



HAL
open science

Aluminum plasmonics for optical applications

Dmitry Khlopin

► **To cite this version:**

Dmitry Khlopin. Aluminum plasmonics for optical applications. Micro and nanotechnologies/Microelectronics. Université de Technologie de Troyes, 2017. English. NNT : 2017TROY0034 . tel-02965285

HAL Id: tel-02965285

<https://theses.hal.science/tel-02965285>

Submitted on 13 Oct 2020

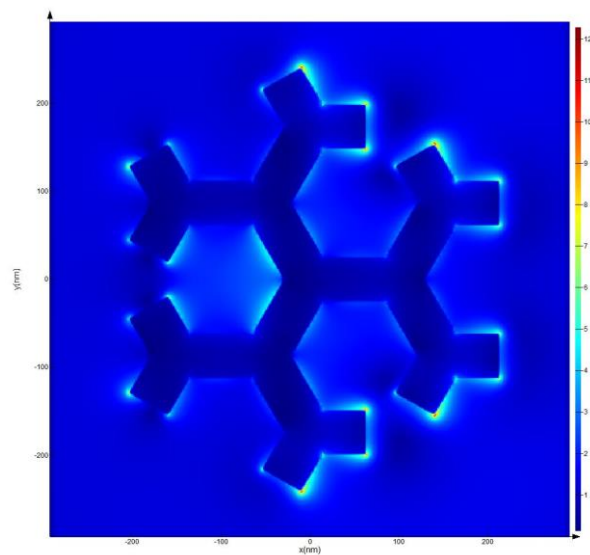
HAL is a multi-disciplinary open access archive for the deposit and dissemination of scientific research documents, whether they are published or not. The documents may come from teaching and research institutions in France or abroad, or from public or private research centers.

L'archive ouverte pluridisciplinaire **HAL**, est destinée au dépôt et à la diffusion de documents scientifiques de niveau recherche, publiés ou non, émanant des établissements d'enseignement et de recherche français ou étrangers, des laboratoires publics ou privés.

Thèse
de doctorat
de l'UTT

Dmitry KHLOPIN

Aluminum Plasmonics for Optical Applications



Spécialité :
Matériaux, Mécanique, Optique et Nanotechnologie

2017TROY0034

Année 2017

THESE

pour l'obtention du grade de

DOCTEUR de l'UNIVERSITE DE TECHNOLOGIE DE TROYES

Spécialité : MATERIAUX, MECANIQUE, OPTIQUE ET NANOTECHNOLOGIE

présentée et soutenue par

Dmitry KHLOPIN

le 15 décembre 2017

Aluminum Plasmonics for Optical Applications

JURY

M. M. KOCIAK	DIRECTEUR DE RECHERCHE CNRS	Président
Mme S. CAMELIO	PROFESSEURE DES UNIVERSITES	Rapporteur
M. W. DICKSON	LECTURER	Examineur
M. D. GÉRARD	MAITRE DE CONFERENCES	Directeur de thèse
M. J. MARTIN	ENSEIGNANT CHERCHEUR UTT	Directeur de thèse
Mme A. PILLONNET	PROFESSEURE DES UNIVERSITES	Rapporteur

Acknowledgements

Looking back to the time I worked on my PhD thesis, I clearly understand that it could not be done without help of many people. Using this opportunity I would like to acknowledge everybody who gave their impact. First off all, I would like to express my deepest gratitude to my supervisors, Dr. Jérôme Martin and Dr. Davy Gérard. Thank you for your guiding during our work, for sharing your knowledge and experience within the different aspects, for the support and encouraging with my ideas. Your optimism, wisdom and patience were the source of my inspiration during this years.

I would like to thank my thesis committee members: Prof. Anne Pillonnet, Prof. Sophie Camelio, Dr. Wayne Dickson, and Dr. Mathieu Kociak for their time, advises and contribution.

My great thanks to our lab engineers Jérémie Beal, Sergei Kostcheev and Regis Deturche for technical support and advises in every moment. As well I would like to thank all my colleagues in LNIO for the precious time and great atmosphere. Especially my colleague Frédéric Laux for the fruitful discussions and help. Also our colleagues from King's College in London take my gratitude for the great collaboration work.

I thank the team of École Doctorale, Isabelle Leclerq, Therese Kazarian and Pascale Denis, for incredible patience and help.

I should mention my friends here in France and back in Russia. Thank you for your belief.

And of course, I would like to thanks my family for support, motivation and love. Your encouragement guided me to my place here.

Contents

Acknowledgements	i
General introduction	1
1 Aluminum plasmonics	3
1.1 General word	3
1.1.1 Dielectric permittivity	3
1.1.2 Band theory and origin of electron gas	5
1.1.3 Drude-Sommerfeld theory	5
1.1.4 Surface plasmons	8
1.1.5 Localized surface plasmons	10
1.2 Aluminum plasmonics	12
1.2.1 Basic optical properties of aluminum	13
1.2.2 Oxidation of aluminum	14
1.2.3 Aluminum nanoplasmonics	15
1.3 Applications of aluminum plasmonics	17
1.3.1 Light generation	17
1.3.2 Raman spectroscopy	20
1.3.3 Color generation	21
1.3.4 Non-linear optics and thermoplasmonics	23
1.4 Conclusion	25
2 Lattice modes in periodic arrays of Al nanoparticles	27
2.1 Linewidth engineering	27
2.1.1 Theory of Rayleigh anomalies	28
2.1.2 FDTD simulations	31
2.2 Experimental methods	33
2.2.1 Fabrication	34
2.2.2 Optical measurements	35
2.3 Conclusion	39
3 Aluminum plasmonics for light emission	41
3.1 Wide band-gap semiconductors	41
3.1.1 Gallium Nitride	41
3.1.2 Boron nitride	43
3.1.3 Zinc oxide	45

3.2	Design of the structure	47
3.2.1	Theory of enhancement	47
3.2.2	Concept of the sample	49
3.3	Experimental results	51
3.3.1	Fabrication of the sample	51
3.3.2	Optical analysis	52
3.3.3	Discussion and outlook	53
3.4	General conclusion	55
4	Fractal plasmonics	59
4.1	Introduction	59
4.1.1	Fractal structure	60
4.1.2	State of the art	62
4.1.3	Surface enhancement	64
4.2	Figure of merit for evaluating fractal structures	65
4.2.1	FDTD simulations	65
4.2.2	Sample production	68
4.2.3	Optical measurements	71
4.2.4	Hot cells	73
4.2.5	Conclusion	75
4.3	Chiral plasmonics with fractal structures	76
4.3.1	Chirality	76
4.3.2	FDTD simulations	80
4.3.3	Optical measurements	83
4.3.4	Discussion and application of chiral aluminum fractals	87
	General conclusion	91
	A Script for fractals	93
	B Résumé	99
B.1	Introduction	99
B.1.1	Plasmonique à base d'aluminium	100
B.2	Modes de réseau	105
B.3	Couplage avec un semiconducteur	108
B.4	Plasmonique dans le visible et l'ultraviolet avec des nanostructures d'aluminium fractales et chirales	112
B.5	Conclusion	116
	Bibliography	119

General introduction

Modern plasmonics is based on the intense and confined electromagnetic fields appearing near metallic nanostructures illuminated at frequencies near their localized surface plasmon resonances. The field of plasmonics is rapidly growing since the end of previous century. Nowadays it proposes multiple applications for enhancing efficiency of photonic devices.

Among the different metals, aluminum sustains a broad range of surface plasmon resonances from deep UV to near IR due to its properties. Sharp plasmonic resonances can be achieved with aluminum nanostructures in near UV where popular noble metals cannot provide a comparable quality of resonance. Aluminum also has a native oxide protection layer and it is a very economically efficient material due to its low cost and recycling quality. However, aluminum has high losses in the visible part of spectrum and its interband transitions are placed around 800 nm. This is why aluminum is usually less attractive for visible plasmonics in comparison with noble metals.

This thesis is a contribution to the wide field of aluminum plasmonics. The main goal consists in adapting the plasmonics techniques commonly used with noble metals in order to push them toward the blue and UV region using aluminum. This requires fabrication processes and a specific procedure for the fabrication of complex aluminum nanostructures, with applications in fields like light generation and extraction. A bibliographic summary of the state-of-the-art of the studied field is presented in Chapter 1. Theoretical aspects of general and aluminum plasmonics are described and several applications of aluminum structures for optics are discussed.

In the second Chapter, a strategy to increase the resonance quality based on diffractive coupling in periodic arrays is presented. Plasmonic resonances coupled with diffractive Rayleigh anomalies lead to hybrid modes with sharp resonances. This approach is studied theoretically and with FDTD simulations. Further samples were fabricated and investigations based on achieved data were made.

Chapter 3 proposes an application of the studied arrays of nanoparticles. Aluminum nanostructures are coupled with a wide band gap semiconductor to enhance its emission. Periodic arrays of Al nanoparticles were fabricated onto a ZnO epitaxial layer. Theoretical concept of the sample contains several aspects of enhancement such as: Purcell effect, antenna effect and waveguiding. Their influence and the results are explained here.

Next Chapter derives from the problematics of Chapter 3: "How to increase the enhancement effect and get more efficient surface coverage without structuring semiconductor substrate?". For this purpose we used a fractal geometry inspired by radiowave technology. The FDTD simulations were performed to design an effective geometry optimized

for certain wavelength. After the structures were fabricated with an adapted electron beam lithography process.

Finally, we propose a concept of chiral fractals. Using the complex geometry of fractals, it is possible to push optical chirality of plasmonic structures towards the UV part of the spectrum. This possibility was proved with the FDTD simulations in the second part of Chapter 3. Samples of chiral fractals were fabricated and the existence of circular dichroism in fractal structures was experimentally demonstrated.

Chapter 1

Aluminum plasmonics

*The light lives in all places, in all things.
You can block it, even try to trap it, but the
light will find its way.*

The Speaker, *Destiny 2*

1.1 General word

A plasmon is a quanta of oscillations of the free electron gas (i.e. a plasma) in a metal. Its existence can explain several optical properties of metals. Their first applications appeared long before the name plasmon was even coined. Since ancient times, stained glasses were made by the inclusion of small metallic particles in glass. A well-known example is the Lycurgus cup [Freestone et al., 2007], a Roman cup dated from the IVth century and made from glass with metallic inclusions. Then, stained glasses were massively used in churches and palaces, like in the Cathedral of Saint-Pierre-et-Saint-Paul of Troyes. The first theory of the "plasma oscillation" was proposed by [D. Pines and D. Bohm, 1952], with an experimental observation using electron energy loss spectroscopy by Powell and Swan in 1959 [Powell and Swan, 1959], using aluminum thin films. From that point on plasmonics started to grow, however it is the rise of nanotechnology that will incredibly boost the field. It can be argue that the starting date of "modern" plasmonics is 1998 with the publication of T.W. [Ebbesen et al., 1998] in Nature about the extraordinary transmission of light through hole arrays. The main change brought by nanotechnology is the ability to manufacture nanostructures with controlled size and shape, such as the nanoholes in Ebbesen work. Nowadays plasmonics is featured in more than 1500 publications per year and thousands of applications. Currently it is one of the major driving forces of the fascinating field of nanooptics, which explores how electromagnetic fields can be confined and manipulated at the nanoscale.

1.1.1 Dielectric permittivity

Optical properties of materials, including metals, are characterized by a variable called dielectric permittivity – $\epsilon(\omega)$. In this chapter we discuss the origin of this dependence.

Maxwell's equations are powerful tools of classic electrodynamics, which can be used to describe the electron gas appearing due of the huge electron density inside metals and negligible difference in energy levels in comparison with kT .

$$\begin{aligned}
\nabla \vec{D} &= \rho_{free} \\
\nabla \vec{B} &= 0 \\
\nabla \times \vec{E} &= -\frac{\partial \vec{B}}{\partial t} \\
\nabla \times \vec{H} &= \vec{j} + \frac{\partial \vec{D}}{\partial t}
\end{aligned} \tag{1.1}$$

where \vec{E} is the electric field, \vec{D} - the electric induction, \vec{B} - the magnetic induction and \vec{H} - the magnetic field. \vec{j} and ρ are current and charge densities respectively. Those values are connected through electric and magnetic polarization via the constitutive equations, presented for Fourier space for simplification:

$$\begin{aligned}
\vec{D}(k, \omega) &= \epsilon_0 \epsilon(k, \omega) \vec{E}(k, \omega) + \vec{P}(k, \omega) \\
\vec{B}(k, \omega) &= \frac{1}{\mu_0 \mu(k, \omega)} \vec{H}(k, \omega) + \vec{M}(k, \omega)
\end{aligned} \tag{1.2}$$

and

$$\begin{aligned}
\rho &= -\nabla \vec{P} \\
\vec{j} &= \frac{\partial \vec{P}}{\partial t}
\end{aligned} \tag{1.3}$$

where μ is the magnetic permeability and ϵ is a dielectric permittivity. Both are generally tensors. In the case of a linear isotropic material with negligible space dispersion those equations take the following form:

$$\begin{aligned}
\vec{D}(k, \omega) &= \epsilon_0 \epsilon(\omega) \vec{E}(k, \omega) \\
\vec{B}(k, \omega) &= \mu_0 \mu(\omega) \vec{H}(k, \omega)
\end{aligned} \tag{1.4}$$

Dielectric permittivity is a complex number $\epsilon = Re(\epsilon) + i \cdot Im(\epsilon)$ and is directly connected to the complex refractive index:

$$\tilde{n} = \sqrt{\epsilon} = n + i\chi \tag{1.5}$$

Parameter χ here is the extinction coefficient connected with absorption in a material. From Eq. 1.5 can be derived:

$$Im(\epsilon) = 2n\chi \tag{1.6}$$

This means that the imaginary part of ϵ describes the absorption of materials.

1.1.2 Band theory and origin of electron gas

The main reason behind the unique properties of metals lies in their electronic configuration. In a single metal atom, electrons have discrete energy levels known as atomic orbitals. Usually, metals at standard conditions have less than 4 electrons on the outer orbit. For example, aluminum electronic configuration is $1s^2 2s^2 2p^6 3s^2 3p^1$, which means 3 electrons in the outer orbit.

When two atoms are combined in a molecule, the atomic energy levels split into pairs of molecular energy levels. Accordingly, in a crystal structure the atomic levels split into a huge number of energy levels, creating continuous bands of energy states.

From quantum statistics, we have a Fermi-Dirac distribution that describes energy distribution of identical particles with half-integer spin, like electrons, in a system at thermodynamic equilibrium.

$$\tilde{n}_i = \frac{1}{e^{(\epsilon_i - \mu)/k_B T} + 1} \quad (1.7)$$

where k is Boltzmann's constant, T is the absolute temperature, ϵ_i is the energy of the single-particle state i , and μ is the total chemical potential. The probability that the many-particle system is in the state R , is given by the normalized canonical distribution [Reif, 1998]

$$P_R = \frac{e^{-\beta E_R}}{\sum_{R'} e^{-\beta E_{R'}}} q^i \quad (1.8)$$

where $\beta = 1/k_B T$. From this the Fermi level E_F can be derived as energy where probability of finding a particle becomes 50 percent:

$$E_F = \frac{\hbar^2}{2m} \left(\frac{3\pi^2 N_e}{V} \right)^{2/3} \quad (1.9)$$

In metals with a given band structure, the Fermi level E_F lies inside at least one energy band. In semiconductors and dielectrics E_F is located in the band gap. This leads to the fact that inside of the band some energy levels are free, and it allows electrons to move along the material. For example in figure 1.1 presenting band structure of aluminum.

In summary, in metals electrons can freely move from one atom to another. Those electrons form the free electron gas with concentration n_0 inside of the metal.

Unique interaction between metal and light goes from oscillations of the electron gas.

1.1.3 Drude-Sommerfeld theory

P. Drude, 1900 created a very efficient plasma theory to explain the optical properties of metals based on the interaction of light with electron gas. Later on, this theory was supplemented by Lorentz and Sommerfeld, so the now in the literature Drude-Lorentz-Sommerfeld theory can be mentioned [Bartlett et al., 2004]. In the origin this model uses a definition of free electrons that combines non-uniformity of crystal lattice potential and electron-electron interaction, i.e. band theory in further study, into the effective mass of the electron m^* . In this case Drude theory does not work well at the wavelengths of interband transitions in

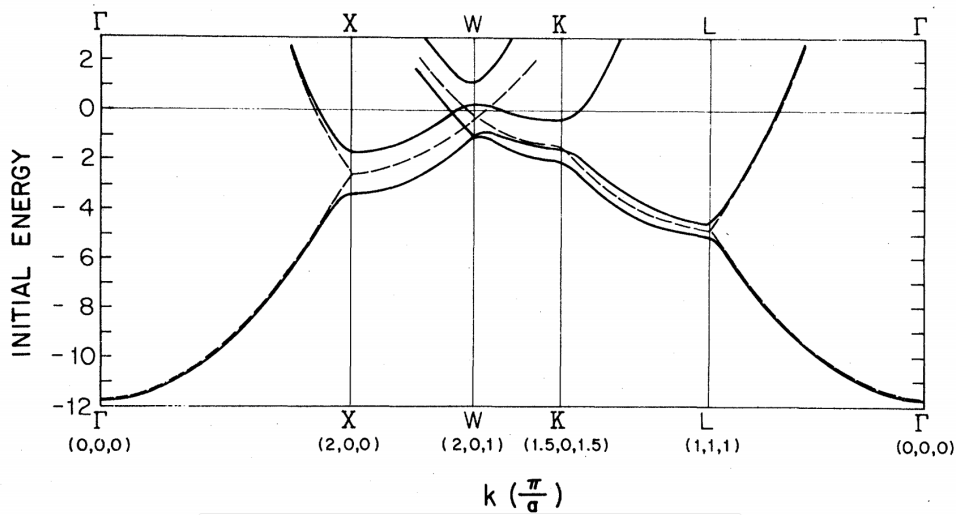


FIGURE 1.1: Aluminum band structure. Extracted from Levinson, Greuter, and Plummer, 1983.

metals, because within this region band influence cannot be neglected. Within the Drude model, the equation governing the movement of an electron in the presence of an external electric field E takes the form:

$$m^* \ddot{x} + m^* \gamma \dot{x} = -eE \quad (1.10)$$

where $\gamma = 1/\tau$ is the frequency of collisions of electrons and τ is a free path time, x is the position, \ddot{x} is the acceleration, \dot{x} is the speed, e is the electron charge and E is the electric field.

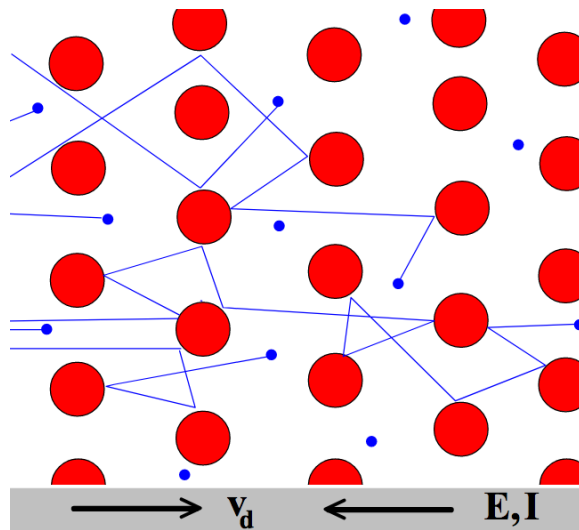


FIGURE 1.2: Drude model electrons (shown here in blue) constantly bounce between heavier, stationary crystal ions (shown in red). Extracted from Wikimedia.

In case of a monochromatic, time-harmonic field $E(t) = E_0 e^{-i\omega t}$ solution becomes:

$$X(t) = \frac{eE}{m^*(\omega^2 + i\omega\gamma)} \quad (1.11)$$

Shift of the electron gas leads to the polarization:

$$P = -n_0 e X = -\frac{n_0 e^2 E}{m^*(\omega^2 + i\omega\gamma)} \quad (1.12)$$

From this equation in combination $\epsilon = 1 + \chi$, which comes from eq. 1.5 we can derive the dielectric permittivity:

$$\epsilon(\omega) = 1 - \frac{\omega_p^2}{\omega^2 + i\omega\gamma} \quad (1.13)$$

where $\omega_p = \sqrt{n_0 e^2 / m^*}$ - the plasma frequency of free electron gas. At high frequencies, where $\omega\tau \gg 1$ imaginary part of ϵ can be neglected and $\epsilon \approx 1 - \omega_p^2 / \omega^2$. But in the area of interband transitions real and imaginary parts become roughly of the same order. As a compensation, in this case, a Drude-Lorentz model can be used as follows:

$$\epsilon(\omega) = \epsilon_{Drude}(\omega) + \epsilon_{Interband}(\omega) = \left(1 - \frac{\omega_p^2}{\omega^2 + i\omega\gamma}\right) + \left(\frac{G_0 \omega_0^2}{\omega_0^2 - \omega^2 - i\Gamma\omega}\right) \quad (1.14)$$

where ω_0 is the central frequency, G_0 is a gain, and Γ the damping factor from Lorentzian model of the interband transitions.

This approximation also works well for macro particles, in classic electrodynamics. But if we decrease the size of the particle to the nanometric scale, free mean path of electrons become comparable with the size of the particle. This also will increase imaginary part of the dielectric permittivity as soon as it is dependent from γ . With a decrease of any dimension below ≈ 10 nm, quantum effects and separated energy levels start to affect the properties and the model should be much improved. As example of values following 1.1 is provided:

	Au	Ag	Al
$n_0(m^{-3})$	$5.9 * 10^{28}$	$5.76 * 10^{23}$	$2.1 * 10^{29}$
$\omega_p(eV)$	9.1	9.1	15
$\tau(fs)$	27.3	36.8	11.8

TABLE 1.1: Drude parameters for gold, silver and aluminum. Extracted from Klimov, 2014, Ordal et al., 1983 and Gall, 2016.

Now assume situation with infinite metal volume. Dispersion law for transversal waves ($div \vec{E} = 0$) will take form:

$$\omega^2 \epsilon(\omega) = c^2 k^2 \quad (1.15)$$

And in case of Drude dispersion:

$$\epsilon(\omega) = 1 - \frac{\omega_p^2}{\omega^2} \quad (1.16)$$

From those equations, the existence conditions of a wave, the so-called volume plasmon, can be derived:

$$\omega = \sqrt{\omega_p^2 + c^2 k^2} \quad (1.17)$$

The dispersion curve of those conditions represented in figure 1.3.

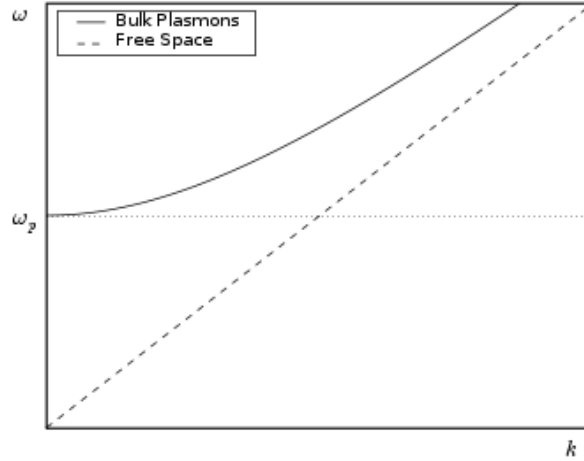


FIGURE 1.3: Dispersion curve for volume plasmon. Extracted from White, 2007.

1.1.4 Surface plasmons

Previously we discussed volume plasmons. This type of plasmon are not localized waves, because their dispersion curve is located higher than the light line, see Fig. 1.3. Much more interesting for nanotechnology, surface plasmons can appear at the interface between a metal and a dielectric. The first mention of such oscillations appeared in works of [Zenneck, 1907] and [Sommerfeld, 1909], connected with problems in telegraph. To describe the surface plasmon phenomena, we consider a simple metal-dielectric interface, as shown in figure 1.4

In this configuration, solutions of the Maxwell's equations can be written for the metal:

$$\begin{aligned} \vec{E}_m &= \vec{E}_0 \left\{ 1, 0, \frac{k_{sp}}{k_{zm}} \right\} \exp\{i(k_{sp}x - k_{zm}z - \omega t)\} \\ \vec{H}_m &= -\vec{E}_0 \frac{\epsilon_m}{k_{zm}} \left(\frac{\omega}{c} \right) \{0, 1, 0\} \exp\{i(k_{sp}x - k_{zm}z - \omega t)\} \end{aligned} \quad (1.18)$$

and for the dielectric side:

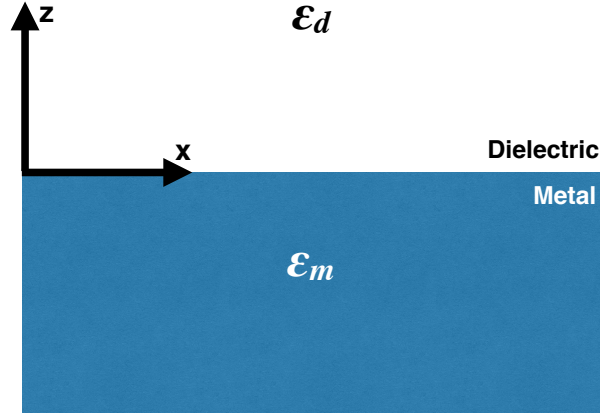


FIGURE 1.4: Metal-dielectric interface geometry.

$$\begin{aligned}\vec{E}_d &= \vec{E}_0 \left\{ 1, 0, -\frac{k_{sp}}{k_{zd}} \right\} \exp\{i(k_{sp}x + k_{zm}z - \omega t)\} \\ \vec{H}_d &= \vec{E}_0 \frac{\epsilon_d}{k_{zd}} \left(\frac{\omega}{c}\right) \{0, 1, 0\} \exp\{i(k_{sp}x + k_{zm}z - \omega t)\}\end{aligned}\quad (1.19)$$

where

$$\begin{aligned}k_{zm} &= \sqrt{\epsilon_m(\omega) \left(\frac{\omega}{c}\right)^2 - k_{sp}^2} \\ k_{zd} &= \sqrt{\epsilon_d(\omega) \left(\frac{\omega}{c}\right)^2 - k_{sp}^2}\end{aligned}\quad (1.20)$$

are the wavevectors orthogonal to the interface in metal and dielectric side correspondingly, and k_{sp}^2 - surface plasmon wavevector. From the continuity of tangential components of electric and magnetic fields, we can write the dispersion equation:

$$\frac{\epsilon_m}{k_{zm}} + \frac{\epsilon_d}{k_{zd}} = 0 \quad (1.21)$$

This equation shows the possibility to have a wave without a source, i.e. it is an electromagnetic mode. In combination with the previous equation, we get:

$$k_{sp} = \frac{\omega}{c} \sqrt{\frac{\epsilon_m(\omega)\epsilon_d(\omega)}{\epsilon_m(\omega) + \epsilon_d(\omega)}} \quad (1.22)$$

And through this it possible to write the components of the wavevector that are orthogonal to the interface:

$$k_{z,j}^2 = \left(\frac{\omega}{c}\right)^2 \frac{\epsilon_j^2}{\epsilon_m + \epsilon_d}, \quad \text{with } j = m, d \quad (1.23)$$

Surface plasmons are localized waves along the interface. It means that along the interface k_{sp} wavevector should be real, and $k_{z,j}$ should be imaginary. This implies:

$$\begin{aligned}\epsilon_m(\omega)\epsilon_d(\omega) &< 0 \\ \epsilon_m(\omega) + \epsilon_d(\omega) &< 0\end{aligned}\tag{1.24}$$

Metals like gold, silver or aluminum have a large negative real part of permittivity and relatively small imaginary part. In this case surface plasmons can exist on the interface of those materials.

$$\begin{aligned}\omega &> \omega_p \\ \omega &< \frac{\omega_p}{\sqrt{\epsilon_d + 1}}\end{aligned}\tag{1.25}$$

Figure 1.5 shows the dispersion curve from equation 1.19 if we take Drude's dispersion for the metal $\epsilon_m(\omega) = 1 - \omega_p^2/\omega^2$. Two branches corresponding to volume and to surface plasmons as predicted by equation 1.22. Note that due to their nature, surface plasmons propagating along a metal-dielectric interface are sometimes called "propagating surface plasmon" or "delocalized plasmons". Another kind of plasmonic excitation, known as localized surface plasmons, also exists and is described in the next section.

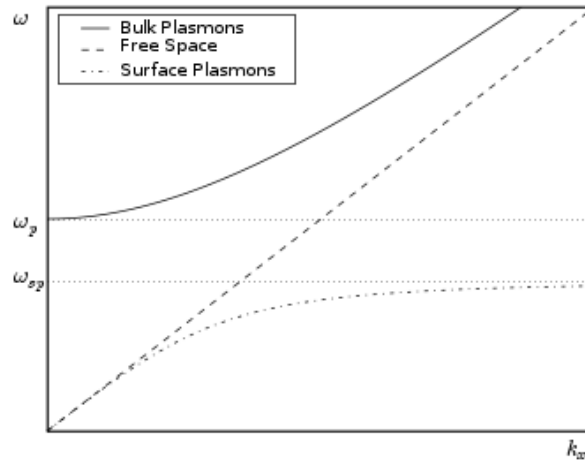


FIGURE 1.5: Dispersion curve for volume and surface plasmon. Extracted from White, 2007.

1.1.5 Localized surface plasmons

Oscillation of electrons in metallic nanoparticles whose size is smaller than the wavelength of the exciting light are called localized surface plasmons. The main difference with volume and surface plasmons lies in the fact that localized surface plasmons can exist only at

fixed resonance frequencies, depending on the particle's shape, size and material. Those frequencies are called plasmonic resonances.

There are two main approaches for the theoretical calculation of plasmonic resonances and the associated distribution of electromagnetic fields:

1. The first method is to solve Maxwell's equations, or their integral form, for different frequencies and to find the frequency-dependence of parameters of interest, such as the scattering cross-section. The scattering cross-section is maximum at the plasmonic resonance and plotting the electromagnetic fields at this frequency yields the spatial distribution of the plasmon mode. The main drawback of this method is that it cannot be easily applied to the different materials, even with the same particle form. Moreover, the scattering cross-section is affected by material losses and other things, so it could decrease precision of calculations.
2. The second method, called the effective medium theory [Elser et al., 2006] is based on a important value, already introduced - dielectric permittivity, which depends on frequency. This method is more universal and allows a deeper understanding of the localized plasmons. In this method, a lot of attention is payed to the form of the particle and its influence on the optical properties.

Effective medium theory is well explained in the book of [V. Klimov, 2014]. Using non-standard methods, solutions of Maxwell's equations can be written in the form:

$$E = E_0 = \sum_n e_n \frac{(\epsilon(\omega) - 1) \int_{V+} e_n E_0 dV}{(\epsilon_n - \epsilon(\omega)) \int_{V+} e_n^2 dV} \quad (1.26)$$

where E_0 is the electric field without the particle, n is the mode index, ϵ_n and e_n are eigenvalue and eigenfunction, respectively, $V+$ is the volume inside the particle. There is a resonance factor $\epsilon_n - \epsilon(\omega)$. ω_n - resonance frequencies, leads to $\epsilon_n - \epsilon(\omega) = 0$. Width of the resonance is dependent on imaginary parts of ϵ_n of $\epsilon(\omega)$, but usually $Im(\epsilon_n) \ll Im(\epsilon(\omega))$.

An analytic solution can be derived for particles exhibiting a high degree of symmetry, such as spheres [Mie, 1908] or spheroids [Yamashita, Wakoh, and Asano, 1975]. Analytic solutions can be found for other forms but they become unnecessarily complicated and numerical solutions are generally used instead.

For particles with sizes $d \ll \lambda$ the quasi-static approximation can be used. For example, let us consider the simple case of a homogeneous sphere of radius a , made from a Drude metal, inside a dielectric medium with permittivity ϵ_m . A static electric field $E = E_0 \hat{z}$ is applied to the system. A sketch of the system is shown in figure 1.6.

Potentials inside Φ_{in} and outside Φ_{out} can be written as follows, derivation can be found in [Maier, 2007] or [Jackson and Fox, 1999]:

$$\begin{aligned} \Phi_{in} &= -\frac{3\epsilon_m}{\epsilon + 2\epsilon_m} E_0 r \cos\theta \\ \Phi_{out} &= -E_0 r \cos\theta + \frac{\epsilon - \epsilon_m}{\epsilon + 2\epsilon_m} E_0 a^3 \frac{\cos\theta}{r^2} \end{aligned} \quad (1.27)$$

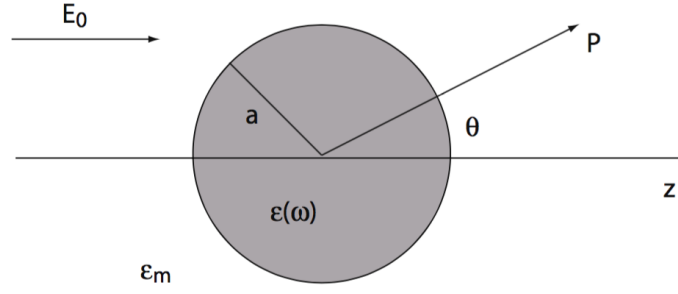


FIGURE 1.6: Sketch of a homogeneous sphere placed into an electrostatic field. Extracted from Maier, 2007.

To simplify those equations an induced dipole moment p is introduced:

$$p = 4\pi\epsilon_0\epsilon_m a^3 \frac{\epsilon - \epsilon_m}{\epsilon + 2\epsilon_m} E_0 \quad (1.28)$$

And from there a polarizability α , a key feature of those calculations, can be defined as:

$$\alpha = 4\pi a^3 \frac{\epsilon - \epsilon_m}{\epsilon + 2\epsilon_m} \quad (1.29)$$

From polarizability α we can see that resonance takes place at $\epsilon(\omega) = -2\epsilon_m$. Also from further calculations [Lord, Zhan, and Pawliszyn, 2012] a cross section of scattering C_{sca} and absorption C_{abs} under plane wave illumination can be found as follows:

$$\begin{aligned} C_{sca} &= \frac{k^4}{6\pi} |\alpha|^2 \\ C_{abs} &= k \text{Im}(\alpha) \end{aligned} \quad (1.30)$$

where $k = 2\pi/\lambda$.

1.2 Aluminum plasmonics

During the last decades, plasmonics has mainly involved the study of gold and silver nanostructures. This is primarily due to their suitable properties in the visible part of the spectrum, i.e. electric permeability has a negative real value and imaginary is relatively small. But with development of the plasmonics field, the need for new materials became a crucial question due to the high price of noble metals and the limited covered part of spectra. For a long time aluminum was underestimated for plasmonics purposes, both due to its relatively high losses in the visible region and to its rapid oxidation when exposed to air. However, as fabrication technologies and know-how increase, aluminum now appears as a great alternative material for plasmonics. Furthermore, aluminum provides an economic advantage because it is cheap and widely available, and compatible with complementary metal–oxide–semiconductor (CMOS) technology.

1.2.1 Basic optical properties of aluminum

As discussed previously, aluminum has a high concentration of free electrons $n = 6 \cdot 10^{23} \text{ m}^{-3}$. The plasma frequency ω_p directly depends on this concentration. For aluminum, the plasma frequency is $\omega_p = 15 \text{ eV}$. That is $\approx 60\%$ higher than the same values for gold and silver (see table 1.1). So by the formula 1.22 we can assume that aluminum should provide a wider spectral range for surface plasmons than gold or silver. But since pioneering studies back in the middle of the 20th century [Ehrenreich, Philipp, and Segall, 1963], aluminum has the reputation of being a lossy and unstable material, not suitable for plasmonics. As a consequence, it has not been studied widely as a plasmonic material until recently.

The main problems associated with aluminum can be summarized in a two very important issues:

1. Aluminum exhibits an interband transition around a wavelength of 800 nm, right in the middle of a region of interest for the evolving field of plasmonics. Interband transitions creates high optical losses and also the classical Drude model approximation is not working properly in this region.
2. Aluminum has a high imaginary part of ϵ for wavelengths higher than roughly 500 nm and this means high losses in this region. Real and imaginary parts of the dielectric permittivity can be observed in figure 1.7.

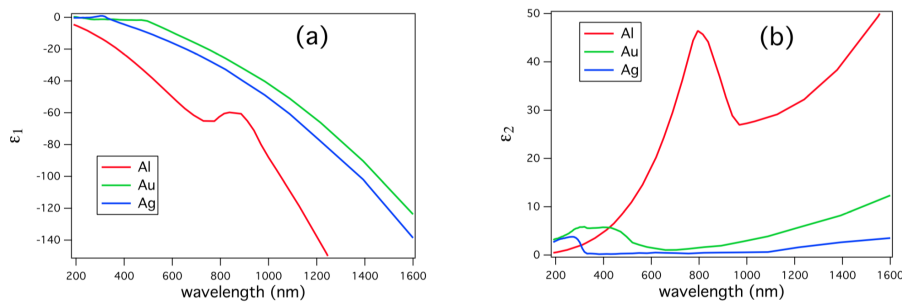


FIGURE 1.7: Real and imaginary parts of the electric permittivity of aluminum. Extracted from Gérard and Gray, 2015. Data was taken from work of Palik, 1997 and Rakić, 1995.

However, those disadvantages can be turned into advantages. Silver and gold have a lower frequency ω_p and both of them have interband transitions in blue and near-ultraviolet part of the electromagnetic spectrum. In this region, aluminum overcomes all noble metals in optical properties. Group of [West et al., 2010] performed simulations with finite difference time domain method (FDTD) of the quality factor for plasmonic resonances of spherical particles made out of different metals. Results of their work shown in figure 1.8. As can be seen, aluminum shows much higher values in the UV region than the others.

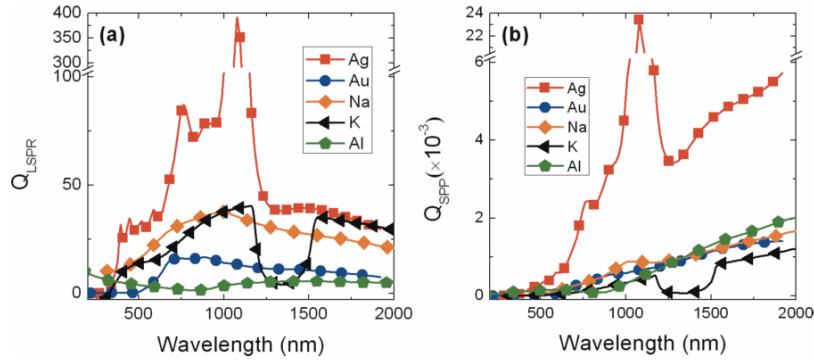


FIGURE 1.8: Quality factors for localized surface plasmon resonances (Q_{LSPR}) is shown in panel (a), and surface plasmon polaritons quality factor (Q_{SPP}) is shown in panel (b). Extracted from West et al., 2010.

1.2.2 Oxidation of aluminum

Even outside the field of optics, aluminum is well known for its lightweight and resistance to erosion. The second property comes from the fact that top layer of aluminum oxidizes incredibly fast, forming an alumina (Al_2O_3) layer. Alumina is a very robust material with a high melting point. The solid alumina layer also affects any fabrication process – this will be discussed later. Fabricated aluminum nanostructures oxidize right after fabrication by just being in air. However, after forming a 3 nm native layer of alumina, the oxidation process stabilizes and particles can keep the same oxide shell thickness for a long time: from a week to months, depending on the environmental conditions (humidity and temperature)[Langhammer et al., 2008a].

Oxidation is of course detrimental for plasmonic properties. It creates a gap between the surface of the particle and the metal. For some applications this could be critical, for example for Surface Enhanced Raman Spectroscopy (SERS). In figure 1.9 presented simulated dependence of extinction spectra versus the thickness of alumina shell for constant size of the particle [Zhang et al., 2017]. As found in this interesting work, there is an obvious decrease of half-width of the resonance peak, i.e. quality factor (Fig 1.9a), but also both a red and a blue shift are observed (1.9b). The red shift comes from a high refractive index of alumina surrounding the metal core, while the blue shift appears due to the decreasing the size of the core, eventually overcoming the red shift.

The main topic of the work described by F. Zhang is about increasing quality of plasmonic resonances through Rapid Thermal Annealing (RTA). One of the biggest issues with aluminum particles fabrication is their poly-crystalline grain structure. Several methods have been reported [Martin and Plain, 2015] to improve fabrication using either low or high evaporation speeds of the metal, but mono-crystalline aluminum is unachievable with simple methods such as thermal evaporation. Using a RTA post-treatment on aluminum nanoparticles, F. Zhang achieved a bigger grain size with moderate oxide layer growth. This leads to increased quality factors of the localized surface plasmon resonance (LSPR), as

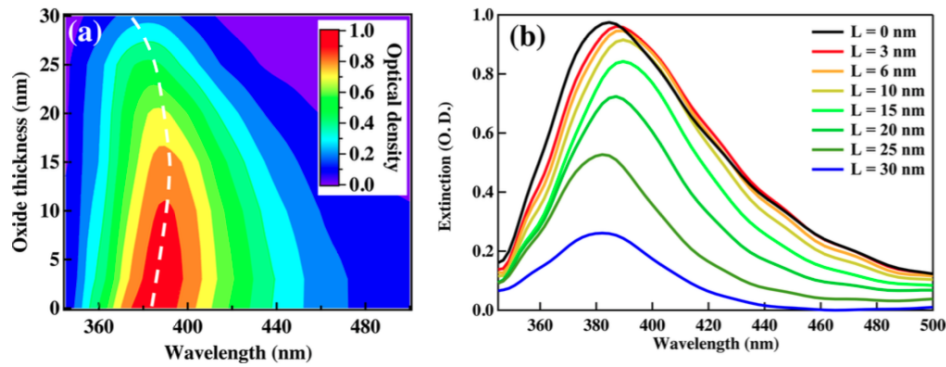


FIGURE 1.9: Extinction spectra calculated with FDTD for a square array of Al nanoparticles with diameter $d = 100$ nm and thickness $h = 40$ nm for different ratios between the volume of Al core and the volume of oxide layer (from oxide thickness $L = 0$ nm, no oxidation, to $L = 30$ nm). (b) Corresponding extinction spectra for several oxide thicknesses. Extracted from Zhang et al., 2017

observed in figure 1.10.

As a conclusion on the oxidation topic, we could say that oxide layer of alumina is not a real issue. Oxidation creates a robust thin native protection layer, which can also be used as a resonance tuning instrument or nanosized melting form.

1.2.3 Aluminum nanoplasmonics

The basic approach to study the optical properties of aluminum nanostructures is to perform extinction spectroscopy on nanostructures with simple geometries. For example, there is a nice study of aluminum nanodisks and nanorods made by M. [Knight et al., 2014]. Figure 1.11 reprinted from their article presents the evolution of the plasmonic resonance with increasing sizes. As it can be seen, with the shift of the resonance from UV to visible part of the spectrum, the shape of the resonance changes a lot – from a well-defined peak to a broad lowered peak. This also means that the quality factor is decreasing.

Those results are mainly explained by the increase of the electric permittivity of aluminum in the visible region. The grain structure also affects the resonance, due to the electron scattering at grain boundaries. With increasing particle size, this effect is more pronounced.

Although electron beam lithography is probably the best fabrication method for systematic study, it is still difficult to fabricate aluminum particles with diameter lower than 40-50 nm. With those limitations and depositing the nanoparticles onto a quartz substrate, the lower boundary for the achievable resonance wavelength is around 280-300 nm. To go beyond this limit, completely different chemical methods should be used. For instance, in the work by [Maidecchi et al., 2013] particles were fabricated using self-assembly on a silane layer. Another example a quite recent method of chemical fabrication of aluminum

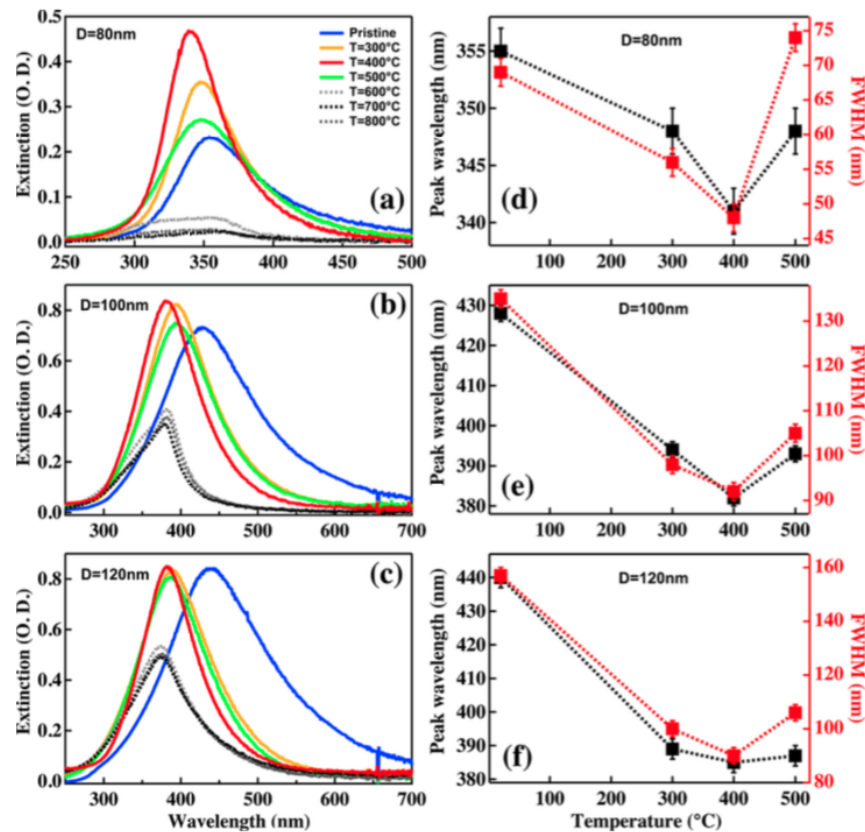


FIGURE 1.10: Column (left), for each box: extinction spectra of Al nanoparticles with fixed diameter after successive RTA treatments with increasing temperature. Column (right): evolution of the peak wavelength and line width with RTA treatment. Extracted from Zhang et al., 2017

nanoparticles with diameter down to 5 nm immersed in ethylene glycol described in patent [Plain et al., 2014]. It is important to mention that at such small sizes quantum effects might become important as discussed previously.

The other possibility to decrease the operating wavelength is to consider higher-order plasmonic modes. For example, quadrupolar plasmon resonances, whose resonance frequencies are higher than that of dipole resonances, can be used. Due to the properties of material, quadrupole and higher modes are more easily excited in aluminum when compared to noble metals, but still the associated absorption and scattering cross-sections are generally quite low. Under some circumstances it is possible to enhance the excitation of a quadrupolar resonance. The easiest way to do that is to use oblique illumination. In the work of [Martin et al., 2014] multipolar resonances was observed in aluminum nanoparticles with electron energy loss spectroscopy.

In most of the aforementioned works, scientists were trying to push the resonance wavelength toward the ultraviolet region. In this area aluminum has little concurrency from the other metals and shows remarkable optical properties. Moreover, and most importantly, UV-plasmonics opens the way to a huge amount of potential applications that we are going to discuss in the following.

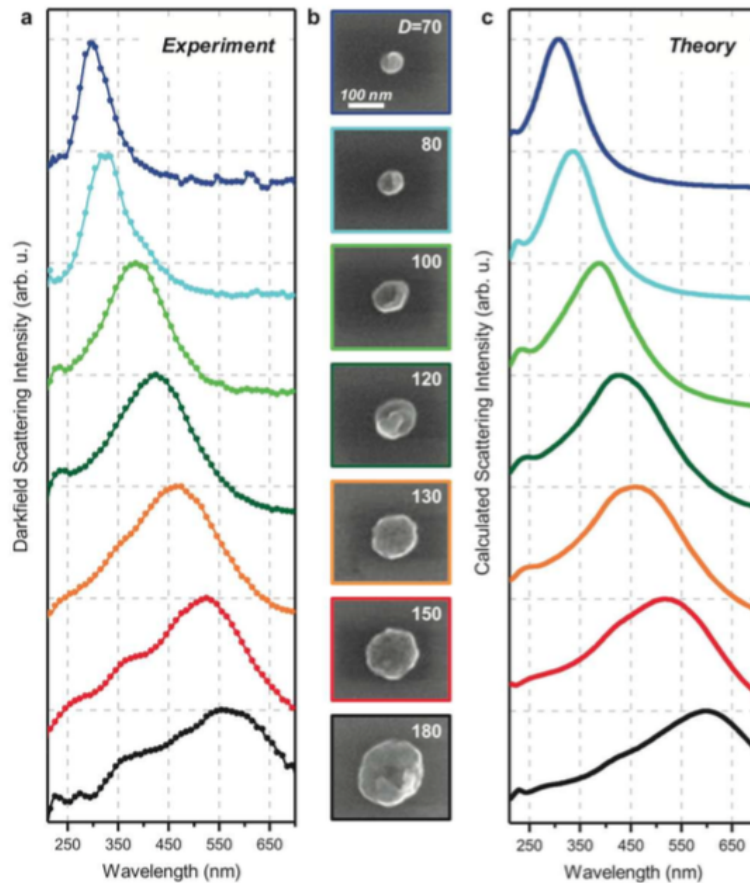


FIGURE 1.11: Tuning of the LSP resonance of Al nanodisks fabricated using e-beam lithography. (a) Experimental scattering spectra of individual nanodisks with varying diameters. ($D = 70, 80, 100, 120, 130, 150, 180$ nm) (b) SEM images of the corresponding nanodisk structures. Scale bar is 100 nm. (c) Finite difference time domain (FDTD) simulations of the scattering spectra, assuming a 3 nm surface oxide and a SiO₂ substrate. Extracted from Knight et al., 2014

1.3 Applications of aluminum plasmonics

The optical properties of aluminum described in the previous section show a great potential for application in different areas. The most promising way is near-UV and blue plasmonics. Sensors, light sources, amplifiers in this region can be enormously useful for application and implementation with biology. Many important biomaterials are somehow sensitive to the UV light, and with aluminum this effect can be greatly increased. Moreover aluminum has low toxicity and, due to the protection of the native oxide layer, resistant to the environment.

1.3.1 Light generation

It is known for a while that surface plasmon can be coupled to luminescent materials, whether fluorophores or semiconductors, in order to enhance their emission. This field is known as "metal-enhanced fluorescence". Fluorescent molecules are more important

for detection and investigation in biological and medical research [Liu et al., 2015], while semiconductor-metal structures and their derivatives (quantum dots, wires and wells) are mainly oriented toward the fabrication of light sources and detectors [Okamoto et al., 2004]. As a combination of both, there is a topic with a fast growing popularity: theranostics [Yu, Park, and Jon, 2012]. The word "Theranostics" is a combination of "Therapy" and "Diagnostics", so as follows from the name this research topic is concentrated on creating heterogeneous particles exhibiting multitask properties.

When a metal is combined with any light-emitting material, there are three main effects that may modify light generation:

1. At the plasmonic resonance, the local electric field intensity is increased in the vicinity of the particle, leading to an increased excitation rate;
2. The so-called Purcell effect makes the particle working as an optical resonator, speeding up relaxation rates in the active material. This yields higher emission rate;
3. Designing the shape of the particle allows one to increase the coupling between the far-field and the near-field, channeling emitted light more efficiently towards the detector or, conversely, concentrating impinging light on the active material. This is the antenna effect.

Aluminum as material for ultraviolet plasmonics shifts all these applications toward the UV region, which is interesting as many molecules can be excited in UV. Usually this emission has a low intensity. As example of such application, the work of J. Eid et al., 2009 can be mentioned. DNA sequencing is a very hot topic, and numerous solutions to perform the sequencing have been proposed. One technique for detection of parts of cut DNA, i.e. nucleotides, is to attach fluorescent markers to them. In [Eid et al., 2009], nano-sized apertures milled in a thin aluminum film (called "zero-mode waveguides") were used to enhance the signal emitted by such markers. A visual description of the method is shown in figure 1.12.

Aluminum can be also used for enhancing of luminescence from rare earth materials, which absorb light in UV and emit in the UV-visible. Let us mention for example the work of Abdellaoui et al., 2015, where the coupling between Eu^{3+} rare earth emitters and aluminum nanostructures has been investigated.

Concerning applications with semiconductors, an attractive direction is the coupling with wide band-gap semiconductors, such as zinc oxide (ZnO) with band gap $E_g = 3.37$ eV, gallium nitride (GaN) with $E_g = 3.2$ eV and boron nitride with $E_g = 5.9$ eV. An interesting fact is that highly n- or p-doped ZnO and AlZnO semiconductors can have a plasmonic behavior at radio frequencies Boltasseva and Atwater, 2011.

The simplest configuration of an Al-semiconductor structure consists of an aluminum film with a layer of semiconductor on its top (or reversed). In this configuration, the semiconductor can be a quantum well [Okamoto et al., 2004] [Gao et al., 2012] or the bulk material [Chou et al., 2015]. In this case the Al layer works as a mirror, amplifying the excitation

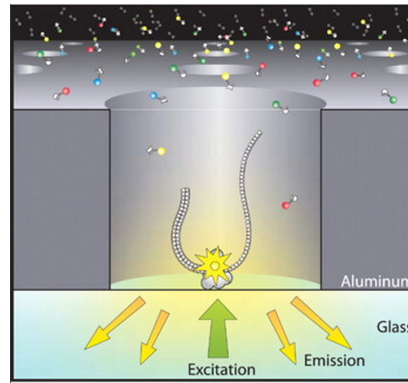


FIGURE 1.12: Experimental geometry. A single molecule of DNA polymerase is immobilized at the bottom of a Zero-Mode aluminum waveguide (ZMW), which is illuminated from below by laser light. The ZMW nanostructure provides excitation confinement in the zeptoliter (10^{-21} liter) regime, enabling detection of individual phospholinked nucleotide substrates against the bulk solution background as they are incorporated into the DNA strand by the polymerase. Extracted from Eid et al., 2009.

light, and also enhances the emission. The reported values of the experimental enhancement factor in those articles is more than 2 times. The next level is structuring the metal surface [Norek, Łuka, and Włodarski, 2016] or changing it to the particle patterns. This will be discussed more precisely in chapter 3.

Using smaller structures to increase light confinement, we can obtain even more localized effects with higher impact. For example, the group of Q. [Zhang et al., 2014] showed a GaN nanolaser and [Chou et al., 2015] demonstrated a ZnO nanolaser. Both projects were based on a configuration where a semiconductor nanowire lies onto either an aluminum [Zhang et al., 2014] or a silver surface [Chou et al., 2015]. This creates a huge local electric field and Purcell effect from the interface metal-semiconductor as shown in figure 1.13. In both works lasing from nanowires was achieved due to plasmonic enhancement.

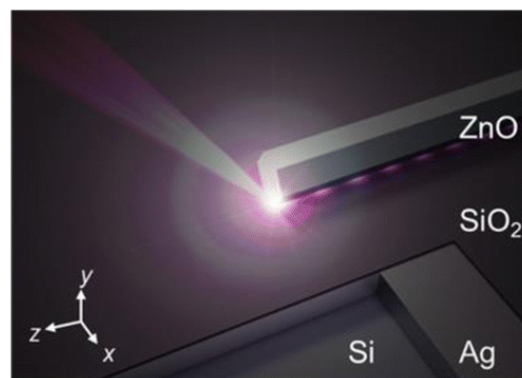


FIGURE 1.13: Robust ultraviolet ZnO nanolaser that can operate at room temperature by using silver to dramatically shrink the mode volume. Extracted from Chou et al., 2015

1.3.2 Raman spectroscopy

Enhanced Raman spectroscopy is a powerful tool for material study through phonon signature. Raman scattering, the core feature of this method, is an inelastic (Stokes) scattering where the energy lost by the photon is transferred to phonons. Raman scattering happens along with elastic (Rayleigh) scattering, but with an extremely low intensity in comparison. In order to enhance the signal, surface plasmons in metals are widely used in different configurations. The two main directions of development in this field are:

1. Surface Enhanced Raman Spectroscopy (SERS) relies on rough metallic films or nanostructures to intensify the Raman signal. Under the incident light excitation, the local electric field around the particles is increased, increasing in turn the Raman scattering (as the Raman scattering cross-section is roughly proportional to the fourth power of the electric field). This technique allows the probing of large surfaces as well as single molecule located in a hot spot between particles [Vlckova et al., 2007]. A sketch is shown in Fig. 1.14a;
2. In Tip Enhanced Raman Spectroscopy (TERS), a metallic (or metal-covered) sharp tip is used. It is needed to create a local increase of the Raman signal at its apex. Combined with a conductive surface, it allows one to perform scanning tunnelling microscopy (STM) at the same time. The sharpness of the tip also provides the possibility to measure the local Raman signal, hence creating a map of the Raman signal with nanoscale resolution [Sheremet et al., 2016]. Schematics can be seen in Fig. 1.14b.

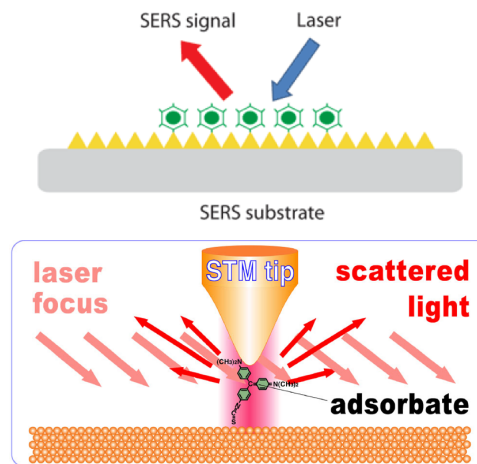


FIGURE 1.14: (top)Conceptual illustration of SERS. Extracted from *Surface Enhanced Raman Spectroscopy*. (bottom)Conceptual illustration of TERS. Extracted from Pettinger, 2010.

The native oxide layer around aluminum nanostructures decreases the effectiveness of SERS but still, in the blue-UV region there is no better metal to use. In [Taguchi et al., 2009], the authors presented results for both methods: SERS using a 10-nm-thick aluminum film on a quartz substrate, and TERS using a silicone tip covered with 25 nm of aluminum.

The study was performed in deep-UV region ($\lambda = 266$ nm). Results are shown in figure 1.15, demonstrating a significant enhancement factor of 4-6 times in both configurations. Especially in comparison with a 20 nm silver film these are very promising results.

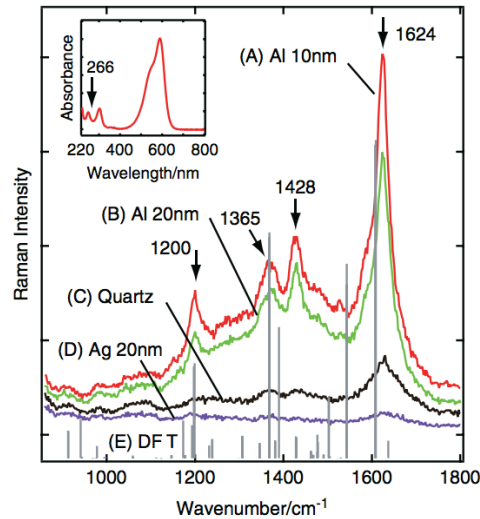


FIGURE 1.15: Resonance Raman spectra of crystal violet aqueous solution placed on (A) 10-nm-thick aluminum film, (B) 20-nm-thick aluminum film, (C) quartz substrate, and (D) 20-nm-thick silver film. Excitation laser wavelength was 266 nm; excitation power, 350 μ W; and exposure time, 300 s. The inset in the left figure shows the UV-vis absorption spectrum of the crystal violet aqueous solution. (E) Calculated vibrational wavenumber of crystal violet by density functional theory (DFT). Extracted from Taguchi et al., 2009

1.3.3 Color generation

The most ancient application of plasmonics is the fabrication of stained glass. Glass masters mixed melted noble metals such as gold and silver with liquid glass to create different transmission/reflection, in other words, colors. Mixing with special (secret at the time) technologies creates a lot of metal nanoparticles and clusters inside the glass. Due to the plasmon resonance sustained by the particles, they scatter light with resonances in the visible region, creating a colored glass. Plasmonic structures of every kind sustain offer possibilities for color generation. With some of the structures it is possible to achieve well-defined colors, suitable for the creation of a color palette, like RGB. As an illustration, a dark field microscopy image of S-shaped aluminum nanostructures, which I made during this PhD, are shown in figure 1.16. An intense and very vivid blue color is observed.

An artificial color generation process using plasmonic structures called "plasmonic colour printing" was first mentioned in the work of [Kumar et al., 2012]. For this purpose, several materials were used including aluminum, which have a very broad allowed zone for plasmonic resonance wavelength. Aluminum metasurfaces has been used for creating a clear Red-Green-Blue palette for pixel application [Olson et al., 2014]. In the cited work, the authors showed pixels formed by periodic arrays of Al nanostructures yielding vivid colors.

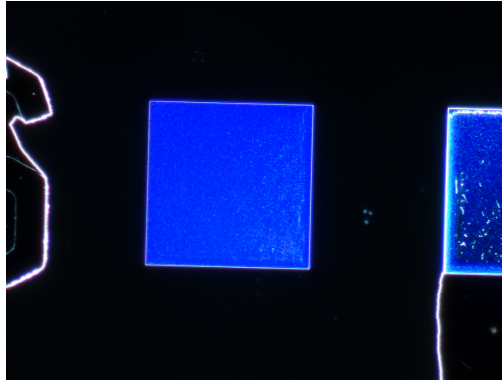


FIGURE 1.16: Photo of a metasurface containing periodic aluminum nanostructures acquired with dark field microscope.

This progress was achieved by exploiting far-field diffractive coupling combined with Fano interference. Results of their work are presented in figure 1.17.

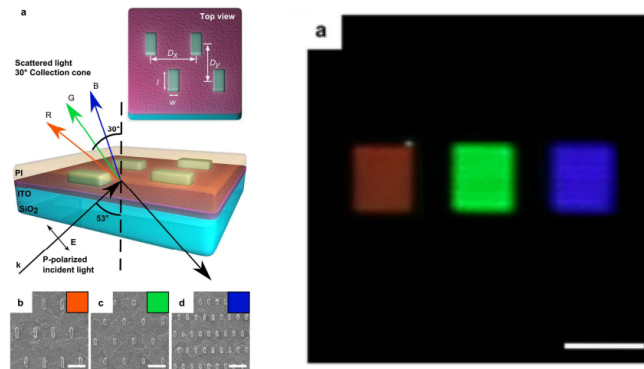


FIGURE 1.17: (a) Schematics of fabricated pixel nanostructures.(b-d)SEM images of fabricated structures.Photograph of three $1.5\text{mm} \times 1.5\text{mm}$ pixels as viewed outside the microscope. Extracted from Olson et al., 2014.

Another approach is to create a plasmonic structure for the exact color needed, for example by analyzing transmission spectra. The simplest way is to choose three wavelengths to represent the RGB palette and then to superimpose transmission at those positions. A more advanced method is to integrate the whole spectra as a superposition of all colors in visible range. Those methods combined with FDTD simulations can be used for designing structures for color printing.

A famous example of such work is an "art" realized by [Tan et al., 2014]. They created a broad plasmonic color palette using "units", or pixels, containing four aluminum nanodisks with different heights, diameters and distances between them. To demonstrate the capability of their plasmonic palette to reproduce natural colors, they created a micro-sized reproduction of Claude Monet's painting "*Impression, soleil levant*". In figure 1.18 a comparison between the micropainting and the original image is shown, as well as a typical unit used of color generation. The agreement between the original painting and its plasmonic rendering is remarkable.

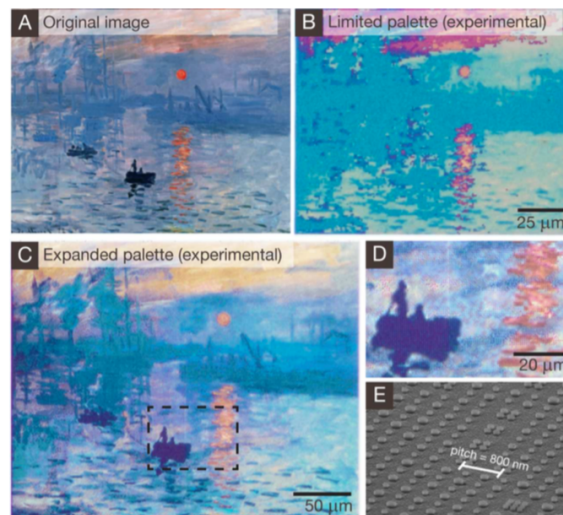


FIGURE 1.18: Structural colors from Al nanoparticles reproduce Monet’s Impression, soleil levant. (A) Original image. (B) Reproduction using the “limited plasmonic palette” (variation of the nanoparticles diameter). (C) Reproduction using the “extended plasmonic palette” (variation of the nanoparticles diameter and spacing). (D) Higher magnification image of the previous panel. (E) SEM image of the plasmonic pixels. Extracted from Tan et al., 2014

1.3.4 Non-linear optics and thermoplasmonics

Non-linear effects in optics are very important for many applications such as ultrafast optical switching and all-optical signal processing. Metal nanostructures can be used to generate such non-linearities, with potential applications in many topics [Boardman and Zayats, 2014]. The second-order non-linear optical susceptibility $\chi^{(2)}$, which is responsible for second order non-linear effects, of aluminum thin films has been measured by D. Krause *et al.* They used a Ti-sapphire laser emitting at a central wavelength of 810 nm with a 50 fs pulse duration [Krause, Teplin, and Rogers, 2004]. The measured value is almost 10 times higher than for gold or silver. However, the measured second harmonic generation (SHG) signal is higher for silver films than for aluminum films. The authors explain this apparent discrepancy by the fact the fundamental pumping wavelength falls into the interband transition region, yielding a deteriorated transmission factor of the pump through the Al film. In any case, aluminum is an interesting material for non-linear plasmonic studies.

Aluminum is also suitable for non-linear photoluminescence (nPL) and heat generation. Plasmonic structures have been systematically probed by nonlinear photoluminescence microscopy, and a comparison between gold and aluminum has been made [Castro-lopez et al., 2008]. The results are however difficult to interpret due a possible role played by the thin conductive oxide at the interface between the metal and the substrate [Schwab et al., 2013]. Another study of non-linear effects in aluminum using nPL microscopy is described in the article of [P.Wiecha et al., 2017], made in collaboration with our group. Both the nPL response and the heat generation rely on the amplitude of the local electric field in the metal. The emitted photoluminescence can be described by the phenomenological relation:

$$I_{nPL}(R_0, \omega) = \nu^2(\omega) \int_V |E(R_0, r, \omega)|^4 dr \quad (1.31)$$

where R_0 and ω are the position and the frequency of the excitation. The prefactor ν is an effective frequency dependent non-linear coefficient and V is the volume of the metallic particle. Finally, E is the total electric field in the metal at the position r

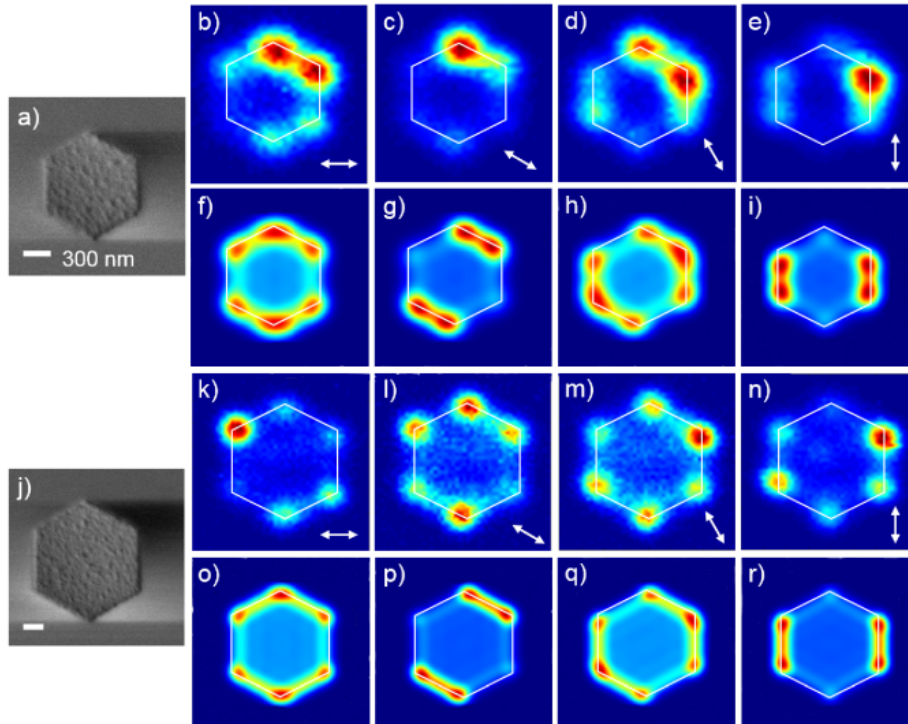


FIGURE 1.19: (a) SEM image of a hexagonal structure with 600 nm long sides. (b-e) nPL maps acquired with incident polarization oriented at (b) 0 degrees, (c) 30 deg, (d) 60 deg and (e) 90 deg. Polarization is indicated by the white arrows. (f-i) Corresponding simulated nPL maps. (j) SEM image of a hexagonal structure with 900 nm long sides. (k-n) nPL maps acquired with polarizations similar to (b-e). (o-r) Corresponding simulated nPL maps. The scale bars are 300 nm. Extracted from Wiecha et al., 2017

In [Wiecha et al., 2017] it was showed that the complex electric field distributions associated to high order plasmonic resonances in planar metal cavities, may be imaged by non-linear photoluminescence microscopy around the aluminum interband transitions. Moreover, a numerical Green dyadic method was successfully used to predict the thermoplasmonic properties. Simulations showed that aluminum can yield a thermoplasmonic response larger than gold in the infrared spectral range due to its interband transitions lying near 800 nm.

Finally, it is possible to study third-order non-linear effects, such as third harmonic generation (THG). Melentiev and collaborators [Melentiev et al., 2013] studied THG in nanostructures (nanoholes and nanoslits) milled in aluminum films for an excitation wavelength

in the infrared ($\lambda = 1500$ nm). From the measurement of the THG intensity, they were able to estimate the value of the third order linear coefficient $\chi^{(3)}$, which was found to be 3 orders of magnitude higher than in gold.

1.4 Conclusion

In this first chapter, we presented a basic introduction to plasmonics and more specifically to the growing field of aluminum plasmonics. We discovered that aluminum has very interesting properties, turning it into a appealing alternative plasmonic material. Aluminum could possibly replace noble metals for some applications, especially in the near-UV and blue region. However, its high losses in the visible part of the spectrum and the interband transitions around 800 nm are still a huge barrier, impeding further development. In the next chapter, we will discuss possibilities of improvement of aluminum nanostructures, in order to obtain higher quality resonances to build effective devices.

Chapter 2

Lattice modes in periodic arrays of Al nanoparticles

Noble metals such as silver and gold provide sharper resonances in the visible and near-infrared spectrum than the so-called “poor” metals, such as aluminum. However, as discussed in the previous chapter aluminum is potentially the best material for UV plasmonics. There are a lot of investigations and successful applications of it for different wavelengths from the deep UV to the blue region of spectrum. It was also shown previously that aluminum can sustain plasmonic resonances from UV to IR thanks to its high plasma frequency $\omega_p = 15$ eV. But in the visible and infrared part of the spectrum it exhibits relatively high losses, that can be derived from the imaginary part of electric permeability $Im(\epsilon)$, as shown in figure 1.7b in the previous chapter. The quality of a resonance is usually quantified with the help of a figure of merit known as the quality factor (or Q -factor) $Q = \omega/\Delta\omega$, where ω is the position of resonance and $\Delta\omega$ is its full width at half maximum. This quality factor is a very important value for different applications.

In this chapter, I will discuss a strategy to improve the quality factor of plasmonic resonances in aluminum particles. This strategy is based on the diffractive coupling between the individual plasmonic resonances of nanoparticles arranged into periodic arrays. First, I will present the theory behind this diffractive coupling, then I will show some numerical simulations and finally I will present the experimental results I obtained.

2.1 Linewidth engineering

There are several possible solutions to improve the quality factor of localised surface plasmon resonances (LSPR). First of all, an obvious way is to use better quality materials: higher purity, higher crystallinity, in other words: less defects. This leads to the increase of the quality factor of the resonance. We saw in the previous chapter that a thermal treatment was able to increase the quality factor of aluminum nanocylinders thanks to the increase of the size of grains in the material [Zhang et al., 2017]. More generally, it has been previously shown that the plasmonic properties were improving the crystallinity of the metal [Laroche, Vial, and Roussey, 2007]. But in any case, the intrinsic optical properties of the material are always a limitation, even in the ideal case of a Drude metal.

The other possibility is to use different geometries. Through symmetry breaking in the particle's shape, it is possible to tune the resonances. In figure 2.1 you can see comparison between different forms of the roughly the same size (about 100 nm). The level of damping of the plasmonic resonance can also be controlled. For instance, the surface plasmon resonances sustained by gold nanorods are significantly sharper than those of nanospheres [Sonnichsen et al., 2002]. It is also possible to couple the resonant modes with other objects, such as particle-particle coupling, or coupling between a particle and a pattern (array of particles). It is the latter solution we chose to explore here.

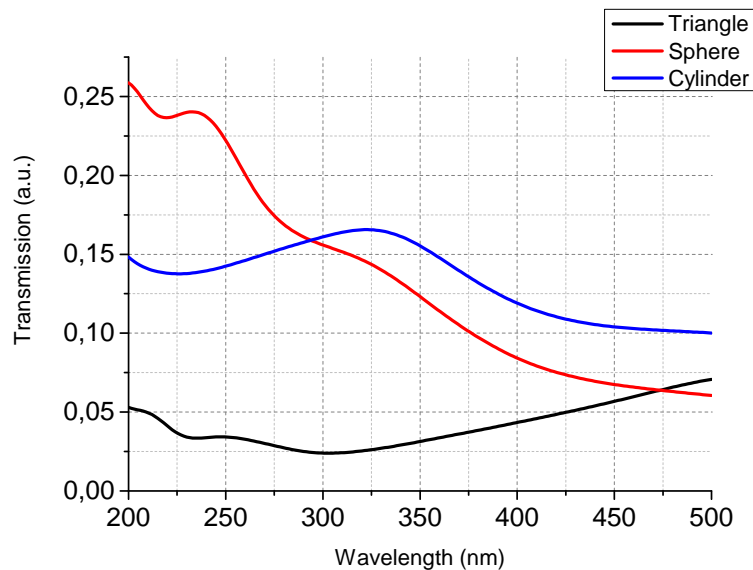


FIGURE 2.1: Transmission spectra obtained with FDTD simulation using Lumerical FDTD Solutions software (homogeneous environment $n = 1$): Aluminum sphere 100 nm radius, Aluminum cylinder height 50 nm and radius 100 nm, Aluminum triangle with sides 100 nm and height 50 nm.

2.1.1 Theory of Rayleigh anomalies

The quality factor of LSPR can be improved in geometries where plasmonic particles are arranged in a periodic array (particle-pattern). Due to diffractive effects, an electromagnetic coupling between scatterers takes place, leading to the emergence of so-called lattice modes [Ross, Mirkin, and Schatz, 2016]. These diffracting lattice modes, also called *surface lattice resonances*, are generally observed near a Rayleigh anomaly of the array. Rayleigh anomalies, or Wood anomalies, were discovered by R.W. Wood, 1935 during the experiments he performed with metallic gratings. One of the original Wood's experimental observations is presented in figure 2.2. It shows the spectrum of a continuous light source given by an optical metallic diffraction grating with different angle of incidence. The dark lines on the spectra correspond to the anomalies.

Later this phenomena was explained by Lord Rayleigh. He proposed that the "anomalies" were in fact light scattered tangentially to the grating surface [Rayleigh, 1907]. The

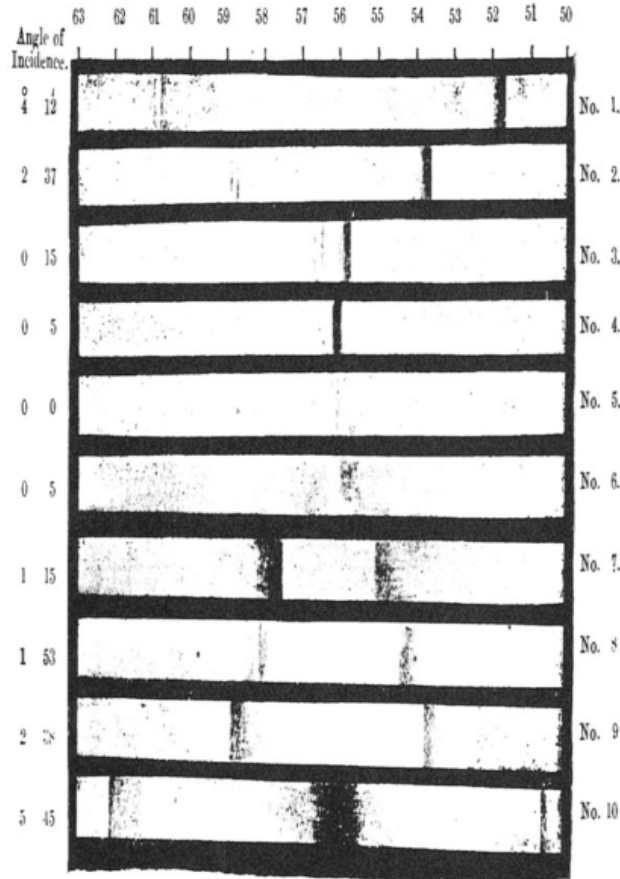


FIGURE 2.2: Spectra of a continuous light source obtained by Wood. The vertical axis is angle of incidence and horizontal is wavelength. The wavelength in nanometers is obtained by multiplying by a factor 10 the numbers shown at the top of the figure. Extracted from Maystre, 2012.

position of the anomalies could hence be predicted using the well-known grating formula [Maystre, 2012]:

$$\sin(\theta_m) = \sin(\theta) + \frac{m\lambda}{D} \quad (2.1)$$

where θ is the angle of incidence, θ_m is the angle of diffraction, D is period of the grating, λ the wavelength and m is the diffraction order $n = \pm 1, \pm 2, \dots$. It can be observed that for some conditions, the angle of diffraction becomes $\theta_m = \pm 90^\circ$, corresponding to a grazing wave:

$$\frac{m\lambda}{D} = -\sin(\theta) \pm 1 \quad (2.2)$$

In this case the lattice modes we introduced before can be understood as a Fano-type process involving a broad resonance (the LSPR) and a discrete photonic state associated with the light scattered in the plane of the array at the Rayleigh anomaly position [Giannini et al., 2011]. In this situation, two hybrid states appear, described by Fano, 1941:

1. Wood anomaly - a diffuse anomaly extends for a wavelength interval from the first one to the higher wavelengths.
2. Rayleigh anomaly - a sharp anomaly with defined wavelengths governed by the grating formula.

The lattice mode is a hybrid state, located close to the Rayleigh anomaly position. It combines properties of both origins: an enhanced scattering cross section, based on the LSP contribution, and a high quality factor. From equation 2.2 we could derive the position wavelength of Rayleigh anomaly:

$$\lambda_{RA} = D \frac{-\sin(\theta) \pm 1}{m} \quad (2.3)$$

This equation is valid in the case of one-dimensional gratings, for example arrays of parallel lines, freely standing in vacuum or air. In the case of nanostructures fabricated in the laboratory, the grating will be placed onto a substrate with a different refractive index. Moreover, two-dimensional gratings will be considered. In the following, we are going to consider the more general configuration of a 2D square grating with period P , located on the interface between two media with refractive indexes n_1 and n_2 . We assume that the incident light makes an angle of incidence θ_i with the normal to the plane of the grating and is located in the (xOz) plane (in other words, the parallel component of the incident wavevector is along the x -axis of the grating). The geometry is depicted in figure 2.3. Below we derive an equation predicting the position of Rayleigh anomalies.

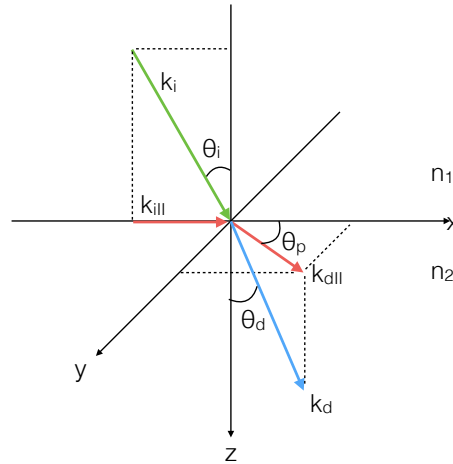


FIGURE 2.3: Demonstration of Rayleigh anomaly.

In Figure 2.3, \vec{k}_i and \vec{k}_d are the incident and transmitted light wavevectors. From here we can derive the grating equation using the conservation of the parallel component of the wavevector \vec{k} :

$$\begin{aligned}\pm k_d \sin \theta_d \cos \theta_p - k_i \sin \theta_i &= m \frac{2\pi}{D} \\ \pm k_d \sin \theta_d \sin \theta_p &= p \frac{2\pi}{D}\end{aligned}\tag{2.4}$$

where m and p are integer indexes describing the diffraction orders. We know that Rayleigh anomaly appears when $\theta_d = \pm\pi/2$. In this case, the equations take the following form:

$$\begin{aligned}\pm k_d \cos \theta_p - k_i \sin \theta_i &= m \frac{2\pi}{D} \\ \pm k_d \cos \theta_p &= p \frac{2\pi}{D}\end{aligned}\tag{2.5}$$

Now we substitute $k = 2\pi n/\lambda$:

$$\begin{aligned}\pm n_2 \frac{2\pi}{\lambda} \cos \theta_p - n_1 \frac{2\pi}{\lambda} \sin \theta_i &= m \frac{2\pi}{D} \\ \pm n_2 \frac{2\pi}{\lambda} \cos \theta_p &= p \frac{2\pi}{D}\end{aligned}\tag{2.6}$$

And from this, the position of the Rayleigh anomalies is given by:

$$\lambda_{RA} = D \frac{\sqrt{n_2^2(m^2 + p^2) - n_1^2 p^2 \sin^2(\theta_i)} \pm m n_1 \sin(\theta_i)}{m^2 + p^2}\tag{2.7}$$

where m and p are integers corresponding to the diffracted order of the anomaly. From this equation can be noticed that m and p , i.e. orthogonal directions, does not play the same roles, as the symmetry of the grating is broken by the incident light. However, at normal incidence, where $\sin(\theta_i) = 0$ formula 2.7 becomes:

$$\lambda_{RA} = D \frac{\sqrt{n_2^2(m^2 + p^2)}}{m^2 + p^2}\tag{2.8}$$

In this case a degeneracy between m and p directions is observed, because $(\pm 1, 0)$ and $(0, \pm 1)$ are the same.

2.1.2 FDTD simulations

In order to investigate the influence of Rayleigh anomalies, we performed finite difference time domain (FDTD) simulations of different gratings. For this purpose were used two commercially available softwares: OptiFDTD from Optiwave [[Optiwave](#)] and FDTD Solutions from Lumerical Solutions [[Lumerical](#)]. In 2015, the first year of my thesis, Lumerical FDTD Solutions provided larger functionality and faster calculations among those two, so all future simulations were performed using only with this package.

First, we performed FDTD simulations using simple structures. Figure 2.4 shows a schematic of the model extracted from Lumerical package. A metallic particle is placed on top of a silica substrate. The plane wave source, linearly polarized, was placed above the particle and the transmission monitor was placed below, inside the substrate. For boundary conditions, in the Z-direction a perfect matching layer was used, in the X- and Y-directions periodic boundary conditions were set in order to simulate a grating.

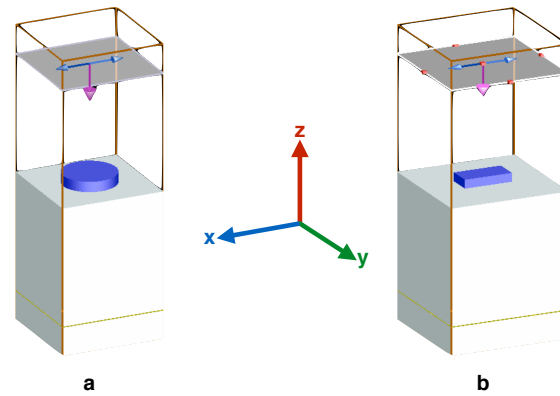


FIGURE 2.4: Model of FDTD simulation extracted from the software. (a) a metal nanodisk, (b) a metal nanorod.

In figure 2.5 the extinction spectrum is plotted, defined as $E_x(\lambda) = 1 - T(\lambda)$ where $T(\lambda)$ is the transmittance spectrum computed with FDTD. Extinction spectra have been plotted for different values of the period of the grating (i.e. the center-to-center distance between neighbouring particles in the grating). A clear dependence of the spectrum on the period can be seen. Those spectra were obtained for aluminum nanocylinders with $r = 50$ nm and height $h = 50$. At the air-glass interface where the array is located appears two Rayleigh anomalies, in glass and in air. These anomalies are located at different positions because of different refractive indices. For small periods, the resonance position of the array, observed as a maximum in the extinction, is very close to the LSP resonance of an isolated particle. With increase of the pitch, the resonance position red-shifts. The quality factor of the resonance also increases drastically. Moreover, the lineshape is modified, from a relatively symmetric shape to a Fano-like lineshape.

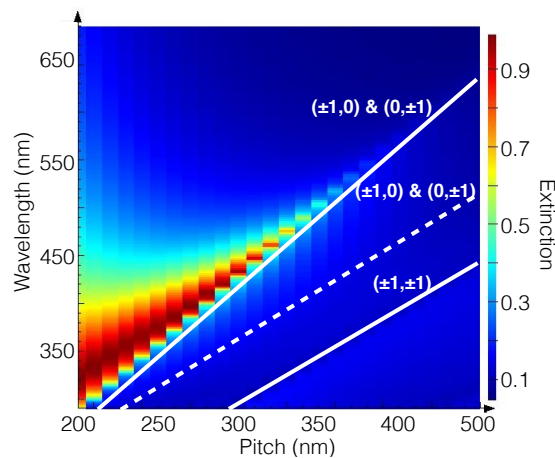


FIGURE 2.5: Extinction spectra as a function of the period, for a grating made of aluminum cylinders with $r = 50$ nm at normal incidence. The particles are placed on the glass substrate with air as the superstrate. Solid lines represent Rayleigh anomalies in glass. Dashed lines represent Rayleigh anomalies in air.

The field maps show in figure 2.6 is plotted the normalized electric field modulus, computed at the wavelength corresponding to each of the modes, for different periods. The first column corresponds to a period of 250 nm, where the Rayleigh anomaly is placed at 375 nm. The second column in the figure corresponds to a lattice period of 300 nm. In both cases, very sharp resonances, with $Q = 7.4$ and $Q = 13.1$ respectively, are observable. The field maps evidence an enhanced field along the polarization direction and a standing wave (Rayleigh anomaly) in the perpendicular direction. Within the spectrum in Fig. 2.6e we can see complete destruction of the plasmonic resonance. Observed peak, demonstrating coupling with the (1,1) Rayleigh anomaly, propagating at 45° for the axes of the array.

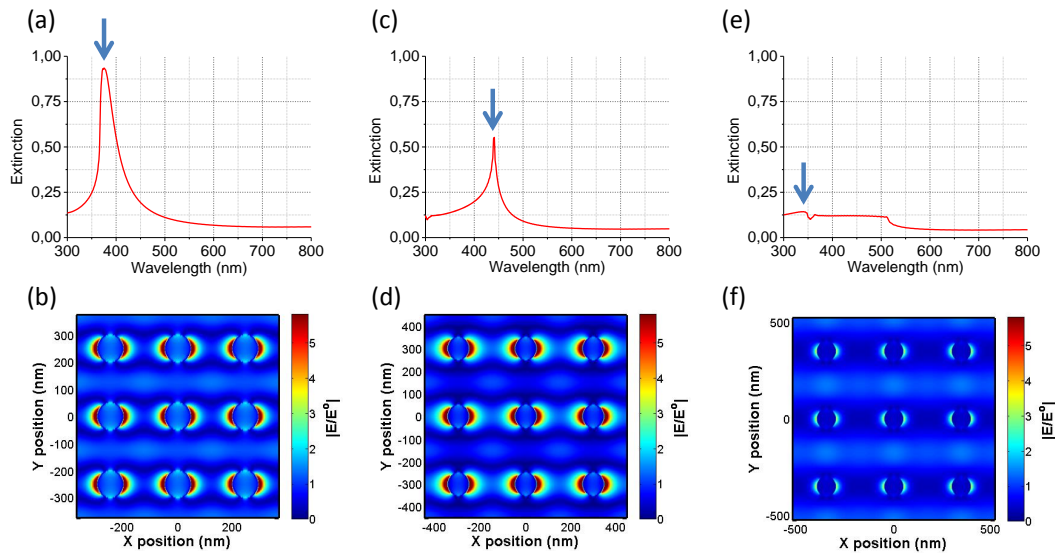


FIGURE 2.6: Normalized electric field modulus maps for different lattice periods. The insets on the top of each of the columns are line cuts of Fig. 2.3, showing the extinction $E_x = 1 - T$ versus wavelength for three different periods: $D = 250$ nm (left column), $D = 300$ nm (center column), and $D = 350$ nm (right column). The arrows indicate the wavelengths where the field maps were calculated.

Back on figure 2.5, with a small period of 200 nm, the influence of Rayleigh anomalies is weak and the inter-particle distance is large enough to neglect near-field coupling, quality factor of the LSPR is $Q_{air-glass} \approx 3$ for air-glass system. But in the area of strong coupling quality factor could reach values of $Q_{glass} \approx 13$. This is more than a 4 times improvement!

2.2 Experimental methods

In order to experimentally investigate the influence of Rayleigh anomalies on the plasmonic resonances in periodic arrays, we produced several samples with aluminum particles and different sizes.

2.2.1 Fabrication

In order to get well-shaped aluminum nanoparticles Electron Beam Lithography (EBL) was used as a fabrication method. The schematics of this procedure can be found in figure 2.7. E-beam lithography is a fabrication method where a pattern is written on the surface of a sensitive film (resist) by a focused beam of electrons produced by an electronic microscope. After exposure, the solubility of the resist is changed, allowing development of the exposed areas (in the case of a positive resist) or the unexposed areas (in the case of a negative resist). The principle is the same as photolithography, the only difference being the use of an electron beam instead of light. This enables an increase of the resolution thanks to the higher energy of electrons in comparison with photons.

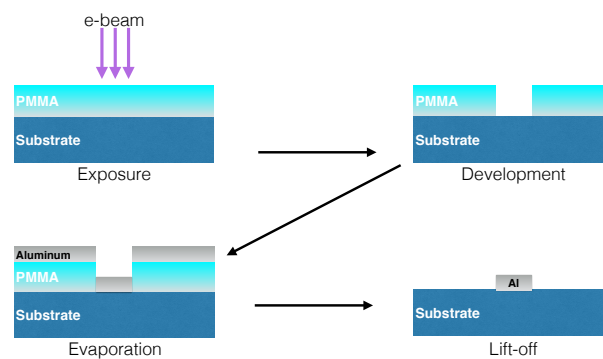


FIGURE 2.7: Schematics of fabrication process with Electron-beam lithography procedure.

As substrates, we used quartz coverslips (Agar scientific). They were covered with layers of poly(methyl methacrylate) (PMMA) solved in methyl isobutyl ketone (MIBK), a common solvent for PMMA, with concentration 30g/l. Polymer was deposited by spin-coating on the substrate with the following parameters: speed 3000 rpm, acceleration 4000 rpm/s, time 30 s. Those settings should provide a 200 nm layer of polymer. Spin-coating was followed by baking on a hot plate during 15 min at 170°C. Since neither glass nor PMMA layer are conductive materials, under the irradiation with the electron beam electrical charges will be stored inside. This would lead to the well-known "charging" effect, creating interferences with the electron microscope and drastically decreasing the resolution of the process. To avoid this, samples were additionally covered with a thin (5 nm spin-coated with same parameters as PMMA) layer of conductive polymer (Espacer 300Z) and baked for 1 min at 90°C.

Then, the samples were irradiated with an electron beam microscope. A setup consisting of a Hitachi S3500 microscope fitted with an EBL control unit "NanoPattern Generation System" (NPGS) was used for this study. The operating parameters were: voltage 10 kV, beam current 10 pA and dose range 400 – 600 $\mu\text{C}/\text{cm}^2$. Pattern designs were prepared in advance through the NPGS module. The writing process is automatic and takes from several minutes to several hours depending on the size of the pattern.

After exposure, the next stage is to develop the resist. Development of PMMA was performed using a 1:3 solution of MIBK and isopropyl alcohol (IPA). The samples were first immersed in water during 30 s to rinse the conductive polymer. Process continues with 60 s in MIBK+IPA and finished with IPA to passivize development process. After this step, the preliminary results of the lithography process can be observed with an optical microscope. Then a 50-nm-thick aluminum film is deposited on the samples, using a thermal evaporator Plassys ME300. Next, the sample is immersed into an acetone bath to remove the rest of resist, before being finally cleaned with toluene.

As a result, patterns of aluminum nanoparticles with different shapes were obtained. The schematics of the samples and some scanning electron microscope (SEM) and atomic force microscope images are presented in figure 2.8.

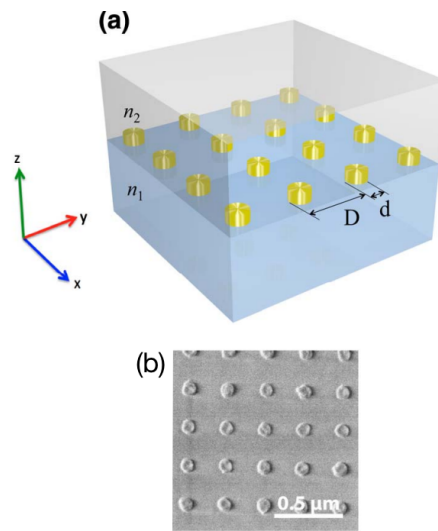


FIGURE 2.8: a) Schematic of the considered geometry: an array of metal nanoparticles deposited onto a dielectric substrate of refractive index n_1 . The superstrate can be air or a dielectric with refractive index n_2 . (b) Scanning electron microscopy image of an array of aluminum nanodisks with $D = 300$ nm, $d = 120$ nm, and $h = 50$ nm. Extracted from Khlopin et al., 2017.

After fabrication aluminum samples were covered with another 200 nm layer of PMMA to prevent oxidation and create homogeneous refractive index environment.

2.2.2 Optical measurements

The optical measurements were performed in the laboratory of our collaborators at King's College London. Their extinction spectroscopy setup provides an angle resolution combined with a wide operating wavelength range from UV to near-IR. As a light source, a lamp Avalight-DHS (Avantes), is slightly focused onto the sample, which can be rotated by a controllable angle θ with regards to the incident beam and angle step of 2 degrees. The light transmitted by the sample is collected using a microscope objective lens (MPlan UV $50\times$, Mitutoyo) confocally coupled to an optical fiber (solarization-resistant fused silica fiber, core diameter $100 \mu\text{m}$) to define a collection area corresponding to the sample size. Finally, the

output of the fiber is sent toward a spectrometer (IsoPlane SCT320, Princeton Instruments) equipped with a cooled camera (ProEM 1600², Princeton Instruments). Schematics of the setup can be found in figure 2.9. As a consequence, this setup allows us to retrieve the dispersion curves of the plasmonic resonances supported by the array. In the following, the dispersion curves are plotted as functions of angle and wavelength.

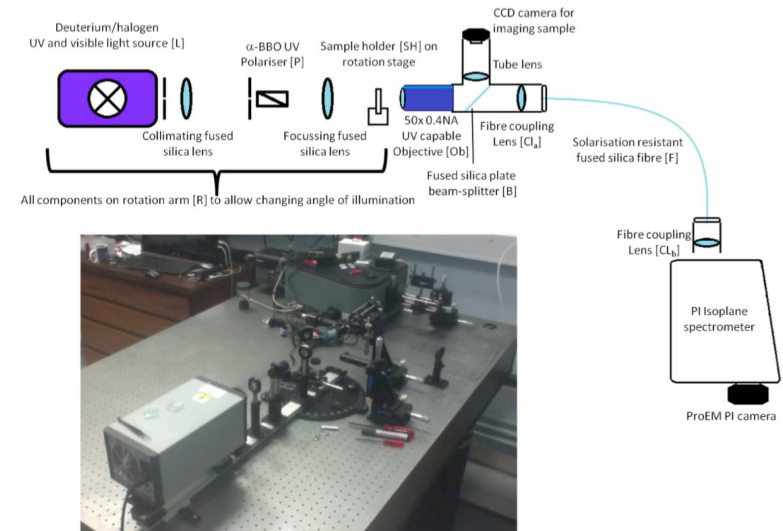


FIGURE 2.9: A schematic diagram showing the key components of the optical setup used to collect ultraviolet spectra. Extracted from Wardley, 2016.

First, we present results concerning aluminum nanodisk arrays. We designed several patterns to obtain a resonance wavelength in the visible range. The diameter of the cylinders is $d = 120$ nm and the period takes values of 250 nm, 300 nm and 350 nm. In figure 2.10 measurement of those three patterns under S - and P -polarized light excitation is presented. S -polarization: electric field is normal to the plane of incidence, P -polarization: electric field is parallel to the plane of incidence.

In figure 2.10 Rayleigh anomalies in glass and in air shown by solid and dashed lines, respectively. The two polarizations exhibit slightly different behaviors. The P -polarization shows a broad and relatively flat dispersion branch corresponding to the plasmon resonance of this branch, while for S -polarization, an interaction with the (1,0) glass/air Rayleigh anomaly appears. The most important difference between P - and S -polarizations concerns the (+1,0) glass/air anomaly. In S -polarization, the anomaly has a detrimental effect on the plasmon branch, while in P -polarization the anomaly seems to be uncoupled with LSPR. Therefore, (0, ± 1) mode showing coupling in P -polarisation rather than in S . This effect can be explained qualitatively by considering how a single nanoparticle scatters light. If we assume the nanoparticle scatters light like a dipole, then its far-field radiation will be perpendicular to the induced polarization, which is along the polarization of the incident electric field. In other words, as each nanoparticle scatters light in a direction perpendicular to the incident polarization, it will preferentially couple with grazing diffractive orders along that direction. It is also important to mention that even when the sample is covered with PMMA layer on top to obtain homogeneous refractive index ($n = 1.5$), we still observe

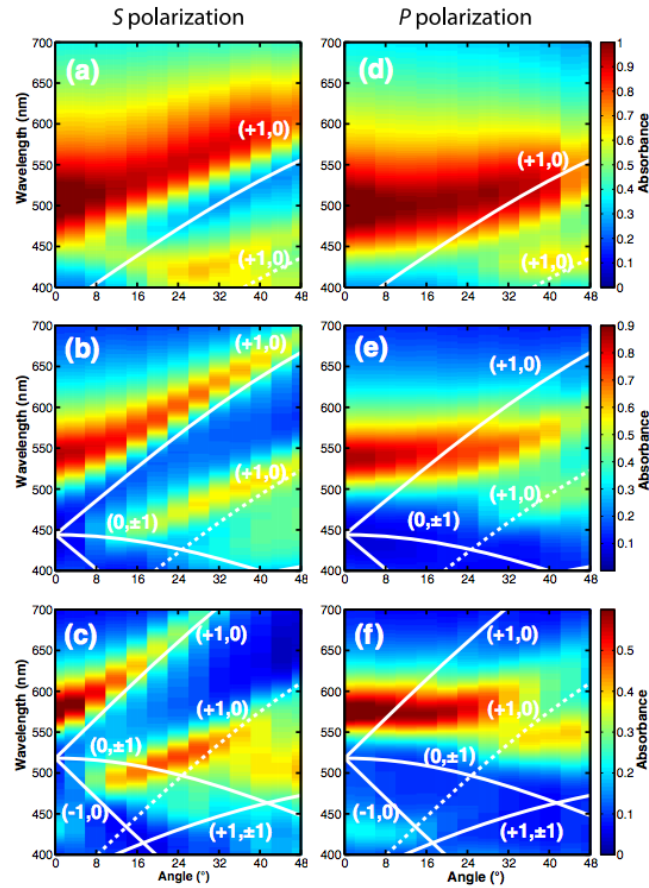


FIGURE 2.10: (a) Experimental dispersion curves of PMMA-covered aluminum nanodisk arrays for (a)–(c) s-polarization and (d)–(f) p-polarization. The diameter of the nanoparticles is $d = 120\text{nm}$. The period of the array is (a), (d) $D = 250\text{nm}$; (b, e) $D = 300\text{nm}$; and (c), (f) $D = 350\text{nm}$. White lines represent the position of the glass/glass $n = 1.5$ (solid lines) or glass/air $n = 1$ (dotted lines) Rayleigh anomalies that were computed using Eq. 2.7.

Extracted from Khlopin et al., 2017.

the presence of Rayleigh anomalies in air. It is likely due to the finite thickness of the PMMA layer and the presence of air inclusions, formed around particles [Khlopin et al., 2017].

The obtained quality factors can be compared to the quality factor obtained for isolated Al nanoparticles, which is generally $Q \approx 2 - 4$ in the visible range [Martin et al., 2014]. Hence, the linewidth engineering from lattice modes enables Q-factors to be reached that are comparable to isolated gold nanoparticles in the visible, i.e. best observed value $Q = 7.3$ at normal incidence. With angle illumination intensity of the peak decreases and it keeps the quality factor at the same or level values in comparison with normal incidence. It is also interesting to compare Figs. 2.10b and 2.10c. In the latter, the anomaly is very close to the LSP spectral position, leading to a sharp resonance at normal incidence where the intensity dramatically decreases when the angle of incidence increases. In contrast, in Fig. 2.10b, the normal incidence linewidth is higher (due to the higher frequency mismatch between the LSP and the anomaly), but as the angle is increased, the resonance sharpens without being

too detrimental to the lattice mode intensity. Consequently, if sharp lattice modes at normal incidence are sought then the Rayleigh anomaly should be designed to appear as close as possible to the LSP resonance. But if angular tolerance is required, then a minimal spectral mismatch should be introduced between the anomaly and the LSP. Moreover, in Fig. 2.10f, a small resonance is observed in blue region, which is expected to be quadripolar.

As widely discussed in the previous chapter aluminum can provide a resonance from the deep-UV. Also, in the blue and UV parts of the spectrum it provides better plasmonic properties in comparison with gold and silver [West et al., 2010]. So the next studied sample was aluminum cylinders exhibiting a small diameter $d = 60$ nm. This size is a good trade-off between fabrication limitations and requirement of small particle size. The period of the grating is $D = 260$ nm. This sample was not covered with PMMA after fabrication in order to avoid red-shift of the resonance coming from increased refractive index of environment. Figure 2.11 shows a dispersion curve for this sample. A clear interaction between the LSP resonance around $\lambda = 420$ nm and the scattered light near the (1,0) Rayleigh anomaly is observed, leading to hybridization and the appearance of a sharper resonance. Under normal incidence, we obtain $Q \approx 8$ (and more for angle illumination), a value that should be compared to $Q \approx 4$ obtained for isolated aluminum particles. In Fig. 2.11 presented an extinction spectrum for the same sample at normal incidence. Quality factor in this case is $Q \approx 13$. This experiment was performed using a freshly made sample, while the dispersion curve was made after several weeks. Oxidation of the aluminum particles appearing during this time can explain the discrepancy in the position of resonance as discussed in the previous chapter.

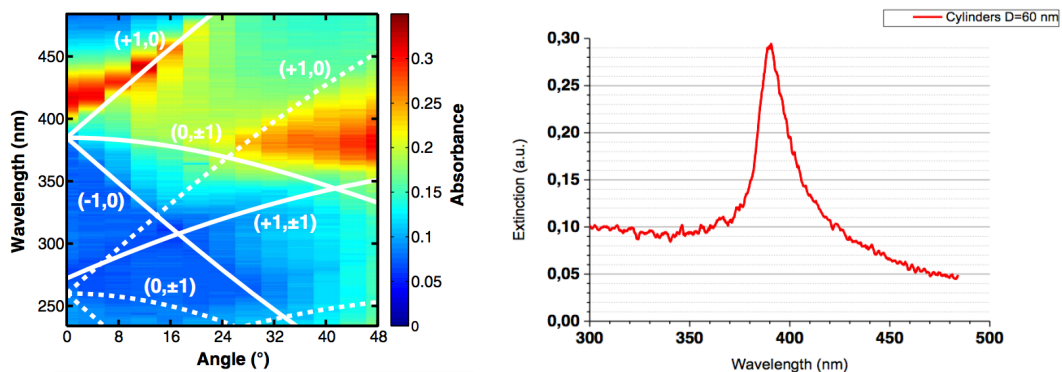


FIGURE 2.11: (Left) Experimental dispersion curve of $d = 60$ nm aluminum nanodisk arrays in the ultraviolet for S -polarization. The period of the array is $D = 260$ nm White lines represent the position of the glass/glass (solid lines) or glass/air (dotted lines), and Rayleigh anomalies were computed using Eq. 2.7. Extracted from Khlopin et al., 2017.; (Right) Extinction spectrum of the same aluminum particles under normal incidence, measured just after fabrication.

2.3 Conclusion

In this chapter, we performed simulations and experiments to understand the coupling process between localized surface plasmons and Rayleigh anomalies in dependence of material, environment, angle of incidence and polarization of the incident light. Using all of those parameters we achieved a highly tunable tool for plasmonic linewidth engineering.

The achieved quality factors Q in aluminum arrays show an increase of 5-10 times in comparison with isolated particles. FDTD simulations showed that under ideal conditions, this increase could reach 30 times. Quality factors for aluminum particles reached values comparable with non-tuned gold particles in the visible range. However, due to the higher losses and polycrystalline structure [Martin and Plain, 2015] our experimental results can be further improved to get closer to the predicted theoretical values. For instance, using the thermal annealing process mentioned in first chapter [Zhang et al., 2017].

Globally, Rayleigh anomalies do not depend on the form factor, this method of linewidth tuning is universal and can be applied to different nanostructures and metasurfaces. Altogether, we believe our results open a way for possible applications. For example SERS application of aluminum particles can be highly improved with addition of linewidth engineering by lattice modes.

In the next chapter will be demonstrated how aluminum nanoparticle arrays can be used to enhance the luminescence from wide bandgap semiconductors, such as ZnO. The lattice mode can be finely tuned to match the exciton frequency (hence enhancing the emission rate), while the array can enhance light extraction from the active layer.

Chapter 3

Aluminum plasmonics for light emission

In this Chapter I will discuss one of the applications of aluminum plasmonic structures - coupling with semiconductors to enhance light generation. The chapter is outlined as follows. Firstly, I will briefly review the properties of active materials for blue and ultraviolet light emission. Then, I will present the design of a aluminum plasmonics enhanced zinc oxide light source, and discuss the obtained experimental results. Finally I will draw some perspectives for future directions.

3.1 Wide band-gap semiconductors

Aluminum plasmonics can be applied to the whole visible spectrum apart from a small region around the interband transition (around 800 nm), but its full potential appears in the ultraviolet region. In this case, to efficiently couple with active materials, wide band-gap semiconductors should be used. The most efficient wide band-gap luminescent materials are Gallium nitride (GaN), Silicon carbide (SiC), Boron nitride (BN) and Zinc oxide (ZnO) and others. In the following, we discuss the properties of these materials.

3.1.1 Gallium Nitride

Gallium nitride is a III-V direct band-gap semiconductor widely used in optoelectronics (among other nitrides) thanks to its high stability and high temperature resistance, surpassing SiC [Morkoç et al., 1994]. This material is very important for applications in heterojunctions with other materials like Indium ($In_xGa_{1-x}N$) or Aluminum ($Al_xGa_{1-x}N$), because these crystals have a relatively small lattice mismatch. They found a lot of applications as blue emitters (LED and lasers) and in photodetection [Di Carlo, 2001]. GaN diodes in the blue and UV are now widely available.

The main method to produce high quality layers of monocrystalline GaN is molecular beam epitaxy (MBE). GaN exists in three different crystal structures: wurzite 2H type, metastable zinc-blende 3C and, very rarely, salt mine type. All of them are shown in figure 3.1.

Gallium nitride has a direct band-gap of 3.4 eV. Its band structure is shown in figure 3.2.

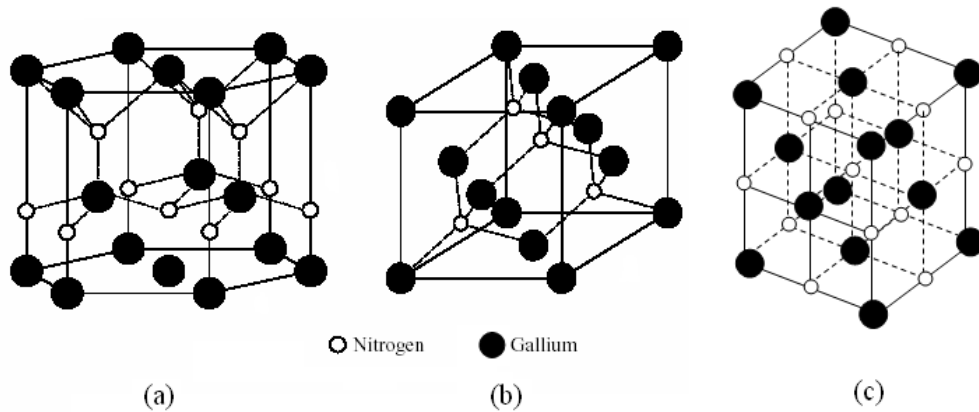


FIGURE 3.1: Crystalline structures of GaN. (a) Wurtzite structure; (b) Blende structure; (c) Salt Mine structure. Extracted from Shi, 1998.

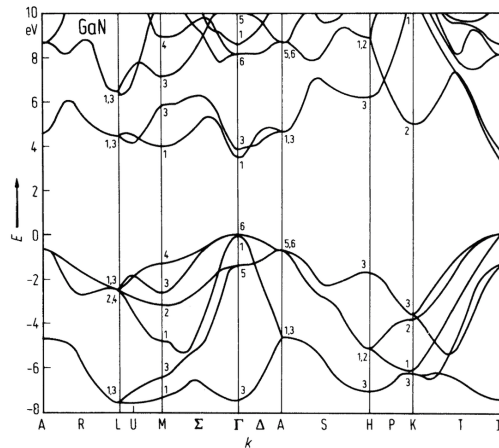


FIGURE 3.2: The band structure of wurtzite GaN. Extracted from .

One of the most famous and most important application of Gallium Nitride is efficient blue light-emitting diodes - as it was acknowledged by the Nobel prize in physics for 2014 year [Class for Physics of the Royal Swedish Academy of Sciences, 2014]. LEDs were studied since the 1950s, but the development of a blue diode was a difficult task due to the problems associated with growth and doping control in wide band-gap semiconductors. The inventors of the high efficiency blue LED, Akasaki, H. Amano and S. Nakamura, solved these problems. They fabricated a GaN film on a layer of AlN to reduce crystal lattice tension. Combined with doping using Mg and Zn [Amano et al., 1989], they were able to create an effective light emitting diode.

After this breakthrough, blue and UV light sources were widely studied and a lot of applications were developed. Several works concentrated on quantum wells made of InGaN [Tateishi et al., 2015] or AlGaN [Gao et al., 2012]. In both cases, an aluminum film was used to enhance light emission. Using the surface plasmon sustained by the aluminum film, the authors achieved an enhancement of the incoming light intensity up to 50 times. Some

results and schematics are presented in figure 3.3.

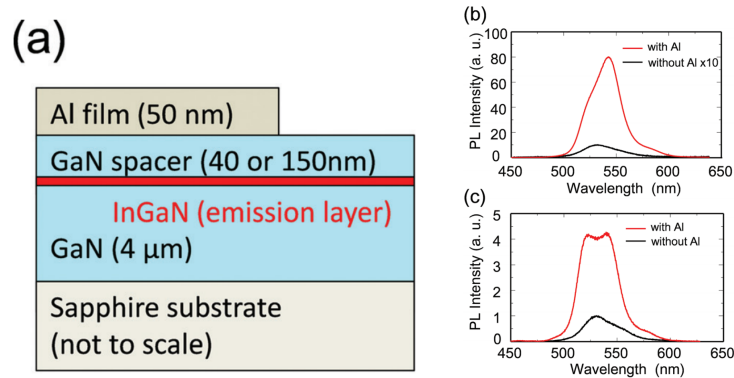


FIGURE 3.3: (a) Sample structure of the InGaN/GaN QWs with Al films. ; Enhanced PL spectra from InGaN/GaN QWs with Al films, which have GaN spacer layers of (b) 40 nm and (c) 150 nm. The PL peak intensity of the uncoated InGaN/GaN QW was normalized to unity. Extracted from Tateishi et al., 2015.

A great example of high-end engineering and science was demonstrated in the work of Lu et al., 2012. Using an aluminum film to generate a confined surface plasmon mode, they built a nanolaser based on an InGaN nanowire as the active gain material. This configuration is close to the nanolaser presented in Chapter 1 (also using GaN) but here the nanowire consists of a core-shell structure with a GaN shell and an InGaN core. A schematic of this concept is presented in figure 3.4. With this structure, the authors observed laser emission at an operating wavelength of 510 nm.

3.1.2 Boron nitride

Boron nitride is also a III-nitride wide band-gap semiconductor. It exists in multiple structure types that are similar to the structures of carbon []:

1. a-BN - amorphous form. Non-crystalline arrangement. Similar to amorphous carbon.
2. h-BN - hexagon form. The most stable form of boron nitride. It is analogous to the graphite structure.
3. c-BN - cubic form. It is diamond out of boron nitride. It is softer than carbon diamond but has improved thermal stability.
4. w-BN - wurtzite form. A rare type with the same structure as lonsdaleite. The most dense lattice among other types.
5. There are other forms of this material, like rhombohedral, but they are rare materials with a high difficulty of production.

In optoelectronics, the h-BN structure is mainly used. It has a high thermal conductivity and it is easier to produce monocrystalline layers than with aluminum nitride. Since seminal

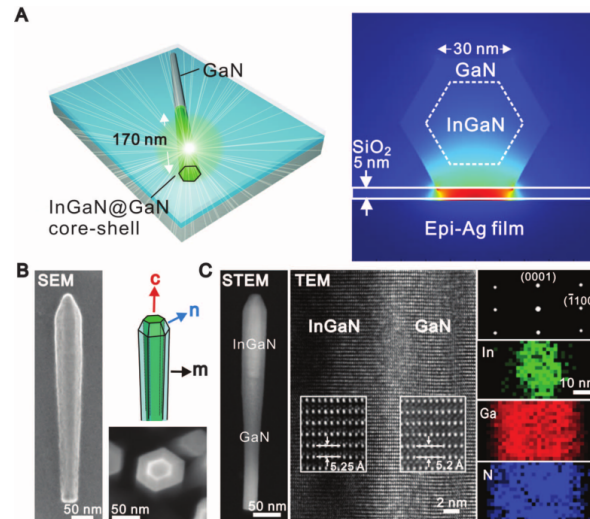


FIGURE 3.4: (A) Schematic of the device: a single InGaN/GaN core-shell nanorod onto a SiO₂-covered epitaxial Ag film (28 nm thick) (B) SEM images of InGaN/GaN core-shell nanorods. The left-hand SEM image shows the actual nanorod on epitaxial Ag film that was used for all lasing measurements. (C) Scanning transmission electron microscopy (STEM) and transmission electron microscopy (TEM) structural analyses of a single-crystalline InGaN/GaN core-shell nanorod. Extracted from Lu et al., 2012.

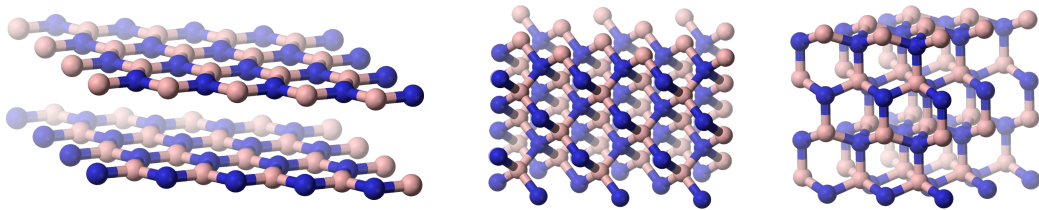


FIGURE 3.5: From left to right: Hexagonal form (h-BN), Cubic form (c-BN), Wurtzite form (w-BN). Extracted from **Wikimedia**

experiments demonstrating a laser emission at 215 nm in monocrystalline sample under e-beam excitation [Watanabe, Taniguchi, and Kanda, 2004], h-BN was thought to exhibit a direct band-gap of 5.2 eV. However, recent experiments performed on high-purity crystals evidenced that h-BN actually has an indirect band-gap of 5.995 eV [Cassabois, Valvin, and Gil, 2015]. Boron nitride also luminesces with an excitation of $\lambda_{exc} \approx 248$ nm. With excitation at 262 nm Larach and Shrader, 1956 observed a fine-structure luminescence in the range 300-500 nm. Zunger and Katzir, 1975 have observed a blue PL continuum in the range 390-500 nm ($\lambda_{exc} = 320$ nm).

Previously, we mentioned the similarity with carbon structures. Actually this similarity leads to the creation of 2D and 1D-materials out of boron nitride in analogy with carbon nanomaterials [Bourrellier et al., 2014]. There are monolayers of h-BN (similarly to graphene) and also h-BN nanotubes. h-BN nanostructures emerged recently for optoelectronic applications in the deep UV region [Jaffrennou et al., 2007][Jaffrennou et al.,

2008][Watanabe et al., 2009][Arenal et al., 2005]. Low-dimensional BN systems sustain very interesting properties: high mechanical stiffness and high thermal conductivity, strong deep ultraviolet emission, thermal and chemical stability. It is therefore clear that h-BN nanostructures are promising for the development of robust, stable and efficient future nanodevices operating in the deep ultraviolet. Their plasmonic engineering is very attractive due to the possibility to couple them with a metallic nanostructures in order to tune their excitonic properties.

3.1.3 Zinc oxide

Zinc oxide is a direct band gap semiconductor, II-VI binary material strongly absorbing in the UV and transparent in the visible and near infrared. It crystallizes in three types of lattices: rocksalt, zinc blende and wurtzite (all of them are shown in figure 3.6). At ambient conditions, wurtzite structure is the most stable and common.

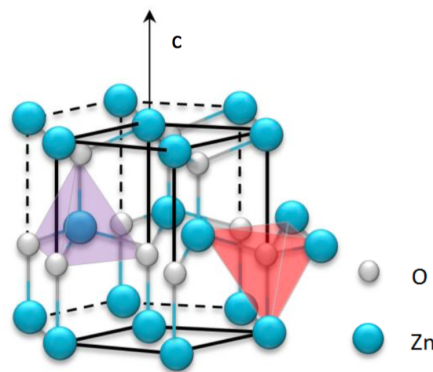


FIGURE 3.6: ZnO wurtzite crystal lattice. Extracted from Nomenyo, 2014.

Thanks to its transparency in the visible and high resistivity, ZnO is widely used in nanotechnology as a mask for lithography. In polycrystalline form, it usually appears as a white powder and is used as an additive in numerous materials and products including plastics, ceramics, pigments, batteries and many others. A very important point for the applications, ZnO is also a non-toxic and antibacterial material.

The band-gap of zinc oxide is direct and 3.4 eV wide. This should provide emission of photoluminescence around a wavelength of 380 nm (excitonic peak). However, in reality there is also a very broad emission in the visible. The wide range of emission in the visible area is associated with defects in the ZnO crystalline structure: point defects (such as vacancies and interstitial defects), linear defects (such as dislocations) and planar defects (surface). These defects appear in the crystal during the production cycle. The luminescence emission from these defects covers several wavelengths in the visible part of spectrum, as it can be seen in figure 3.7 .

Zinc oxide nanostructures provide a number of interesting properties: excellent temperature/radiation resistance, and tunable resistivity. In combination with its large exciton binding energy (≈ 60 meV) at room temperature, ZnO becomes a perfect candidate for a

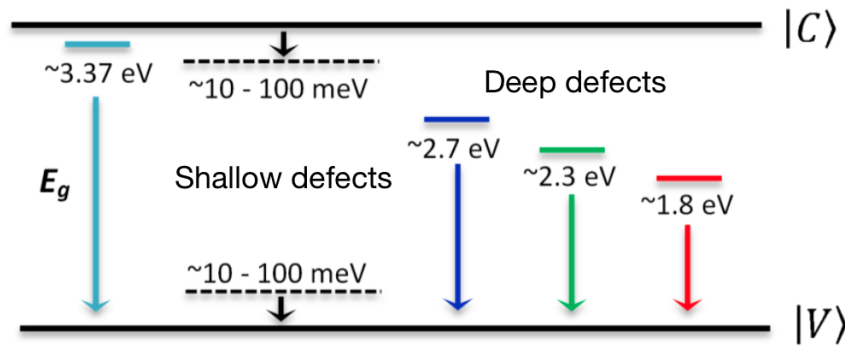


FIGURE 3.7: Schematics of energy levels of defects in ZnO. Extracted from Nomenyo, 2014.

variety of applications such as low-threshold excitonic lasers in UV region [Nomenyo et al., 2014].

In the literature, several works about coupling of ZnO with plasmonic structures have already been reported. Several configurations can be realized:

1. The aluminum film (or Al nanostructures) can be located under a zinc oxide layer, i.e. between substrate and ZnO layer. For example, in the work of You et al., 2008, a silver film was placed under the ZnO layer. They reported a total enhancement of photoluminescence reaching a factor of 45 at $\lambda = 380$ nm with a silver film thickness of 120 nm. Another example is the work of Norek, Łuka, and Włodarski, 2016, where a hexagonal lattice of aluminum particles was used. In this configuration the quality of the metal layer is critical and usually an epitaxial deposition is required. The roughness of a thermally evaporated aluminum layer can lead to an increased quantity of defects inside the ZnO layer, increasing the losses and broadening the emission spectrum. Moreover, the high refractive index of ZnO in the ultraviolet range (in average 2.4) causes a redshift of plasmonic resonance wavelength. As a consequence, smaller particles are needed to match the ZnO emission wavelength.
2. Metal nanoparticles can be placed on the top of the zinc oxide film. In this configuration there is no risk of deteriorating the crystallinity of ZnO, but the production of these structures strongly relies on the smoothness of the ZnO surface – if it not the metallic film or particles will not have reproducible shape and quality. Hence, using an epitaxial layer of zinc oxide is the best option. An example is the work of Cheng et al., 2009, where a 40-nm-thick silver layer is on the top of a ZnO film. A huge drawback of this configuration is that the metal (silver or aluminum) is exposed to air and hence not protected from oxidation.
3. An efficient configuration for coupling is to use a nanowire of ZnO on top of the Al layer [Chou et al., 2015]. This is analogous to the GaN nanolaser structure showed before in Fig. 3.4.

4. There are a lot of other possible combinations of Al nanostructures with ZnO nanostructures, for example work of Puraahmad, Stroschio, and Dutta, 2012. But most of them are more complicated in terms of fabrication. Some of them will be described later in this Chapter in a "Conclusion and Perspectives".

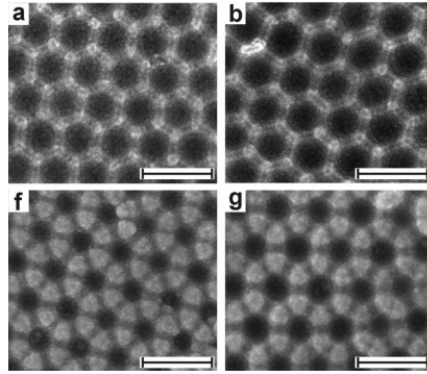


FIGURE 3.8: Some examples of hexagon lattice of aluminum nanoparticles under ZnO layer. Extracted from Norek, Łuka, and Włodarski, 2016.

In our laboratory, colleagues have a strong expertise of fabrication and characterization of ZnO structures [Nomenyo et al., 2014][Gokarna et al., 2014][Divay et al., 2008]. Different nanostructures can be produced using our colleagues facilities: Thin films [*Nanovation*], nanodisks [Nomenyo et al., 2014], nanopillars [Nomenyo, 2014], urchin-like structures [Gokarna et al., 2014] and others. This provides a good platform for studies of the coupling between wide band-gap semiconductors and aluminum.

3.2 Design of the structure

To study aluminum plasmonics for the emission enhancement from a wide band-gap semiconductor, the zinc oxide was chosen due to its availability in our laboratory. It exhibits very promising properties and already proven coupling compatibility. Besides, the strong expertise from the colleagues is a huge advantage.

3.2.1 Theory of enhancement

As previously discussed in Chapter 1, apart from the dependence of emission intensity on the incoming excitation, the electromagnetic environment surrounding the emitter plays a major role. In 1946, E.M. Purcell published a short note where he described a phenomenon called nowadays "Purcell effect" [Stephens, 1946]. In his original note, Purcell described the enhancement of an emitter's spontaneous emission rate by a cavity but more generally, the Purcell effect stems from the modification of the local density of optical states (LDOS) around the emitter.

Generally speaking, emission appears due to the relaxation from an excited state to the ground state. As well presented in [Colas des Francs et al., 2016], one can introduce a "cooperativity parameter," describing the efficiency of light-matter interaction. Inside a cavity made in an homogeneous medium of optical index n_1 , the cooperativity parameter can be written for a single atom as:

$$C = \frac{g^2}{2k_{cav}n_1\Gamma_0} \quad (3.1)$$

where g is the coupling rate between the atom and the cavity mode, k_{cav} is the cavity losses and Γ_0 refers to the atom decay rate in vacuum. In this case, the Purcell factor F_p represents the effect of the cavity:

$$F_p = \frac{\Gamma_{cav}}{n_1\Gamma_0} = 2C \quad (3.2)$$

where Γ_{cav} is the modification of the decay rate due to the optical cavity. The above equation can be written in the more well-known form Stephens, 1946 :

$$F_p = \frac{3}{4\pi^2} \left(\frac{\lambda_{em}}{n_1} \right)^3 \frac{Q}{V} \quad (3.3)$$

where Q is the quality factor of the cavity, V is a modal volume involved in the coupling and λ_{em} is the emission wavelength of the atom. G. Colas des Francs et al. made an excellent work to adapt Purcell factor for the plasmonics. Metal nanoparticles excited at their plasmonic resonance create a local change in the photonic density of states, in a similar fashion to optical cavities. In summary, the Purcell factor for metallic particles near the plasmonic resonance is proportional to the $F_p \propto Q/V$. For surface plasmons, the quality factor is estimated from the resonance spectrum profile:

$$Q = 2\pi \frac{E_{cav}}{E_{des}} = \frac{\lambda_{res}}{\Delta\lambda} \quad (3.4)$$

where E_{cav} and E_{des} are the energies stored in the cavity and dissipated per cycle, respectively. Here λ_{res} is the resonance peak wavelength and $\Delta\lambda$ is its full width at half maximum. The modal volume can be expressed as:

$$V = \frac{\int \epsilon E_n^2(r) dV}{\max(\epsilon E_n^2(r))} \quad (3.5)$$

where $E_n(r)$ is the electric field intensity at position r , and ϵ is the dielectric constant of the material. In this case the expression $\epsilon E_n^2(r)$ simply calculates the optical energy density.

Let us recall that Purcell effect is not the only possibility to get more light. The presence of a metal structure can also create a light redistribution, changing the radiation pattern (antenna effect). As discussed in the first chapter, at the plasmonic resonance the scattering cross-section reaches a maximum. This effect, for example, can be applied to solar cells: metal particles are used to scatter light and increase the light path inside the cell [Catchpole and Polman, 2008].

3.2.2 Concept of the sample

Complex plasmonic geometries comprising particles made out of different metals and/or shapes can be designed in order to allow a simultaneous enhancement at excitation and the emission wavelengths. A more detailed description of such systems are described, for instance, in [F. Laux, Bonod, and Gérard, 2017].

In our case, the chosen way is waveguiding. The refractive index of ZnO in the UV region (excitation-emission range) has a relatively high value of $n \approx 2,4 \pm 0,2$. This allows ZnO to work as a waveguide at those wavelengths, as experimentally demonstrated in [Aad et al., 2014]. (see also Fig. 3.9)

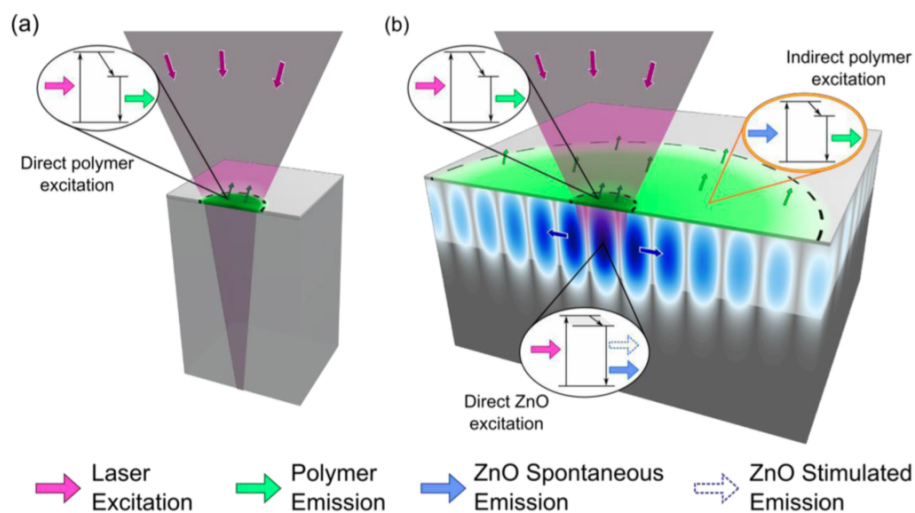


FIGURE 3.9: Artistic depiction of the gain-assisted waveguiding energy transfer (G-WET) process for ultrathin film optimized excitation as illustrated for a (polymer) luminescent thin film and an active (ZnO) layer. (a) Case of the passive substrate; (b) Case of the active layer. Extracted from Aad et al., 2014.

The use of a diffraction grating can possibly solve two issues at the same time. First of all, arrays of nanoparticles allow the tuning of the plasmon resonance wavelength thanks to the interference with Rayleigh anomaly, as described in the previous chapter, to obtain sharp lattice resonances exhibiting high quality factors. The second expected advantage is that the grating will insert more exciting light inside the ZnO layer, leading to waveguiding and efficient excitation of the active layer. Those perspectives create the concept presented in figure 3.10.

The diffraction grating located on top of the ZnO can be a 1D grating (i.e. periodic lines, see fig. 3.10b), or a 2D grating (i.e. a matrix of structures, see fig. 3.10d), or something in between that we might call a 1.5D grating (such as the dashed lines depicted in fig. 3.10c). We attempted to fabricate all these three structures, but unfortunately we encountered an issue with both the 2D and 1.5D structures. The fabrication was done using e-beam lithography and lift-off method, with PMMA as a positive resist. Due to the small contact surface of non-exposed polymer after e-beam irradiation, during the development process the polymer can slip away from its position, leading a badly imprinted structure. A better solution

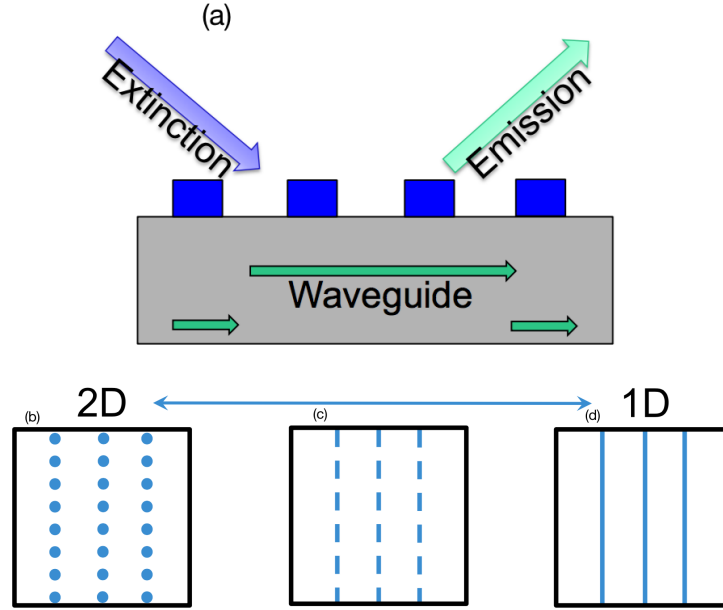


FIGURE 3.10: Schematics of the sample concept: aluminum nanoparticles located on top of the ZnO layer.

to produce such structures would be to use reactive ion etching on an evaporated aluminum surface.

In this concept, we decided to use the Rayleigh anomaly to excitation wavelength and Purcell effect to emission wavelength. For the excitation a 325 nm He-Cd laser was used. Emission is expected around 380 nm. As described in the previous chapter, the resonance wavelength of the lattice modes linearly depends on the refractive index n_2 :

$$\lambda_{RA} = D \frac{\sqrt{n_2^2(m^2 + p^2)}}{m^2 + p^2} \quad (3.6)$$

As soon as we are interested in waveguiding inside the ZnO layer, λ_{RA} should be equal to the 325 nm. According to equation 3.6, the center-to-center distance in the lattice should be 165 nm in order to obtain a first order Rayleigh anomaly at this position and provide coupling of the excitation light into the waveguide where it will be absorbed.

The second step is to tune the plasmonic resonance of individual aluminum nanoparticles in order to match the emission wavelength. As the refractive index of ZnO is high, it redshifts the resonance and we have to decrease the size of the nanoparticles. FDTD simulations of the basic cylinders were performed with the model. The refractive indices of aluminum and alumina were taken from Palik, 1997. In this simple numerical model, the 150-nm-thick ZnO layer was not modelled as an active material but as simple dielectric with a purely real refractive index set to 2.4. This system sits onto a sapphire substrate. The boundary conditions are periodic in the XY plane and PML in the Z-direction.

The results of the optimization demonstrated that cylindrical particles with a diameter of 40 nm and a height of 50 nm can be used for enhancement. Let us underline that such nanoparticle sizes correspond to small particles, at the limit of what can possibly be made

using standard procedures of e-beam lithography.

To sum up, a basic concept of the sample has been developed and optimized. Its main characteristics are: relatively thick zinc oxide film on top of the quartz or sapphire substrate, aluminum cylinder particles with diameter 40 nm and height of 50 nm on top of the ZnO layer. A 3D picture of our design is shown in figure 3.11. A possible issue remains, as our model neglected light absorption inside the ZnO layer (the imaginary part of its dielectric permittivity was set to zero). Active bulk materials are difficult to model and it is hard to predict the possible impact of the absorption on the enhancement factor. Hence, the experiment is required to see what kind of enhancement factor can be achieved.

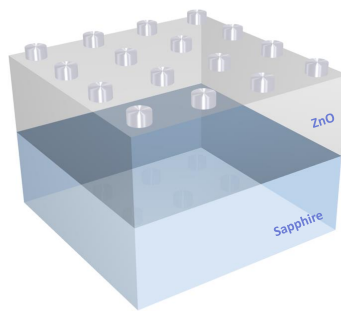


FIGURE 3.11: A schematic representation of the sample.

3.3 Experimental results

To experimentally validate the proposed design, we fabricated a sample based on the previously described concept. In this section we will discuss the fabrication procedure and results from the measurements.

3.3.1 Fabrication of the sample

To realize the sample, we used an epitaxial layer of zinc oxide. Molecular beam epitaxy is a method of deposition of thin films with high crystalline quality. ZnO was grown in our collaborator's company Nanovation [*Nanovation*]. The thickness of the layer is 150 nm, and it is grown on a sapphire substrate. The 150-nm-thickness is high enough to provide waveguiding in a monocrystalline layer. The next step is electron beam lithography. The surface of epitaxial ZnO is smooth enough to perform the lithography directly on it. The substrate was spincoated with a 150-nm-thick Poly(methyl methacrylate) layer. As ZnO is a semiconductor, there is no need of a conductive polymer. The main parameters of the e-beam lithography are summarized in the following table 3.1. Moreover, the use of ZnO as a substrate allows to perform a better alignment of the e-beam microscope. Hence, fabrication of small structures (40 nm in diameter) should be possible.

Voltage	20 kV
Current	30 pA
Aperture	10 μm
Dose	200 $\mu\text{C}/\text{cm}_2$

TABLE 3.1: E-beam lithography parameters used for fabrication.

In figure 3.12 are shown representative SEM images of the fabricated particles. To avoid any contamination of the sample, electronic microscopy was performed *after* the optical study. The shown pattern has a high-quality particles with diameter of 40 nm. Also we observed an unexpected issue in the lithography process leading to elliptical particles in one of the patterns. The large axis of the ellipse is rotated by 45° from the lattice axis and is 60-nm-wide, while the width of small axis is 40 nm.

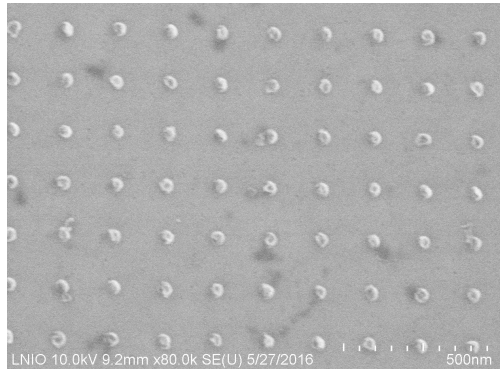


FIGURE 3.12: SEM image of aluminum nanocylinders $d=40$ nm fabricated on top of the ZnO layer.

3.3.2 Optical analysis

Photoluminescence measurements were performed on an optical setup made in our laboratory. It is based on a continuous wave He-Cd laser (Coherent) emitting at a wavelength of 325 nm with a 10 mW power. The probing spot is very small and for the best alignment conditions its diameter is about 1 μm . In comparison with the pattern size (30 μm) this is relatively small. Detection and spectral analysis are performed by spectrometer (Princeton Instruments Advanced SP2500A). A schematics of the setup is shown in figure 3.13.

The first measurement was made on the cylindrical Al particles. As presented in figure 3.14a, where the red line corresponds to the PL emission with particles and the black line to the PL emission of the pristine ZnO sample, there is an obvious enhancement of the signal. The spectra are presented here without any normalization of the signal and the observed enhancement is not that large – 50% for the best conditions, as can be seen in fig. 3.14b. Note that in this case the plasmonic resonance was perfectly aligned with the emission wavelength. The position of the plasmonic resonance was computed using FDTD as the difference between transmission spectra with and without particles. matching of the

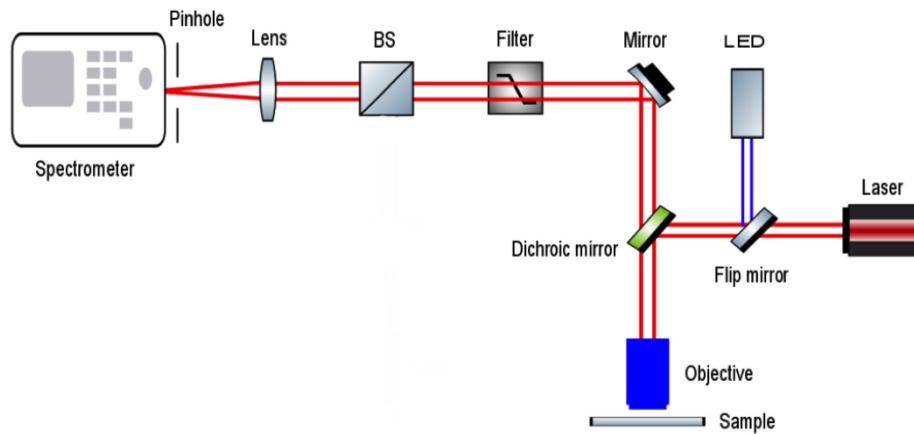


FIGURE 3.13: Schematics of micro-Photoluminescence setup. Extracted from Rahbany, 2016.

resonance with emission wavelength leads to the increase in the outcome light with Purcell and antenna effects described before. Issues will be discussed later.

A side result concerns elliptical aluminum particles (fig. 3.15). On the raw data it is hard to see any enhancement, rather a small and wide bump around 390-395 nm. But in figure 3.15b, where an enhancement ratio is shown, it becomes clear that enhancement is there and it almost as high as for cylinders. The only difference is that due to the bigger size of the aluminum structures it redshifted. The enhancement spectrum of elliptical nanoparticles shows a good correspondence also with plasmonic response calculated via FDTD simulations and presented in figure 3.15c. In that case the plasmonic resonance is redshifted in comparison emission wavelength the Purcell and antenna effects becomes less effective at 380 nm (also local field intensity drops down) leading to the small effect on the peak. Those effects become more valuable at ≈ 395 nm where the plasmonic resonance is placed, but with a lack of light it becomes harder to detect.

3.3.3 Discussion and outlook

The experimental results show a moderate enhancement of the luminescence by the aluminum nanostructures. Its value for the best conditions is only 1.5. This result is clearly lower than our expectations and deserves explanation. First of all, the Purcell and antenna effects are localized around the particles. In other words, the plasmonic modal volume from where enhancement effects could be observed is relatively small. On the other hand, we have a quite thick layer of zinc oxide (150 nm) when compared to the penetration depth of the localized surface plasmon field (a few tens of nm). This means that most of the active material is *not* coupled to metal particles. The spatial distribution of the electric field, obtained from FDTD simulations, can be seen in figure 3.16. To compensate the influence of the uncoupled volume, a normalization can be performed. The coupled and uncoupled volumes are estimated by field profiles obtained from simulations and expected to be in the

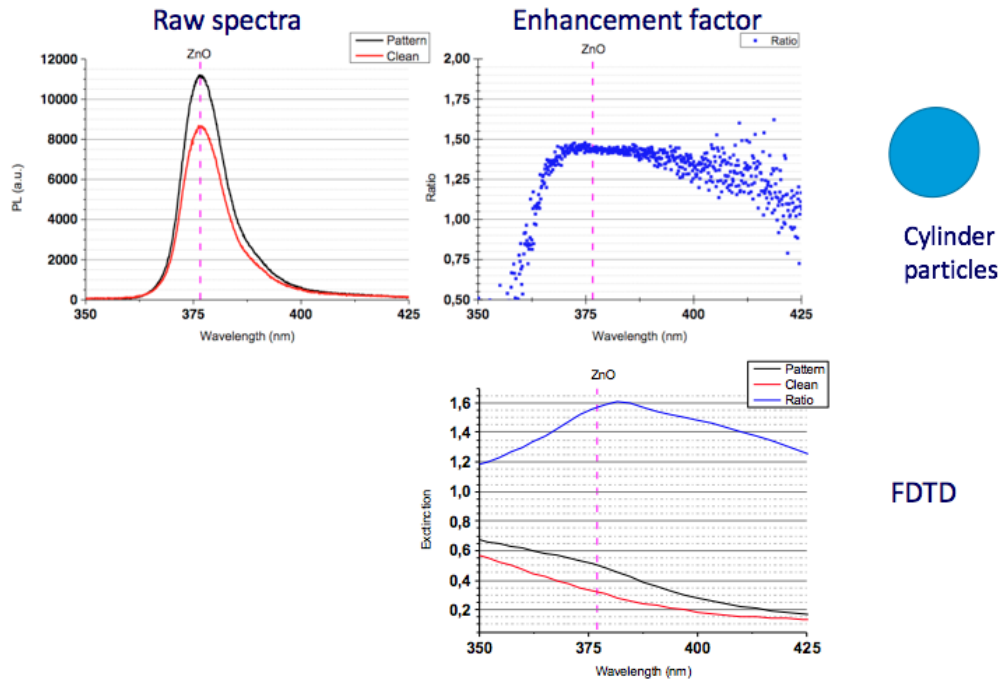


FIGURE 3.14: (a) Spectra of photoluminescence of the ZnO with cylindrical aluminum particles. Black line - intensity of emission with particles I_p , red line - without particles I_o ; (b) Enhancement ratio $R_e = I_p/I_o$; (c) Extinction spectra simulated with FDTD.

same order as the particle volume. With these parameters, the normalized enhancement factor peak value is around 10. This value is closer to our initial expectations.

The second issue is connected with the second concept: waveguiding. Our experimental setup cannot provide measurements of photoluminescence from the edge of the sample. In our hypothesis, there is an increase of the side emission due to waveguiding within the layer of ZnO, that is not measured in the obtained spectra (measured from the top). Such an edge-emission has been observed during the experiments, as light can be seen with the naked eye emerging from the side of the sample when the exciting spot is located onto a patterned area. In contrast, almost no side emission was observed when the excitation spot was located on pristine ZnO.

Surely for the realization of a practical device, the most important figure of merit is the total amount of luminescence, without any normalization trick. To obtain useful results without normalization of data, there are several possible ways:

1. The most obvious solution is decrease the thickness of the ZnO layer. But with decrease of thickness waveguiding would be less effective.
2. Also it is possible to etch the ZnO layer, in order to put the metallic nanoparticles inside the active material layer. This would greatly increase the modal volume. Unfortunately, ZnO is used to create lithography masks as it is very robust to etching. This will definitely leads to a lower quality of fabricated particles, as well as the creation of defects inside the ZnO crystalline structure, decreasing its efficiency.

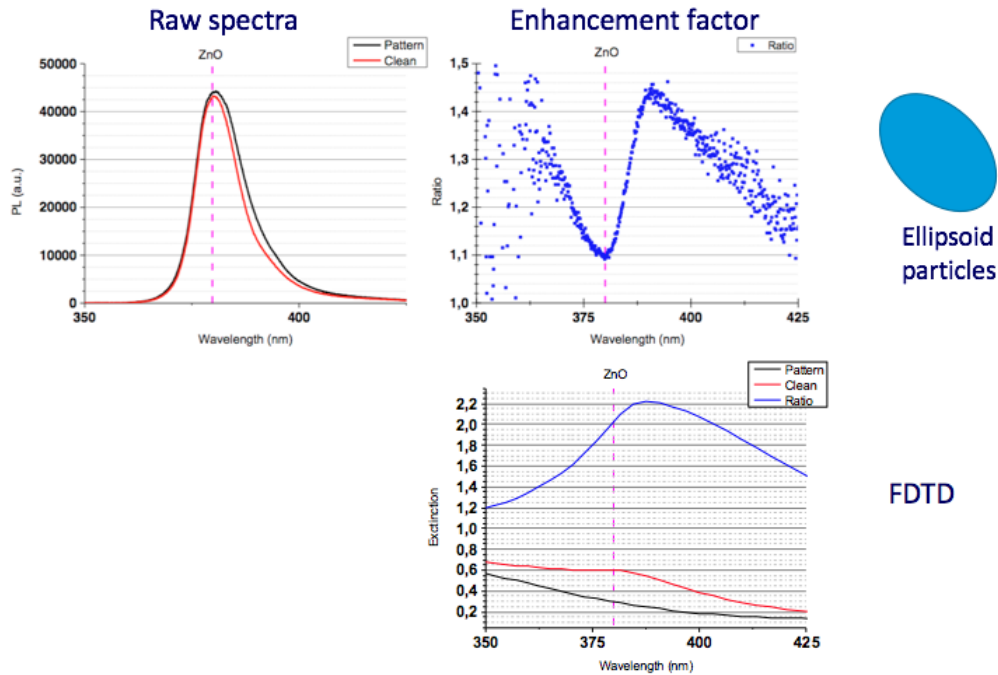


FIGURE 3.15: (a) Spectra of photoluminescence of the ZnO with ellipsoidal aluminum particles. Black line - intensity of emission with particles I_p , red line - without particles I_o ; (b) Enhancement ratio $R_e = I_p/I_o$; (c) Extinction spectra simulated with FDTD.

3. An improvement of the setup to measure the edge emission is necessary. As well as inverse case with side illumination, where aluminum array would uncouple light from the waveguide.
4. The structure used in this experiment is a basic lattice of cylinders. Our fabrication technology allows us to produce more complex metasurfaces, which potentially will show higher enhancements with the use of the same substrate.

3.4 General conclusion

Energy efficiency now appears as a necessity for all future technologies. As future nanophotonics devices should heavily rely on ultra-compact light sources, these new light sources should also be designed to be energy-efficient. This implies the need to extract more light from the active material constituting the light source. In conventional lasers, the down-limit of the active medium is typically half the operating wavelength, leading to a minimum device size of a few hundreds of nm. In order to break this limit it has been shown that coupling the laser active medium (semiconductor alloys) with metallic nanostructures allows for the confinement of the optical energy into surface plasmons.

Aluminum nanostructures have great potential for use with zinc oxide for enhancing light generation. Even if it is not the most effective configuration, with Al nanocylinders located on the top of the ZnO layer we achieved luminescence enhancement factors of 1.5

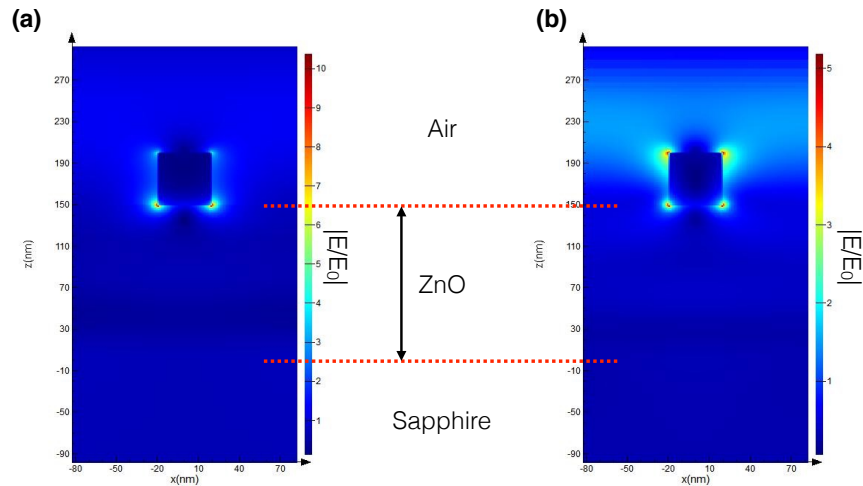


FIGURE 3.16: Field map obtained with FDTD simulations. performed for (left) $\lambda = 325$ nm and (right) $\lambda = 380$ nm

(raw) and around 30 (volume-normalized). Continuation of this work carries a great potential in structuring both of the materials. For example complex metasurfaces, that will be discussed later in this thesis. Structuring the ZnO [Nomenyo et al., 2014], or the use of ZnO nanostructures such as pillars, is also a very interesting direction. Advancing in the fabrication methods will allow to produce complex hybrid nanoobjects, such as a nanopillar onto a particle or *vice-versa* (see figure 3.17). With this structure, it should be possible to create a nanocavity inside of the pillar with the aluminum particle working as a amplifier and a mirror.

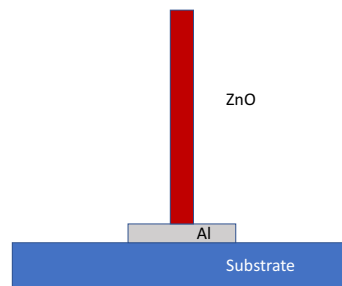


FIGURE 3.17: Schematics of a nanopillar sitting on top of a nanoparticle.

Other wide band-gap materials, discussed previously, should not be forgotten. Especially, we have to mention boron nitride as a wonderful candidate for photonics applications in the deep ultraviolet region. PLanar (2D) BN structures (flakes) can be coupled with Al plasmonic nanostructures as, for example in figure 3.18. Proposed BN-Al model can deliver interesting properties for deep UV-light generation.

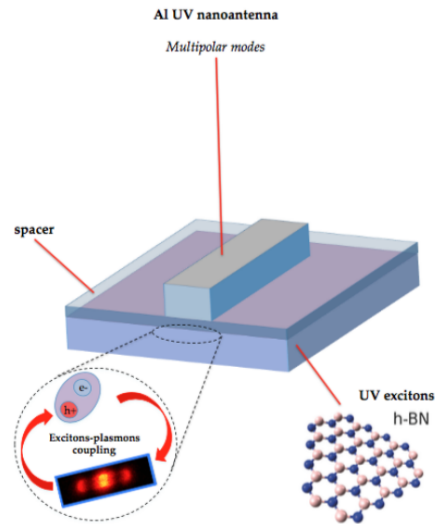


FIGURE 3.18: Proposed structure aiming at combining UV plasmonic resonances in aluminum nanoantennas with excitons in h-BN nanostructures. Aluminum nanorod placed onto h-BN flake with a spacer layer in between. With aluminum nanorod multimodal plasmonic resonances [Martin et al., 2014] can be used to enhance emission from boron nitride.

UV nanophotonics is very important for the biological research and medical applications. Nanodevices based on ZnO and Al are non-toxic and can be used for in-viva investigations. Theranostics discussed in introduction is also rely on nanosources for local detection and curing directly inside the human body. A very recent step in this direction is a work of J. Kunz et al., 2017 where UV-light is used to kill bacteria. With further study and fruitful collaborations project of AlumOnics (Aluminum photonics) can be widely applied in different research fields.

Chapter 4

Fractal plasmonics

The relatively low efficiency of the plasmonic photoluminescence enhancement observed in Chapter 3 is a general problem when dealing with bulk or thin film emitters. This limitation can hinder further development of an application prototype, such as a highly efficient UV diode that can be used for many industry purposes like lighting, medical treatment and diagnosis.

In order to find a solution for this problem, I adopted a solution inspired from radiowave technology: fractal antennas. In this chapter I will describe a study of using specific fractal form nanoparticles for plasmonics. After a brief introduction on fractal structures and a state of the art of their use in plasmonics, I will present the numerical simulations I used to design aluminum nanostructures for field enhancement. Then, I will show the structures I produced using an adapted e-beam lithography process. Finally, I will present a new concept of chiral fractal structures, created by introducing a rotation angle inside the fractal.

4.1 Introduction

As already shown, the surface plasmon resonance in metals, including aluminum, is very sensitive to the geometrical properties of the structure including particle dimensions, surface, volume and, most importantly, shape. This is why scientists from plasmonics developed new types of structures that were suitable for precise tasks, such as the "bow-tie" structure [Şendur and Challener, 2003] to generate intense hot-spots where light is confined, or matrices of rotated nanorods to create a metasurface working like a lens [Kildishev, Boltasheva, and Shalaev, 2013]. Creating an efficient form factor for emission enhancement of thin films is the purpose of this study.

The fractal-like shape is a common feature in natural and artificial objects (figure 4.1). A popular (and delicious) natural fractal is the Romanesco cauliflower (fig. 4.1a). Similarly, the common cauliflower is also fractal-like, however the structure is not as neat as the previous one. Most mobile phones use fractals for antennas (fig. 4.1b), a compact design that can be confined in a small volume and provide more space for other components. In the virtual world, fractals are even more popular, starting from screen wallpapers for computers to sophisticated algorithms – for example behind some of the cryptocurrencies lies a fractal system of transactions [Popov, 2017].

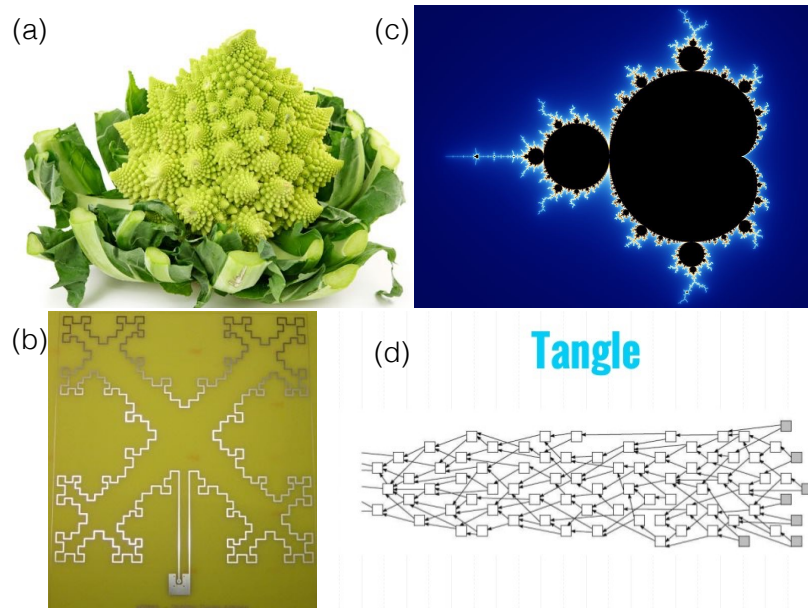


FIGURE 4.1: (a) Romanesco coliflower. Extracted from **Wikimedia** (b) Mobile phone antenna. Extracted from *Fractal antenna experiment*. (c) Graphic image of Mandelbrot fractal. Extracted from **Wikimedia** (d) IOTA Tangle. Extracted from Popov, 2017.

As it might be expected, fractals have attracted attention in nanoscience and especially in the field of plasmonics. There are many types of different fractals, opening a huge field for plasmonic engineering. Some of the fractal shapes are more popular in other sciences and mathematically described. For now, several noticeable works are published that have focused on studies of fractal-like films and clusters [Dong et al., 2014][Hou et al., 2014], the Sierpinski nanocarpets [Volpe, Volpe, and Quidant, 2011], the Vicsek fractal [Wen et al., 2002], and trapezoidal log-periodic geometries. [Aouani et al., 2013][Navarro-Cia and Maier, 2012].

4.1.1 Fractal structure

A fractal is a set of objects possessing a propriety of self-similarity. A first mathematical concept appeared in the XVII century using the term of recursion. However the first official mention of the name "fractal" is dated 1975, the year of the first edition of the book by Benoit Mandelbrot, 1983. Mandelbrot used fractal approximation to calculate the length of the Great Britain coast. Fractals can exist in whatever dimensional space and can have absolutely different representations, but some fractals can be visualized. For example, in figure 4.2 are presented several fractals.

Due to their structures, fractals can have dimensions that differs from the topological dimensions, (2D for surface or 3D for volume) and even with non-integer values. For example, fractal 4.2d can be characterized as a 4-dimensional (to account for the number of branches) lying within the 2 topological dimensions of a surface. That is why those kind of structures are so appealing for application in antennas. While keeping the same used volume or

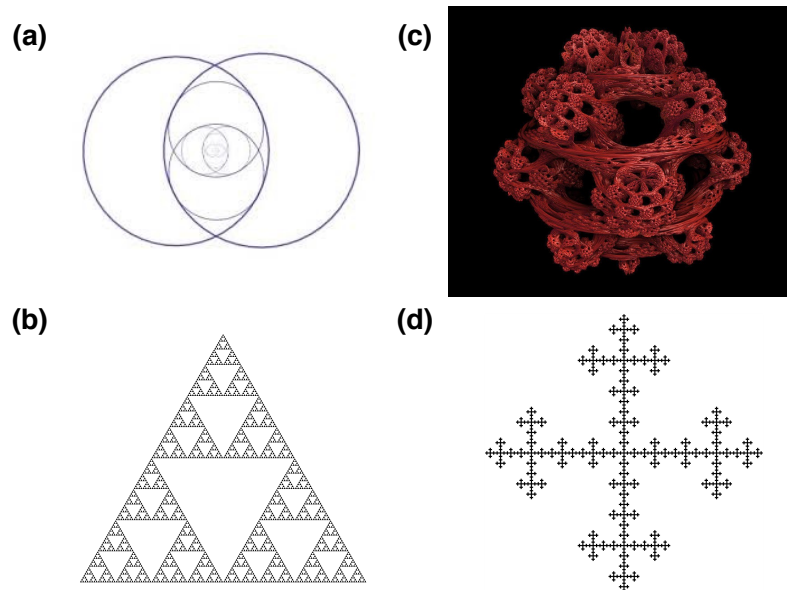


FIGURE 4.2: (a) 2D topological fractal build of circles. Extracted from **Wikimedia** (b) 2D topological Sierpinski fractal. Extracted from **Wikimedia** (c) 3D topological Mandelbulb fractal. Extracted from *Sub.Blue*; (d) 2D topological Vicsek fractal. Extracted from **Wikimedia**

surface, a fractal antenna can exhibit a higher efficiency via, for instance, an increased total antenna perimeter.

In mathematics and computer science, the term of a fractal is usually connected with the term of *graph* – a set of a "vertexes" and "edges". The fractal on the picture 4.2d is actually a graph. Graph theory is an important domain of mathematics describing those structures, their properties and structuring applications. Among those categories exists a subset called "trees" – a connected graph with no loops.

The Cayley graph is one of the most well-known mathematic fractal structures. It is a graph defined by the Cayley theorem [Cayley, 1878]. Let G be a group and S be a generating set. The Cayley graph $\Gamma = \Gamma(G, S)$ is a colored directed graph constructed as follows: (Cayley)

- Each element $g \in G$ is assigned a vertex: the vertex set $V(\Gamma)$ of Γ is identified with G .
- Each generator $s \in S$ is assigned a color c_s .
- For any $g \in G, s \in S$ the vertices corresponding to the elements g and $g * s$ are joined by a directed edge of color c_s . Thus the edge set $E(\Gamma)$ consists of pairs of the form $(g, g * s)$, with s and S providing the color.

In geometric group theory, the set S is usually assumed to be finite, symmetric (i.e. $S = S^{-1}$) and not containing the identity element of the group. In this case, the uncolored Cayley graph is an ordinary graph: its edges are not oriented and it does not contain loops (single-element cycles) and it is so called Cayley tree.

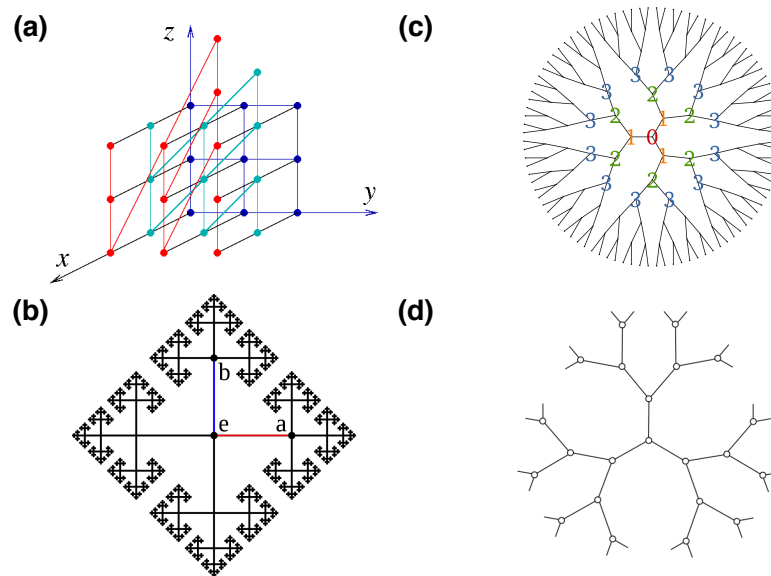


FIGURE 4.3: (a) Part of a Cayley graph of the Heisenberg group (The coloring is only for visual aid). Extracted from Ref [Wikimedia](#) (b) The Cayley graph of the free group on two generators a and b . Extracted from [Wikimedia](#) (c) Bethe lattice - a subclass of Cayley trees. Numbers represent generations. Extracted from [Wikimedia](#) (d) Finite Cayley tree. Extracted from Khorrami and Aghamohammadi, [2014](#).

In this work we have studied Cayley trees. Those graphs have a root or "generation zero" point. The number of branches from the root is called the *dimension* of the graph, and every next generation has a self-similarity to the previous one. For easier interpretation, at this stage we assume that every next generation is a copy of the previous one with a different length of the branch. Using this terminology, the graph in fig. 4.3b is 4 dimensional with 6 generations and the one in fig. 4.3d is 3 dimensional with 4 generations. Those fractals have a rotational symmetry.

4.1.2 State of the art

We already mentioned that fractals are well-known in radiowave technology. There also exist several attempts to adapt fractal antennas for to the visible and near-infrared range. The previously mentioned articles are mainly focused on studies of fractal films and clusters, as well as special types like the Sierpinski nanocarpets or the Vicsek fractal. In their work, S. Gottheim et al., [2015](#) published an investigation of one of the basic fractal structures, the Cayley tree. To be precise, it should be mentioned that some of the other fractals can be described as Cayley trees with a different set of generation rules. For instance, the Sierpinski carpet would be built from triangles instead of rods.

S. Gottheim and coworkers produced gold nanofractals with different sizes and geometries. Optical characterization was performed in the infrared spectra and compared with numerical simulations. The main results from this work are presented in figure 4.4. From

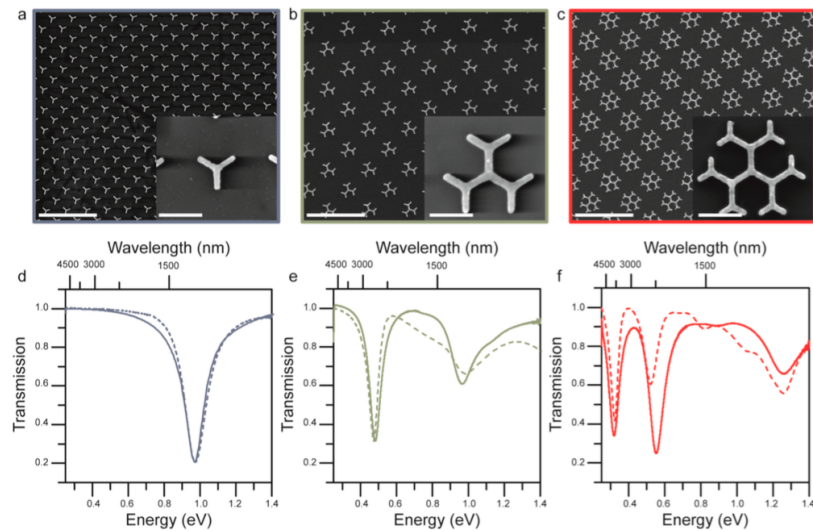


FIGURE 4.4: Scanning electron micrograph (SEM) images of $50 \times 50 \mu\text{m}$ 2D arrays of (a) first-, (b) second-, and (c) third-order Cayley trees with the individual structures shown as insets. The periodicity of the first-order Cayley tree (a) is 500 nm in both directions, while the (b) second- and (c) third-order Cayley trees have 1 μm periodicity. The array scale bars are 2 μm ; inset scale bars are 300 nm. (d-f) Experimental Fourier transform infrared transmission spectra (solid lines) of the first-, second-, and third-order Cayley tree structures under nonpolarized light excitation with corresponding finite element method simulated transmission spectra (dashed lines) reveal an increase in the number of resonances as the fractal geometry is iterated. Each newly emerging resonance occurs at an energy lower than those seen previously. Extracted from Gottheim et al., 2015.

their simulated electric field maps, they found that the plasmon excitation is mainly confined in the termination of the branches. From this the authors inferred that the charges concentrate on the tips and the degeneracy of this distribution creates several plasmonic modes within the multigeneration Cayley trees [Gottheim et al., 2015]. A schematic of the charge distribution is shown in figure 4.5. This yields a simple description of the existing plasmon modes in Cayley tree structures: fractals with one generation exhibit one main plasmonic resonance, with two generations, two peaks, and so on (see figure 4.4).

Another interesting concept for fractal plasmonics is the Sierpinsky carpet [Sierpinski, 1916]. This structure, generated on a base of triangles (figure 4.6a) combines properties of bow-tie structures with fractal effects. For example, the work of S. Cakmakyapan et al., 2014 presenting an excellent study of those structures.

The authors found that with the increase of the number of generations, i.e. smaller triangles combined together, only a slight redshift of plasmonic resonance was observed, as shown in figure 4.6b. In contrast, a striking difference in the spatial distribution of the electric field intensity is observed on the maps of the electric field intensity (fig. 4.6c) for the different generations. Thanks to the multiple hot spots, where the electric field is enhanced and localized, it is possible to apply such structures for nano- and micro-size antennas, and for SERS.

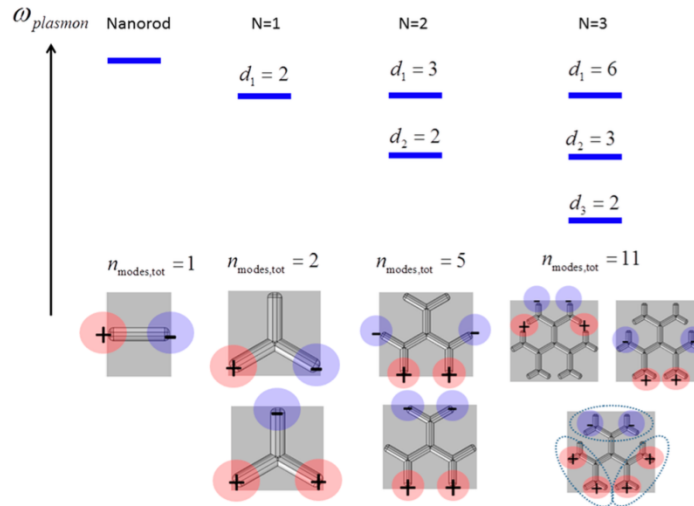


FIGURE 4.5: Schematic of formation of the multippeak plasmonic spectra. This principle to generate plasmonic modes is based on the assumption of changes located only on the tips. Mode 1 with the corresponding degeneracy d_1 (N) is the dipolar interarm oscillation of charge. Mode 2 is the interbranch oscillation. Mode 3 on the fractal $N = 3$ is more like a “global” plasmon. In this and other analogous more extended plasmon modes, the charge oscillates between the complex branches shown with dashed ovals (lower right corner of the figure). Extracted from Gottheim et al., 2015.

4.1.3 Surface enhancement

In the previous Chapter, we observed that the spatial extension of the enhanced electromagnetic field around the aluminium nanoparticles (the plasmonic modal volume) with respect to the volume of the epitaxial zinc oxide layer was not sufficient to obtain a significant enhancement of the emitted photoluminescence. As a consequence, it appears a question of how to maximize the effectiveness of a plasmonic structure that is confined within a surface. There are two approaches to solve this issue. The first one is to generate better “hot spots” exhibiting extremely high values of field enhancement using, for example, dimer structures such as bow-tie antennas. The problem is that these plasmonic hot spots are also extremely confined, therefore the plasmonic enhancement will only affect a small region of the active material. The second approach is to increase the area of enhancement.

As already known from the previous chapter, Purcell effect enhancement of photoluminescence is proportional to the local optical density of states, which is dependent from the electric field E . On the other hand nanoantenna effect is also dependent of local electric field enhancement.

The goal is to find an optimal shape of the particles to acquire a maximum of plasmon-enhanced photoluminescence. Assuming that penetration depth of the enhanced local electric field is the same, the total enhancement could be estimated by the average electric field (or square root of intensity $\sqrt{I_E}$) per unit surface.

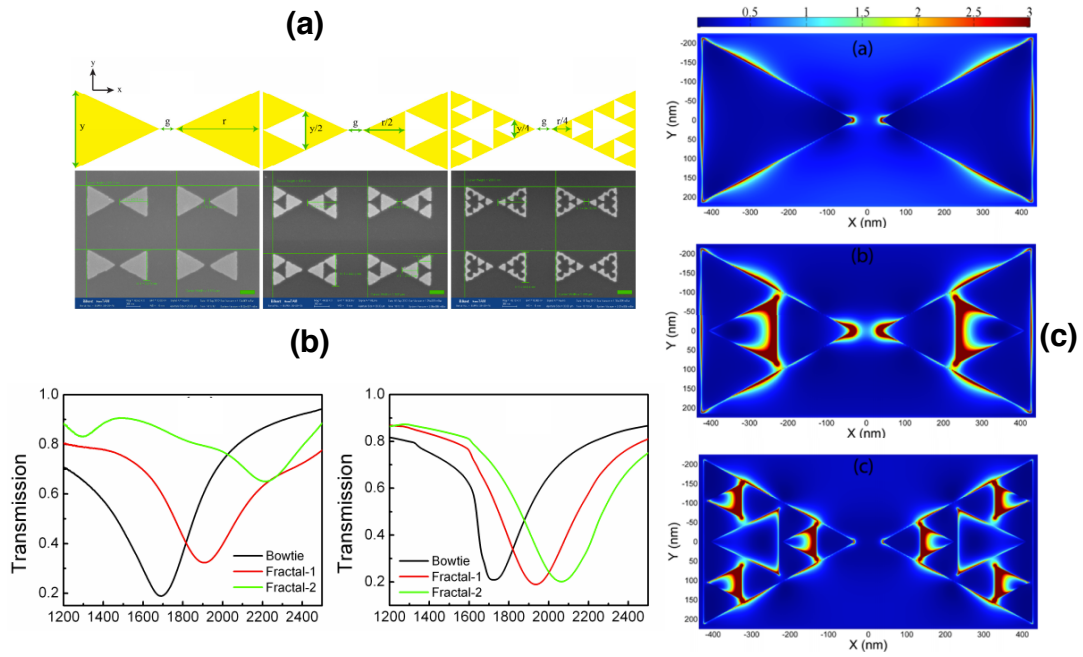


FIGURE 4.6: Schematics (above) and SEM (below) images of Bowtie, Fractal-1, and Fractal-2 structures. $g = 65$ nm, $r = 400$ nm, $y = 420$ nm. Scale bar is 100 nm; (b) Transmission spectra of the antenna arrays from experiment and simulations; (c) Electric field distributions at the Stokes shifted wavelength, 895 nm for Bowtie and two Fractals. The maximum of the color bar is set to the same value for comparison. Extracted from Cakmakyapan et al., 2014.

4.2 Figure of merit for evaluating fractal structures

Previously we found a figure of merit in the electric field. This will be our base point for the optimization and design of the fractal structures, and their further fabrication process. To decrease the fabrication time while increasing the studied range of parameters, we performed preliminary simulations using FDTD. The chosen patterns were subsequently fabricated by electron beam lithography.

4.2.1 FDTD simulations

FDTD simulations of different structures were performed. The FDTD model used for this study consist of that following: aluminum particles are placed onto a quartz substrate, illumination source (TFSF) is placed in the air and the square field monitor (580×580 nm²) is situated 2 nm under the interface in a substrate. An uniform mesh is placed around particle and monitor in order to obtain a uniform matrix of field intensity. All boundary conditions were set to perfect matched layers (PML) in order to measure single particle response without the inference of collective resonances such as lattice modes. The monitor is fitted with an additional script calculating the average electric field over all cells as a square root of intensity. In this case the uniformity of the mesh is important, in order to have the same

weight for all calculated cells. Particles are made from aluminum of 50 nm height and with 3 nm layer oxide at the all interfaces with air. Data for materials are taken from Palik, 1997.

In order to have a reference and to quantify the advantage brought by the fractal geometry, we are using cylinder particles and an empty substrate. This yields the following list of geometries to optimize:

- Cylinder particle;
- Optimized square array of nine cylinders, close by the quantity of aluminum;
- Cayley tree;
- Pristine substrate.

All optimization algorithms were made for the precise wavelengths of 325 nm (excitation wavelength of ZnO), 380 nm (the emission wavelength of ZnO or quantum dots) and 530 nm (a common excitation wavelength in visible), which all have interest for applications with aluminum. To ensure that all fractals work at the best conditions, an optimization script was used with variation of every dimension in XY plane, i.e. radius for cylinders, length and width for fractals. Results of those simulations are presented in the following table. Difference in "a" and "b" is polarization: "a" goes for polarization along one of the branches, "b" along another symmetry axis (red arrow shows polarization on schematics).

Results of FDTD simulations are shown in table 4.1 and pictures - optimized structures showing the highest E_{av} at the reference wavelengths. Let us underline that we also performed tests for 4D3G and higher order fractals, but we observed no significant increase in the average field in comparison with the increased complexity of fabrication. Big cylinder is a cylinder with approximately same quantity of aluminum as the fractals. Optimized cylinder is one that giving maximum value of E_{av} .

We assume that our optimization script also investigates the case of dimers, because of the wide range of allowed period in the case of an array. The results confirm that generating hotspots with high values of local field enhancement yields a loss in terms of area coverage. As we can see from the table, fractals provide an average field at the same level as an optimized array of cylinders, which is obviously based on the lattice modes described in Chapter 2. However, fractals could also be enhanced by lattice modes, since Rayleigh anomalies do not depend on the geometry of particles but only on the array parameters. For the case of a single cylinder, the fractal structure transcends it completely.

Normalized electric field intensity maps for the most efficient fractals are presented in figure 4.7. Those positions do not always correspond to the resonance position, which generally yields the excitation of hot spots at the edges. As it can be seen, the field intensity is rather distributed along the fractal, providing a good areal coverage.

The next step is to fabricate real Cayley trees in aluminum. Because of the complexity, small feature size and high material density of those structures the standard lithography process should be optimized to achieve a satisfactory result.

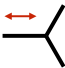
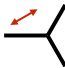


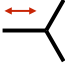
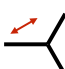
Structure/Wavelength	325 nm	380 nm	530 nm
3D2G-a 	$l_1 = 120$ nm $l_2 = 120$ nm $w = 60$ nm $E_{av} = 1.49$	$l_1 = 120$ nm $l_2 = 60$ nm $w = 60$ nm $E_{av} = 1.17$	$l_1 = 120$ nm $l_2 = 60$ nm $w = 31$ nm $E_{av} = 1.24$
3D2G-b 	$l_1 = 120$ nm $l_2 = 120$ nm $w = 60$ nm $E_{av} = 1.49$	$l_1 = 120$ nm $l_2 = 120$ nm $w = 60$ nm $E_{av} = 1.15$	$l_1 = 120$ nm $l_2 = 60$ nm $w = 31$ nm $E_{av} = 1.24$
4D2G-a 	$l_1 = 150$ nm $l_2 = 120$ nm $w = 49$ nm $E_{av} = 1.56$	$l_1 = 120$ nm $l_2 = 60$ nm $w = 60$ nm $E_{av} = 1.16$	$l_1 = 120$ nm $l_2 = 60$ nm $w = 32$ nm $E_{av} = 1.37$
4D2G-b 	$l_1 = 150$ nm $l_2 = 120$ nm $w = 49$ nm $E_{av} = 1.56$	$l_1 = 120$ nm $l_2 = 60$ nm $w = 53$ nm $E_{av} = 1.15$	$l_1 = 120$ nm $l_2 = 60$ nm $w = 32$ nm $E_{av} = 1.37$
3D3G-a 	$l_1 = 100$ nm $l_2 = 100$ nm $l_3 = 100$ nm $w = 60$ nm $E_{av} = 1.49$	$l_1 = 60$ nm $l_2 = 100$ nm $l_3 = 50$ nm $w = 56$ nm $E_{av} = 1.28$	$l_1 = 100$ nm $l_2 = 100$ nm $l_3 = 56$ nm $w = 30$ nm $E_{av} = 1.29$
3D3G-b 	$l_1 = 100$ nm $l_2 = 100$ nm $l_3 = 100$ nm $w = 60$ nm $E_{av} = 1.48$	$l_1 = 61$ nm $l_2 = 100$ nm $l_3 = 500$ nm $w = 35$ nm $E_{av} = 1.31$	$l_1 = 95$ nm $l_2 = 69$ nm $l_3 = 58$ nm $w = 49$ nm $E_{av} = 1.24$
Big cylinder	$r = 120$ nm $E_{av} = 0.79$	$r = 120$ nm $E_{av} = 0.8$	$r = 120$ nm $E_{av} = 0.86$
Optimized cylinder	$r = 30$ nm $E_{av} = 0.9$	$r = 38$ nm $E_{av} = 0.92$	$r = 62$ nm $E_{av} = 1$
Array	$r = 30$ nm $D = 250$ nm $E_{av} = 1.54$	$r = 40$ nm $D = 400$ nm $E_{av} = 1.62$	$r = 51$ nm $D = 300$ nm $E_{av} = 1.38$
Empty	$E_{av} = 0.78$	$E_{av} = 0.79$	$E_{av} = 0.80$

TABLE 4.1: Results of optimization via Lumerical FDTD solutions. Listed structures provide maximum E_{av} at certain wavelength.

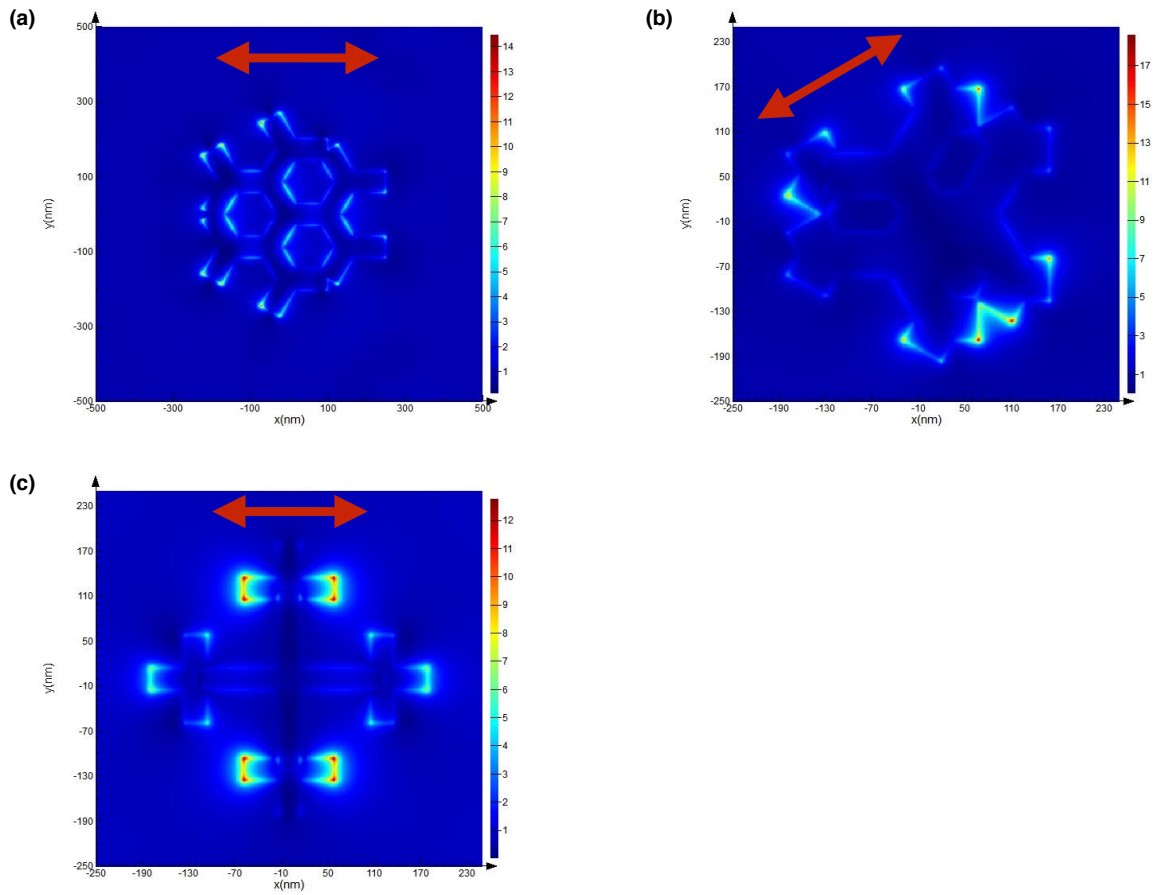


FIGURE 4.7: Normalized electric field intensity maps $|E/E_0|^2$ for some positions from the table: (a)3D3G-a at $\lambda = 325$ nm; (b)3D3G-b at $\lambda = 380$ nm; (c) 4D2G-a at $\lambda = 530$ nm.

4.2.2 Sample production

The Cayley tree structure is a complex geometry figure and more advanced nanofabrication methods are needed. First of all, we used another e-beam microscope (Raith e-Line e-beam microscope) instead of Hitachi NPGS module for the e-beam writing. It is a recent e-beam lithography setup providing a high precision for large scale patterns. Thanks to the import feature of mask models fractals were easily generated outside of the setup with different parameters. Moreover it allowed the creation of random patterns, the advantages and disadvantages of which will be discussed later.

First attempts were performed with almost the same conditions as for samples from the previous chapters. The quartz substrate (cover slip Agar scientific 200 μm thick) was covered with PMMA dissolved in MIBK with concentration 30g/L, spin-coated at 4000 rpm and baked on a 170°C hot plate for 12 minutes. To avoid charging effect, a thin layer of conductive polymer (Espacer 300Z) was deposited on the top of PMMA. Variation of dose was performed from 250 to 600 $\mu\text{C}/\text{cm}^2$. After lithography and development of PMMA, a 50 nm layer of aluminum was evaporated followed by lift off process in acetone.

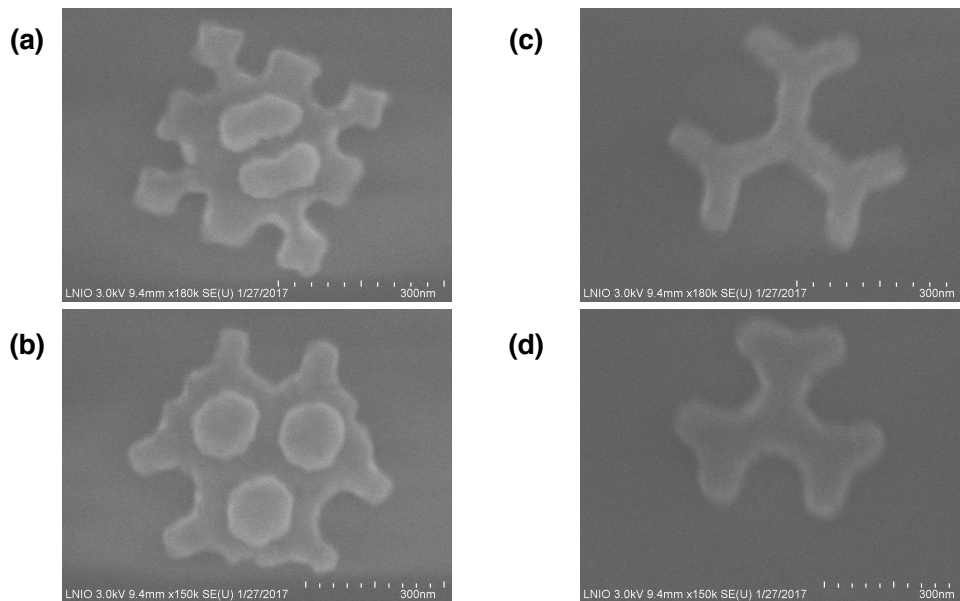


FIGURE 4.8: First unsuccessful fabricated sample.

Figure 4.8 represents our first attempt to produce the graph structure. The samples with a lower dose contained 90% of non-imprinted structures due to insufficient exposure. On the other hand, structures with higher doses are over-imprinted. Those results show that the acceptable dose window is lying between 350 and 400 $\mu\text{C}/\text{cm}^2$, and is less than 50 $\mu\text{C}/\text{cm}^2$ wide. Such a small window of acceptance leads to an increased difficulty to get reproducible results due to the unavoidable procedure fluctuations, such as PMMA and conductive polymer thickness, evaporated metal roughness and others.

The use of a 50-nm-thick aluminum layer allows for a decrease of the necessary thickness of the PMMA layer. This leads to an enhanced contrast for lithography. Higher contrast allows lower writing doses to be used and increases the size of the sensitivity window. To achieve the desirable 100 nm thickness of polymer, the concentration of PMMA solution was decreased first to 15 g/L with 2500 or 2000 rpm speed for spin-coating. However, the decrease of the rotation speed creates an uneven polymer film thickness that critically affects reproducibility. To prevent this problem, a 20 g/L solution was prepared and spin-coated at the speed 4000 rpm. The baking time on the hot plate was increased up to 17 min to create a more solid polymer film. Thanks to these improvements, and after several iterations, the quality of the fabricated structures was significantly ameliorated. In figure 4.9, a successful sample is presented.

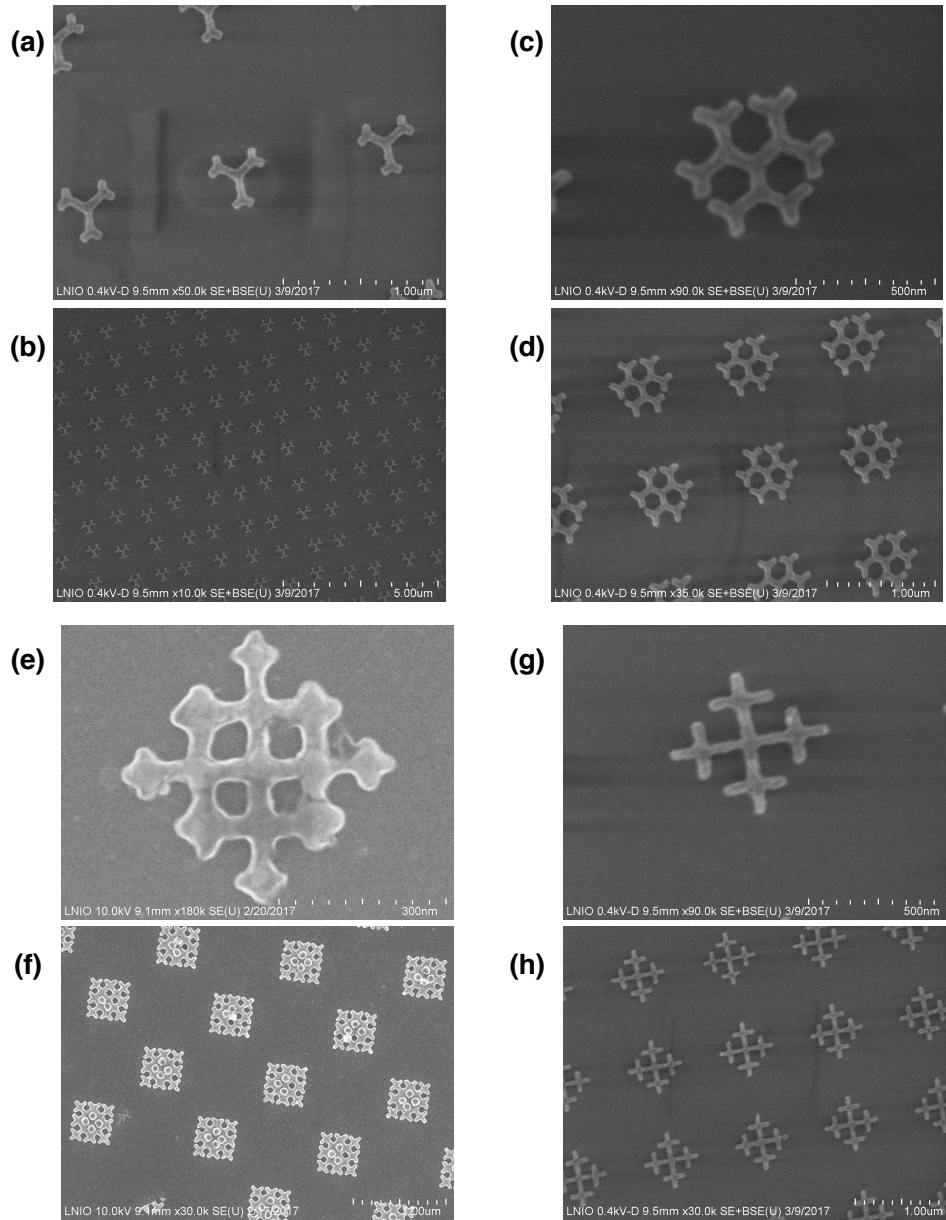


FIGURE 4.9: SEM images of fabricated aluminum nanofractals. (a,b) 3D2G; (c,d) 3D3G; (e,f) 4D3G; (g,h) 4D2G.

Imprinting fractals with more than two generations, three for example in figure 4.9e,f, appeared to be a complicated task due to the non-uniform dose distribution. This non-uniformity appears due to the large size of the structure and proximity effect, i.e. influence of electron-substrate and electron-polymer interactions, when the exposure dose distribution is wider than the scanning pattern. In this case with increasing center to border distance dose falls and it leads to the rounded corners of the last generation. To avoid overlapping of branches, 3rd generation have a small length, less than 70 nm. With the width of 50 nm, the rounded corners of a rectangle became a small circle head. As a solution another resist could be used for fabrication.

Aluminum oxidizes quickly in air. A 3-nm-thick native oxide layer appears almost immediately around the particle and then it stabilizes in time, with a thickness increase of 1-3 nm per month under normal conditions. In the case of Cayley tree structures or other fractal structures, the surface to volume ratio is increased. As a consequence, the role played by oxidation is even more critical in the formation of plasmonic resonance and their stability. Therefore, optical measurements were performed as fast as possible just after the fabrication.

4.2.3 Optical measurements

As clearly explained in the work of Gottheim et al., 2015, plasmonic resonances for fractals result from the charge distribution on the edges of the last generations. In the article, well-defined resonances were observed on the extinction spectra, thanks to the use of rather large gold structures and low losses in gold. For aluminum Cayley trees, the resonant wavelengths are expected to be closer to each other and to partially overlap due to the lower quality factor. Through FDTD simulations, the parameters of aluminum fractals were optimized for different wavelengths (325 nm, 380 nm and 530 nm).

60x60 μm patterns were produced. As the size of the probing spot is around 30 μm in diameter on our optical setup, this allows representative spectra to be obtained even in presence of small fabrication defects. Patterns were realized in two forms: square lattices and pseudo-random distribution. The lattices have orthogonal base vectors with the same length of 1 μm . The expected position of the first orders of Rayleigh anomaly are located in the infrared part of the spectra and the influence of higher order can be neglected in the range of interest. But to avoid any diffraction effects, even if influence of high orders of Rayleigh anomalies is weak, we created a pseudo-random pattern. Every particle has "nest" coordinates, which are placed the same way as in lattice model – 1 μm square lattice. But also every fractal has a displacement vector with a random length in the range 0 to 0.2 μm in a random direction. This destroys collective resonances that might appear in a periodic structure. But in contrast to a completely random displacement, the pseudo-random method helps to keep neighboring structures away from overlapping by keeping the center-to-center distance not smaller than 0.6 μm .

Studied sample contains fractals, theoretically optimized for 325 nm (see Table 4.1), with different configurations. The height was kept at the same value of 50 nm.

1. 3 Dimensions and 2 Generations with lengths: $l_1 = 120 \text{ nm}$, $l_2 = 120 \text{ nm}$, $w = 60$ (3D2G);
2. 3 Dimensions and 3 Generations with lengths: $l_1 = 100 \text{ nm}$, $l_2 = 100 \text{ nm}$, $l_3 = 100 \text{ nm}$, $w = 60$ (3D3G);
3. 4 Dimensions and 2 Generations with lengths: $l_1 = 150 \text{ nm}$, $l_2 = 120 \text{ nm}$, $w = 49$ (4D2G);
4. 4 Dimensions and 3 Generations with lengths: $l_1 = 95 \text{ nm}$, $l_2 = 86 \text{ nm}$, $l_3 = 92 \text{ nm}$, $w = 31$ (4D3G);

Creating fractal particles with electron beam lithography with more than three generations as well as with more than four dimensions becomes a complicated task due to the small distances between branches. As explained above, FDTD simulations showed there was almost no interest in those structures in comparison with 3D and 4D. Already the last one, 4D3G fractals, pattern was unsuccessful.

Optical measurements were performed within the UV-range using homemade microscope setup at normal incidence without light polarization. A schematic representation is shown in figure 4.10.

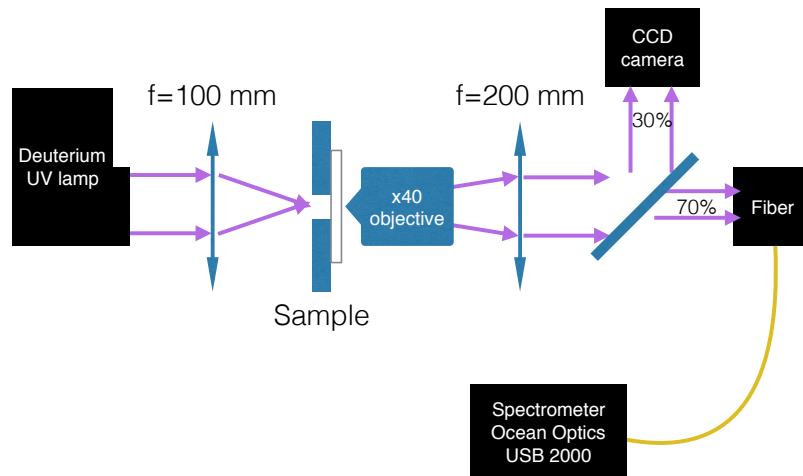


FIGURE 4.10: A schematic representation of the homemade UV microscope setup. Deuterium lamp is used as a light source. Probing spot size is defined by fiber diameter.

Absorbance spectra are obtained from transmission data by the formula:

$$A = -\log \frac{I}{I_0} \quad (4.1)$$

where I_0 is the incoming light intensity and I is the transmitted one.

Resulting spectra shows a small intensity resonance due to the large center-to-center (or average center-to-center for random pattern) distance between structures. In comparison with the cylinder arrays from Chapter 3, the quantity of aluminum per unit area is decreased almost twice. This dramatically decreases the signal to noise ratio. Because of this issue, we had to introduce a "boxcar" in the spectrometer settings to sum the detected intensity between neighbouring pixels of the CCD array detector. This explains the "step-like" appearance of some spectra in the following figures. In figures 4.11, 4.13 and 4.14 you can see comparison experimental data and FDTD data. The simulations have been carried out using a geometrical model close to the measured size and form of the fractals.

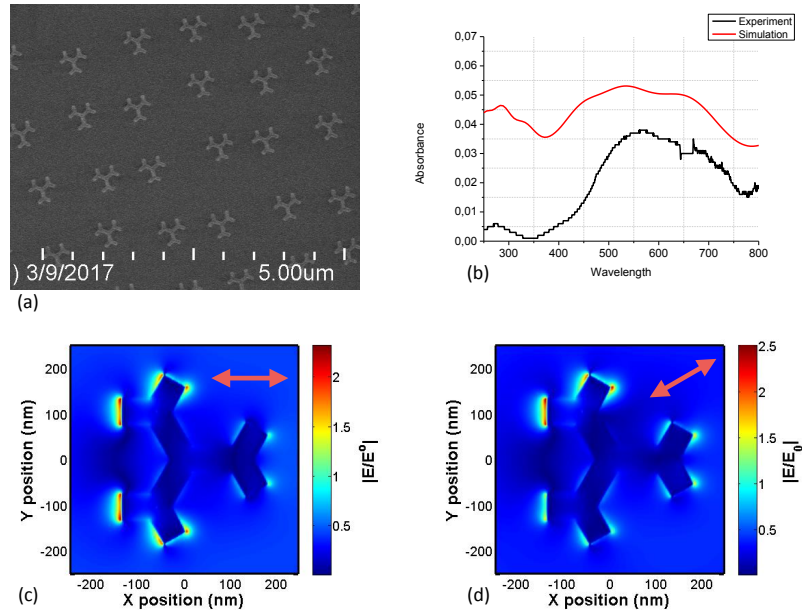


FIGURE 4.11: (a) SEM image of 3D2G fractal. (b) Absorbance spectrum of showed particles and simulated absorbance spectrum for comparison. Simulations performed for the real size of the structures measured with SEM: $l_1 = 120$ nm, $l_2 = 90$ nm, $w = 60$. (c,d) Field map generated with FDTD simulations for the peak wavelength with two polarization along symmetry axis at $\lambda = 530$ nm.

Experimental results for structures 3D2G are in good agreement with the FDTD simulations as can be seen in Fig. 4.11. As predicted we observed low quality factor $Q \approx 3$, coming from not well-resolved resonances. Also in figure 4.11 UV peaks around wavelength of 250 nm can be seen. The origin of it lies in mainly in dipolar resonance within one branch as can be seen in figure .

Four dimensional Cayley trees have a different symmetry. Presented in figure 4.14c field profile showing that electric field is less localized in those configurations, probably because of the smaller distance between branches of the graph. But again in case of larger density of small elements producing of it obstructed. Those pattern as well have a good correspondence with FDTD simulation results.

4.2.4 Hot cells

The Cayley tree structures described in this chapter sometimes contain parts looking like "not complete" geometrical figures, or geometrical figures with a gap left. There are squares and hexagons as shown in figure 4.15. Those can be called "split figures" in analogy with the so-called split rings. Under certain conditions, these split figures are able to generate very interesting field profiles sensitive to the incident light parameters.

The studied Cayley trees always have one or two different types of symmetry axis in the fractal plane: one among one the branches for odd number of dimensions and one between two branches for even number of dimensions. If the polarization axis is aligned with the incident light among the second symmetry axis for 4D fractal it will cross two opposite

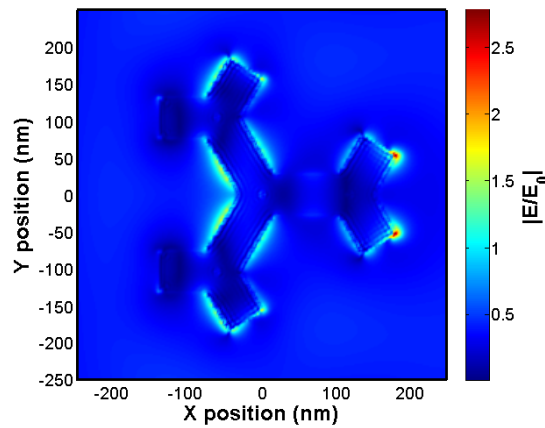


FIGURE 4.12: Normalized electric field profile for 3D2G fractal $l_1 = 120$ nm, $l_2 = 90$ nm, $w = 60$ at $\lambda = 267$ nm.

splits. This configuration leads to the electric field profile confined within a split figure, in this case a square. In figure 4.16 is represented electric field intensity profile for two orthogonal polarizations. The operating wavelength is not at resonance of the whole fractal. Only split squares, or "cells" 2 and 3 in one case and 1 and 4 in opposite are involved. By switching polarization between 45° and -45° it is possible to choose which cells are activated.

Presented images in figure 4.16 are results of FDTD simulations for 4D2G structure with $l_1 = 120$ nm and $l_2 = 80$ nm with obtained field profile at 380 nm wavelength. Two orthogonal polarized light were applied in case 4.16a and 4.16b as shown by red arrows in the figure. The maximum intensity of the electrical field is 7 and the average field intensity inside the cell is ≈ 2 .

To sum up, we are capable to switch on and off a "nano-pixel" inside the fractal structure, using a simple remote optical command (the polarization state of the exciting light). Possible applications of this system are polarization sensitive detectors or emitters. In order to experimentally validate this finding, several methods are possible. The most simple among them are:

1. Scanning near field microscopy can be used to probe local modes under polarized illumination. The drawback of this method lies in the presence of the scanning probe, that might disturb the electromagnetic distribution.
2. Sensitive polymer described in works of R. Bachelot [Bachelot and Plain, 2013]. Under illumination, molecular nanomotors, based on azobenzene derivatives grafted to a polymer chain, can induce a mass migration [Hubert et al., 2008]. This movement can be detected with atomic force microscope (AFM), yielding a map of the exciting light intensity. The open question is if the predicted field intensity enhancement inside the cell will be sufficient to trigger the mass migration.

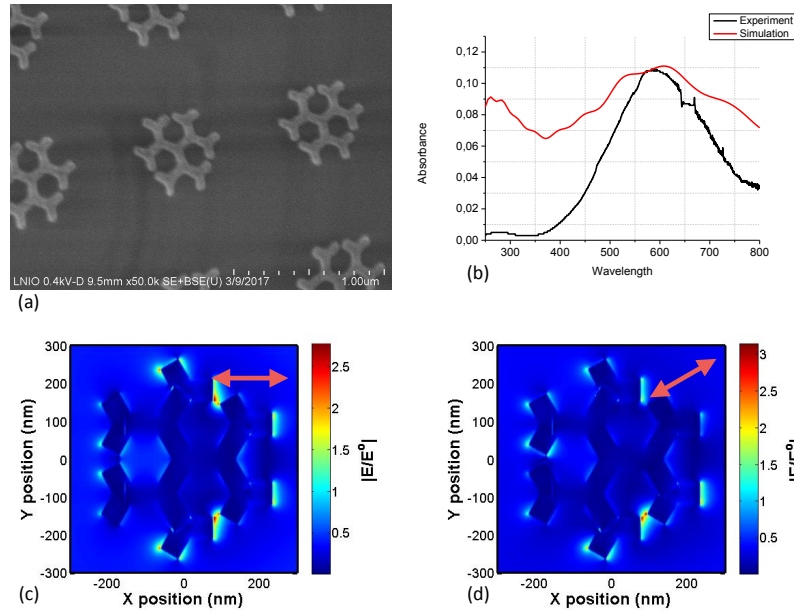


FIGURE 4.13: (a) SEM image of 3D3G fractal. (b) Absorbance spectrum of showed particles and simulated absorbance spectrum for comparison under non polarized illumination. Simulations performed for the real size of the structures measured with SEM: $l_1 = 105$ nm, $l_2 = 100$ nm, $l_3 = 80$ nm, $w = 60$.(c,d) Field map generated with FDTD simulations for the peak wavelength with two polarization along symmetry axis at $\lambda = 547$ nm.

4.2.5 Conclusion

In this section an investigation of the concept of fractal plasmonic structure was performed. After a study of existing experience in optics and also radio technology a Cayley tree geometry was chosen for further work. By the FDTD simulations the most efficient fractal structures were determined, using an average electric field per unit surface as a figure of merit.

The process of fabrication for producing complex fractal structures with relatively small size using e-beam lithography was improved. Even after this procedure of fabrication is not ideal and has poor reproducibility. Simple optical measurements performed with fabricated structures and they show a good correspondence with FDTD simulations.

However, experiments with optically active material were not performed. In this case there is a perspective work to prove effectiveness of fractal structures for coupling with light emitters.

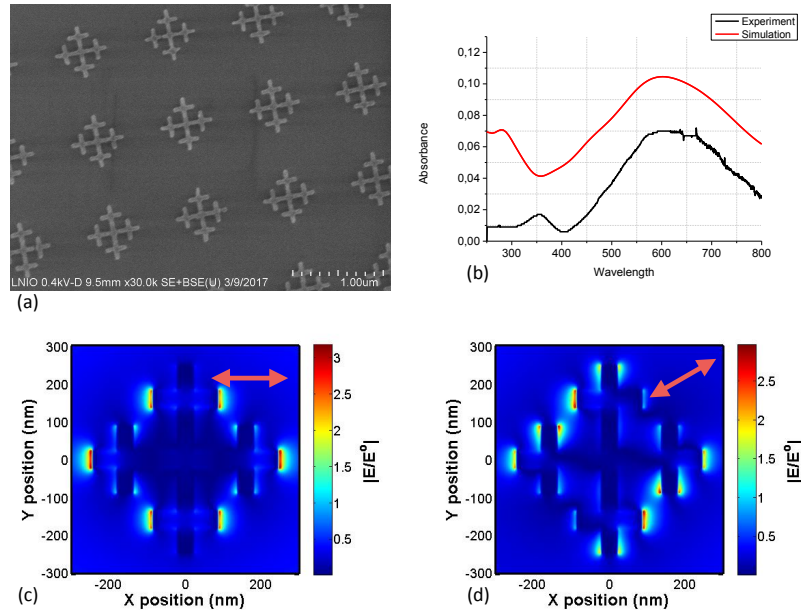


FIGURE 4.14: (a) SEM image of 4D2G fractal. (b) Absorbance spectrum of showed particles and simulated absorbance spectrum for comparison. Simulations performed for the real size of the structures measured with SEM: $l_1 = 160$ nm, $l_2 = 90$ nm, $w = 50$. (c,d) Field map generated with FDTD simulations for the peak wavelength with two polarization along symmetry axis at $\lambda = 626$ nm.

4.3 Chiral plasmonics with fractal structures

In the previous section, we discussed a pseudo-random pattern as a solution against Rayleigh anomalies. In addition, we discussed the idea of randomly orientate the fractals in the pattern. Through this, the idea to rotate the branches appeared.

Fractals exhibit a huge variety of forms and sizes. Chiral plasmonic structures previously reported in the literature, such as spirals or gammadions, can also be described as fractals. In this section will be discussed possible application of aluminum Cayley trees to the field of chiral plasmonics.

4.3.1 Chirality

The first definition of chirality was proposed by Lord Kelvin in 1893: *"I call any geometrical figure, or group of points, 'chiral', and say that it has chirality if its image in a plane mirror, ideally realized, cannot be brought to coincide with itself"* [Kelvin, 1894]. Chirality is a wide spread characteristic over different aspects of the natural world. Usually, chirality is connected with organic objects: chirality of carbon structures and chirality of organic molecules. Optical measurements based on circularly polarized light is a common technique of measurements for chiral structures. Symmetry of the light-matter interactions dictates the rules for optical chiral properties of molecules, structures and other things: circularly polarized light scatters in-equivalently with different orientations. An example of technique based on this phenomena is chiral rotational spectroscopy [Cameron, Götte, and Barnett, 2016] of molecules. It is

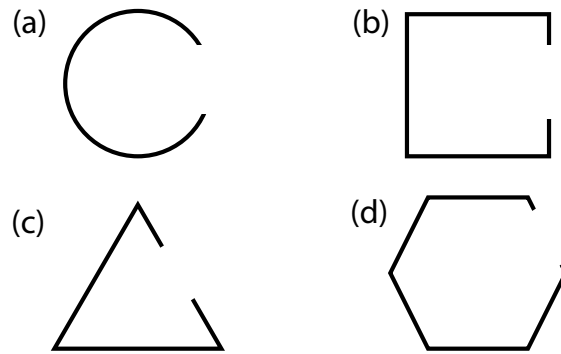


FIGURE 4.15: (a) Split ring, (b) Split square, (c) Split triangle, (d) split hexagon.

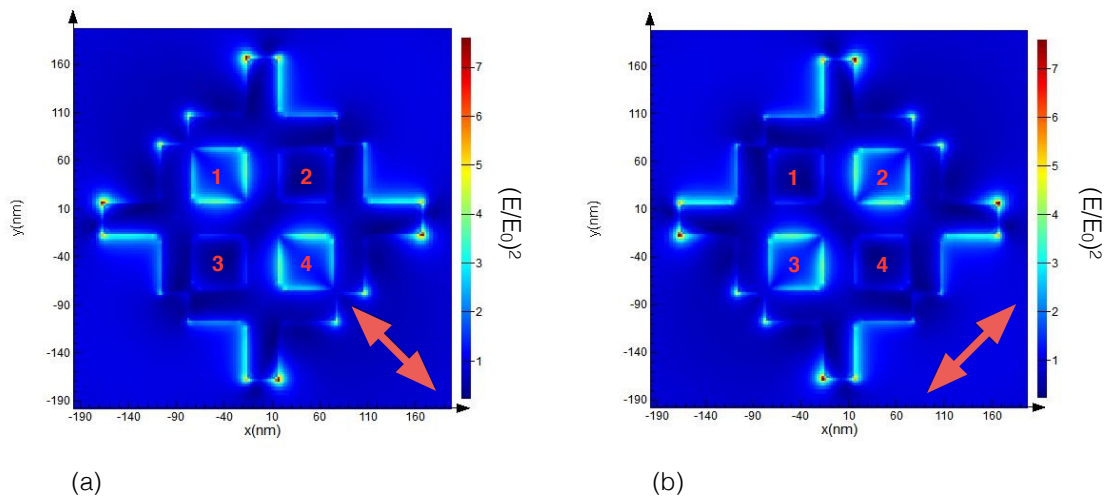


FIGURE 4.16: Field map of a fractal structure with orthogonal polarization at 380 nm illumination (left) Cells 1 and 4 are "hot" (right) Cells 2 and 3 are "hot"

a powerful recognition tool because many molecules have an unique chirality and can be distinguished through those experiments. A well-known example of chiral molecules are sugars: sucrose, dextrose, glucose and others – all of them have different chirality that can be determined using simple optical measurements.

But chiral structures can be made out of any material, because it is a pure geometrical property, and then it can be combined with other optical effects. In recent years, chiral plasmonic nanostructures have gained substantial interest [Schäferling et al., 2012][Mastroianni, C., and Paul Alivisatos, 2009][Fan and Govorov, 2010][Guerrero-Martínez et al., 2011]. Chiral plasmonic structures can have a large variation of the forms and obtain chiral sensitivity as high as molecules. By virtue of recent fabrication techniques like electron beam lithography new complex chiral structures can be produced. Also it is possible to produce not only planar but layered and even 3D structures like examples in figure 4.17. On the other hand

plasmonics provided confined and highly enhanced electromagnetic fields. In combination with the chiral form can provide local chiral effects around the nanostructures.

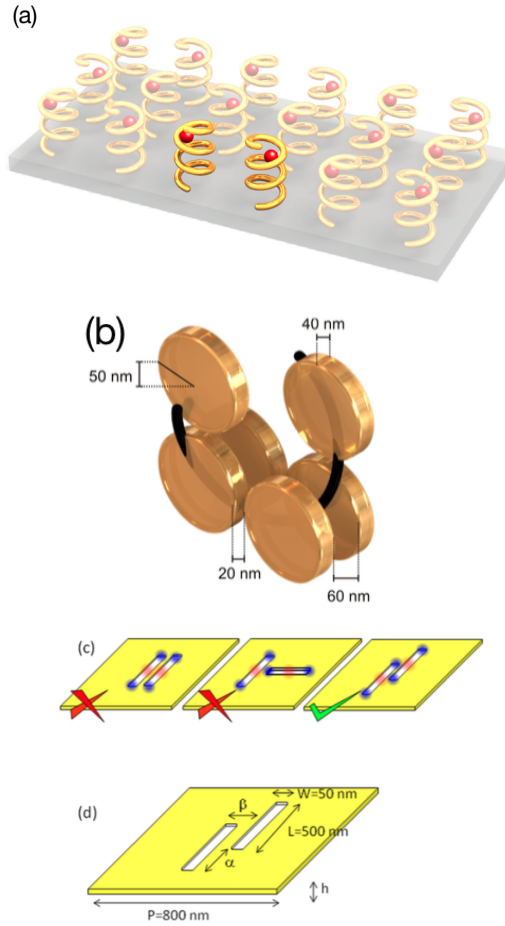


FIGURE 4.17: (a) 3D chiral structure. Extracted from Schäferling et al., 2012; (b) Layered chiral structure; (c-d) Pairing arrangements of nanoslits. Only the arrangement on the right will exhibit chiral electromagnetic eigenmodes. Extracted from Hendry et al., 2012.

To quantify chiral properties, several methods and characterizing metrics exist. The most common value is the *circular dichroism* CD . It is a macroscopic (far-field) characteristic defined by the difference in absorbance for right- and left-handed circular polarization of incident light:

$$CD = \Delta A = A_{LHP} - A_{RHP} \quad (4.2)$$

A normalized value is also used:

$$CD_N = \frac{A_{LHP} - A_{RHP}}{A_{LHP} + A_{RHP}} \quad (4.3)$$

Sometimes a circular dichroism measured in degrees can be found in the literature [Greenfield, 2006]. This value in degrees is called ellipticity θ and comes from light ellipticity of light:

$$\tan\theta = \frac{E_{RHP} - E_{LHP}}{E_{RHP} + E_{LHP}} \quad (4.4)$$

where E_{RHP} and E_{LHP} are the magnitudes of the electric field vectors of the right-circularly and left-circularly polarized light, respectively. Electric field magnitudes can be changed to the square root of intensity I :

$$\tan\theta = \frac{I_{RHP}^{1/2} - I_{LHP}^{1/2}}{I_{RHP}^{1/2} + I_{LHP}^{1/2}} \quad (4.5)$$

Dichroism is a small effect in magnitude, so it is possible to use some mathematical approximations and with Beer's law ellipticity can be written as:

$$\theta^\circ = \Delta A \left(\frac{\ln 10}{4} \right) \left(\frac{180}{\pi} \right) \approx 32.982 CD \quad (4.6)$$

So it means that value in degrees is linearly connected with circular dichroism value mentioned before.

As explained above, circular dichroism is a macroscopic quantity obtained from far-field measurements. To quantify the chirality inside nanostructures, a near-field quantity accounting for local chirality effects is required. Such a quantity has been defined quite recently and be called the *Optical Chirality* (or optical chirality density). It represents local enhancement effects appearing in plasmonic nanostructures and can be used to enhance the signal for detection of chiral molecules [Govorov et al., 2011]. Optical chirality can be written in the following form:

$$C(\vec{r}) = \frac{1}{2} [\epsilon_0 \vec{E}(\vec{r}) \cdot \vec{\nabla} \times \vec{E}(\vec{r}) + \frac{1}{\mu_0} \vec{B}(\vec{r}) \cdot \vec{\nabla} \times \vec{B}(\vec{r})] \quad (4.7)$$

where \vec{E} and \vec{B} are electric and magnetic fields, respectively. In the case of time-harmonic monochromatic fields, a simpler version can be written [Tang and Cohen, 2010]:

$$C(\vec{r}) = -\frac{\epsilon_0 \omega}{2} \text{Im}[\vec{E}^*(\vec{r}) \cdot \vec{B}(\vec{r})] \quad (4.8)$$

where \vec{E} and \vec{B} are the complex field amplitudes. In order to obtain more practical numbers, it is convenient to normalize this value using the chirality of a circularly polarized wave as a reference. This defines the *Optical Chirality Enhancement*, which is represented by the formula:

$$\hat{C}(\vec{r}) = \frac{C^\pm}{|C_{CPL}^\pm|} \quad (4.9)$$

where \pm goes for Right- and Left-handed polarizations and C_{CPL}^\pm goes for chirality without nanostructure. For unpolarized light \hat{C} is equal 0 and for circularly polarized light $\hat{C} = 1$. Fields with $\hat{C} > 1$ are called "super-chiral fields". These super-chiral fields stem for local effects, and as a consequence are confined to the near-field. Near chiral nanostructures, such as the one shown in figure 4.18 taken from [Schäferling et al., 2012], the optical chiral

enhancement can reach values around 10 for 2D chiral nanostructures, and even higher values (around 100) for 3D plasmonic chiral particles, such as an helix.

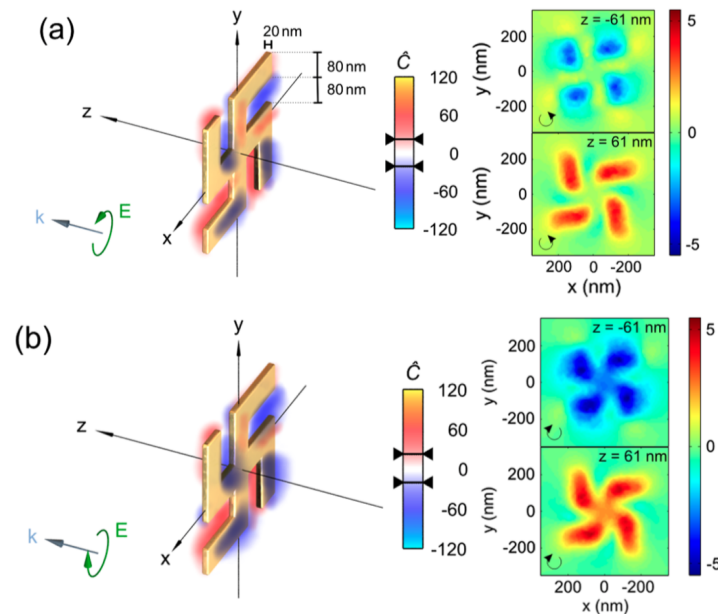


FIGURE 4.18: Optical chirality enhancement by a planar gammadion structure illuminated with (a) LCP and (b) RCP computed at a wavelength of $2.01\mu\text{m}$. The structure exhibits similar shapes for the regions with enhanced chirality for both polarizations; only the values differ (as best seen in the two-dimensional slice views). Extracted from Schäferling et al., 2012.

Most of the works mentioned above are oriented toward the visible and infrared parts of the spectrum, due to material and size limitations. As aluminum fractal nanostructures have proven their potential for UV and blue plasmonics, in the following we are going to explore the opportunity to extend optical chiral enhancement toward the blue region.

4.3.2 FDTD simulations

Preliminary studies were performed by FDTD simulations using the Lumerical FDTD software. This software allow the simulation of a circular polarization by using two orthogonal linearly-polarized light sources with a 90° phase difference. Through this method right-handed (RH) and left-handed (LH) polarizations were obtained.

Studied aluminum particles were placed onto an interface between air and a SiO_2 substrate. Concerning the boundary conditions, both Periodic and Perfect matched layer (PML) boundary conditions were used. Illumination comes at normal incidence from the air side. Monitors were placed under the particle in glass 2 nm below for near field monitor and 400 nm below for transmission monitor.

The Cayley tree structures described in the previous section are non-chiral structures because their mirrored image can be superimposed to the original. To check that and to validate our numerical model, two simulations were performed with RH and LH polarizations.

For this simulation Periodic boundary conditions were chosen for X and Y directions. Z direction (light propagation) was set PML. In figure 4.19 are plotted the absorption spectra for both polarization, and the difference between them – i.e. the circular dichroism as defined above. And as expected for a non-chiral structure, there is no difference between the RH and LH absorption spectra and the CD is equal to zero for all wavelengths.

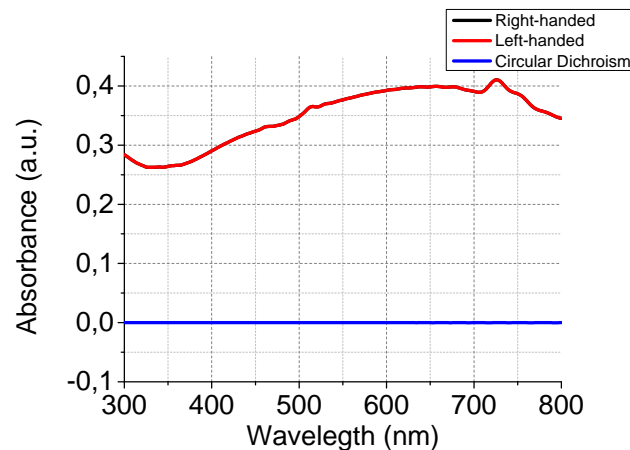


FIGURE 4.19: Results of FDTD simulations for 3D2G fractal without rotation.
 $l_1 = 120$ nm, $l_2 = 100$ nm and $w = 50$

To add chirality to our fractal structures, we introduce a new parameter – the angle of rotation. This value is describing the rotation of all generations, except the first, relative to the root. Some examples of different rotations are shown in figure 4.20. Interestingly, gammadions, a well-known chiral structure [Schäferling et al., 2012], is also a Cayley tree where the second generation is similar to the first and rotated by 90° . Note that there is an issue of overlapping within fractals starting with 3 generations (more than 3 is anyway complicated to fabricate) for large rotation angles.

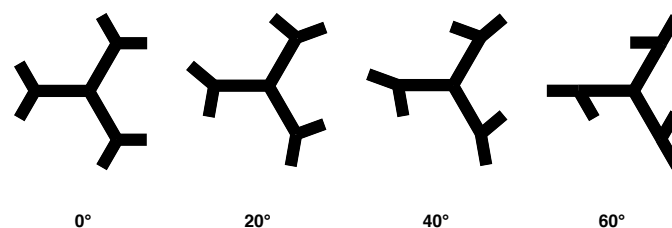


FIGURE 4.20: Sketch of different Cayley trees with added rotation (a).

As mentioned before, simulations were performed with both periodic and non-periodic boundary conditions. Both of them have disadvantages:

- Periodic boundary conditions (PBC) should show the the same result as experiment with periodic structures with correction to idealization of materials in simulation. But periodicity creates Rayleigh anomalies that disturbs the spectra by interfering with the plasmonic resonances. So to obtain far-field characteristics, like circular dichroism, PBC were used.
- Single particle simulation with PML boundaries giving should represent in transmission spectra monitor almost the same spectrum as random pattern. But not only far-field data but also a part of near-field will be detected. This can lead to the difference from the experiment results. To observe near-field effects without disturbance from lattice modes, PML boundaries were used.

For the simulations we used 3 dimensional fractals with 2 generations in order to avoid any overlapping of the branches. The rotation angle was changed from 0° to 60° . Results are presented in figure 4.21.

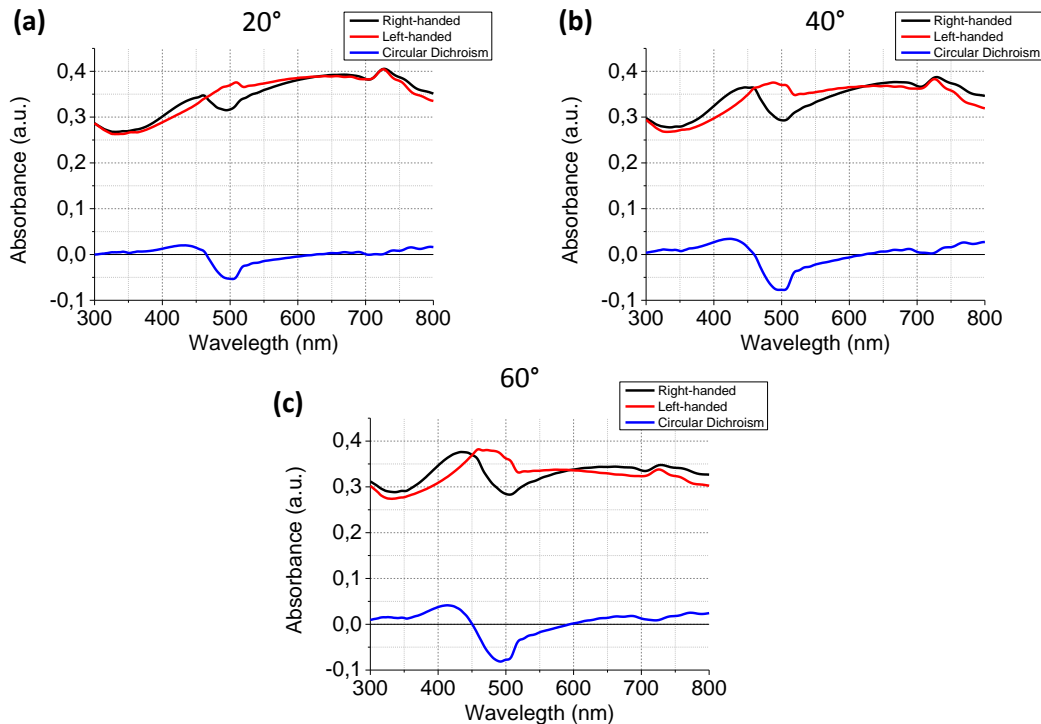


FIGURE 4.21: Results of FDTD simulations for 3D2G fractal without rotation. $l_1 = 120$ nm, $l_2 = 100$ nm and $w = 50$: (a) $\theta = 20^\circ$; (b) $\theta = 40^\circ$; (c) $\theta = 60^\circ$.

As presented in figure 4.21, numerical simulations showed that aluminum Cayley trees can create circular dichroism. The 3D2G fractal with 100 nm length for the first generation and 150 nm for the second exhibits a plasmonic resonance around 380-400 nm. Roughly in the same region, circular dichroism can be clearly seen. The absolute value of circular dichroism increases with the rotation angle. One can also notice another dichroism bump on the spectra in the red region. It has a different sign compared to the first one and a higher intensity. It appears due to the chirality of the structure in two ways at the same time with

the two edges of the second generation. For a graphical explanation see figure 4.22. Chiral structure can be presented as a superposition of two chiral structures left-handed (red) and right-handed (blue) and both of them can create chirality.

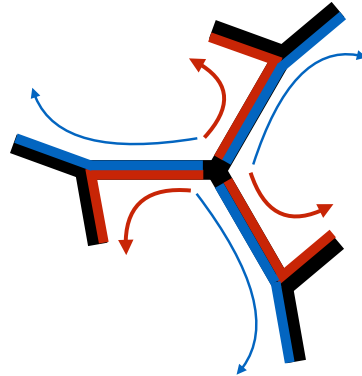


FIGURE 4.22: Graphic explanation of two chiral signs. Top view of the Cayley tree. Red color corresponds to the left-handed chirality and blue - the right-handed.

The next step is to calculate the optical chiral enhancement \hat{C} mentioned before. Values of the electric and magnetic fields were gathered from field monitors placed near the structure: 2 nm above the fractal, on the air side (TOP) and 2 nm below the fractal, inside the glass substrate (BOTTOM).

The results presented in figure 4.23 show that the optical chiral enhancement takes values $\hat{C} = [-4, 6]$. This range is comparable to what was reported in the infrared range using gold gammadion structures (figure 4.18). But in this model a randomly chosen Cayley tree was investigated. With additional script for calculating optical chiral enhancement can provide us the efficient chiral structures, i.e. further optimization should lead to the even higher values of \hat{C} . Those simulations shows a great potential for further studies and experiments.

4.3.3 Optical measurements

Samples for experimental measurements were fabricated using e-beam lithography on a quartz substrate. To generate patterns of chiral fractals, a routine was written and can be found in Annex 1. The difference with non-chiral structures pattern lies in a rotation of generations and in random patterns particles. They have not only a random displacement but also random rotation of the whole particle, while keeping chirality constant. in figure 4.24 are shown some results of this fabrication.

As it can be seen in figure 4.24, the fabrication of chiral structures requires a change in the effective dose due to the proximity effect. This affects especially particles with a rotation angle higher than 40° . For those patterns a dose study was performed, but we did not managed to achieve good results due to the high number of involved parameters, within a complicated form factor with small feature sizes.

Optical setups working in UV and Visible regions were modified to perform chirality measurements. A broadband quarter-wave plate (Thorlabs AQWP05M-340) was installed

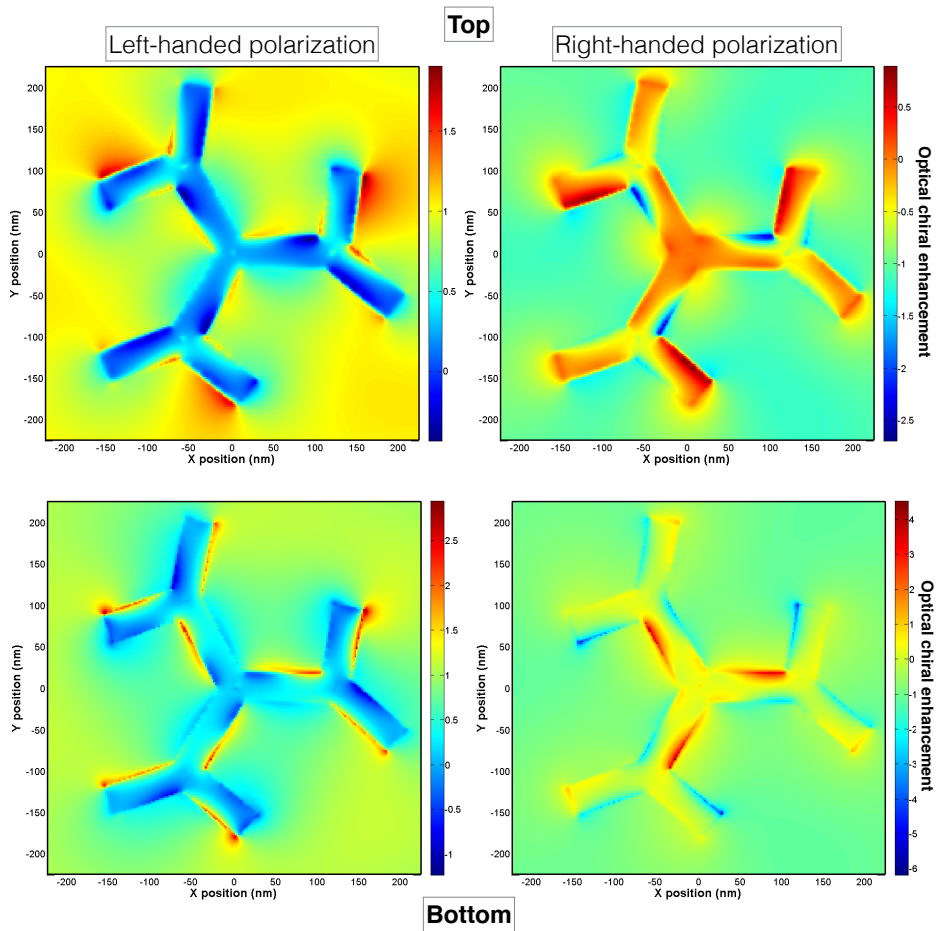


FIGURE 4.23: Optical chiral enhancement obtained from FDTD simulations for 3D2G fractal with $l_1 = 120$ nm, $l_2 = 100$ nm, $w = 50$ nm, $h = 40$ nm and rotation $\theta = 20^\circ$. The maps were computed for $\lambda = 450$ nm.

after a linear polarizer (Thorlabs GLB10), and rotated by 45° with respect to the polarization direction in order to create circularly polarized light in the UV setup described in previous section (Fig. 4.10). For the visible range, we used Thorlabs WPH05M-980 as a quarter-wave plate in pair with polarizer Thorlabs LPVISC100-MP2 and halogen lamp. This configuration leads to several issues with optical measurements, creating a slightly elliptical polarization rather than a circular one:

- Not ideal alignment. Any disturbance, even small, in the system creates imperfect circular polarization.
- Limited operating ranges of the polarization optics. On the setup different polarizers and quarter-wave plates were used to cover the whole spectrum, but those components can not be ideal everywhere. Our supplies has a gap of reliability from 500 to 700 nm, where the polarization circularity deteriorates.

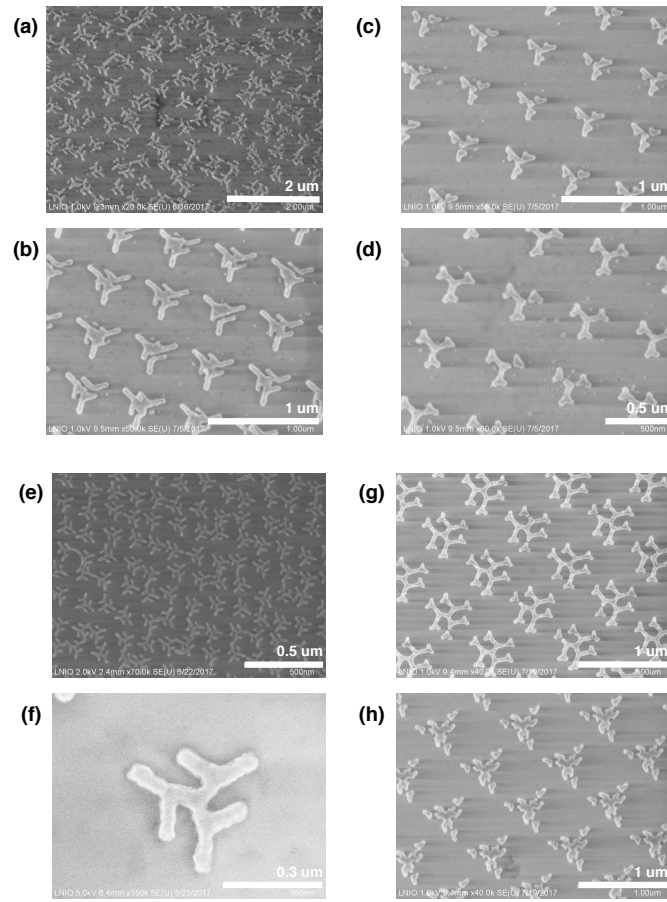


FIGURE 4.24: SEM images of (a-d,h) Unsuccessful fabrication attempt of chiral structures; (e-g) Successful fabrication attempt of chiral structures

In principle, both issues should decrease the observed circular dichroism, but cannot increase it. This means that the detection of any dichroism could be appraised as a proof of existence of chirality within plasmonic structures – even if the magnitude of the effect might be underestimated.

As a first experiment, chirality measurements have been performed only in the ultraviolet. In Fig. 4.25 the corresponding results are presented. We clearly observe circular dichroism in the spectra, with a maximum around $\lambda = 350$ nm, i.e. fabricated fractals showed chiral properties. The second peak corresponds to the longer wavelength >600 nm (out of range for the setup) and has a different sign as predicted due to the second direction of branches. However, when we tried to reproduce this result one week after the first experiment, the chiral response was almost lost. To explain this, we assume that aluminum oxidation occurred and destroyed a chiral effect within this week. As already evoked above, as fractal structures have a larger surface exposed to air than a non-fractal structure of similar dimension, they might experience higher oxidation rates. Moreover, due to the small feature size and fine details in the fractal geometry, the effect of any oxidation could significantly decrease the quality of plasmonic resonances and hence the optical chiral enhancement in the near-field. As a consequence, all further measurements were made with freshly made

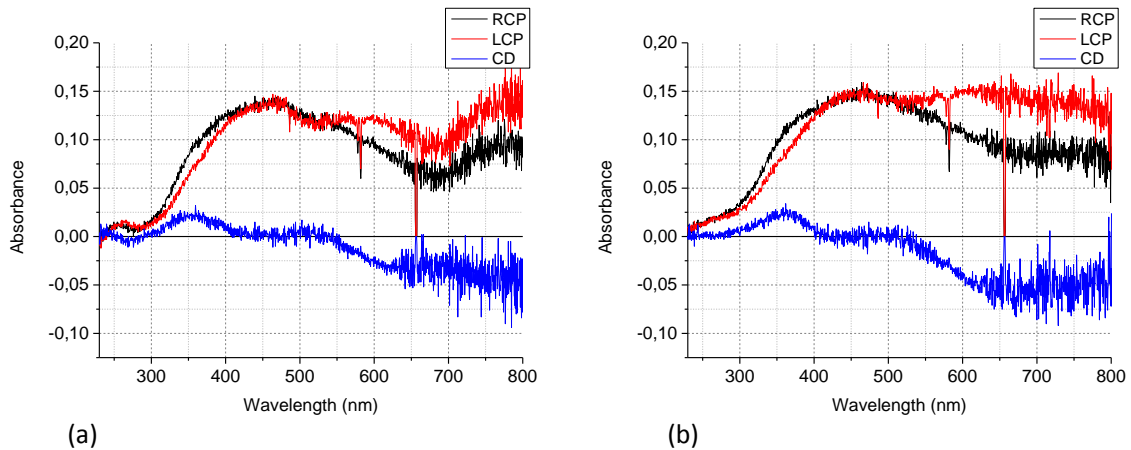


FIGURE 4.25: Absorbance spectra and calculated circular dichroism for patterns of 3D2G fractals with 20° rotation and $l_1 = 100$ nm, $l_2 = 120$ nm, $w = 50$ nm. (a) Lattice pattern (b) Randomly distributed pattern

samples to minimize oxidation.

In the next part of the study, we oriented on gathering more data in different configurations. Absorbance and circular dichroism spectra for different angles, forms and wavelengths are combined in figures 4.26, 4.27, and 4.28. Measurements were performed right after the fabrication in order to avoid oxidation issues. Even if those figures were made for the same patterns, there is not always a perfect match of the spectra, because of the different optical setups that were used for the visible and blue-UV regions. Obtained values of dichroism reached 0.05 OD (optical density) for 3 branches structures, which is around 16% of intensity.

During the experiments we observed an issue of reproducibility of fractal structures. Some structures, fabricated with the same methods, showed chirality much lower than expected or did not at all. Repeated optical experiments of the samples with realignment of the optical setup have yielded the same result, suggesting that the issue is linked with the structures themselves. However, a subsequent analysis of the patterns with an electron beam microscope did not reveal any visible structural problems with those particles. We believe that the problem might be linked with the grain structure of evaporated aluminum, which is difficult to control.

Fractals with 4 branches showed significantly lower values of circular dichroism than fractals with 3 branches. This could be also caused by fabrication issues due to the increased material density per unit surface. Furthermore, 4D fractals are limited in rotation angle and second generation, due to overlapping. Maximum achieved value is 0.02 OD at 700 nm wavelength for the structure 4D2G with 20° rotation and $l_1 = 100$ nm, $l_2 = 80$ nm, $w = 50$ nm, as shown in Fig. 4.28.

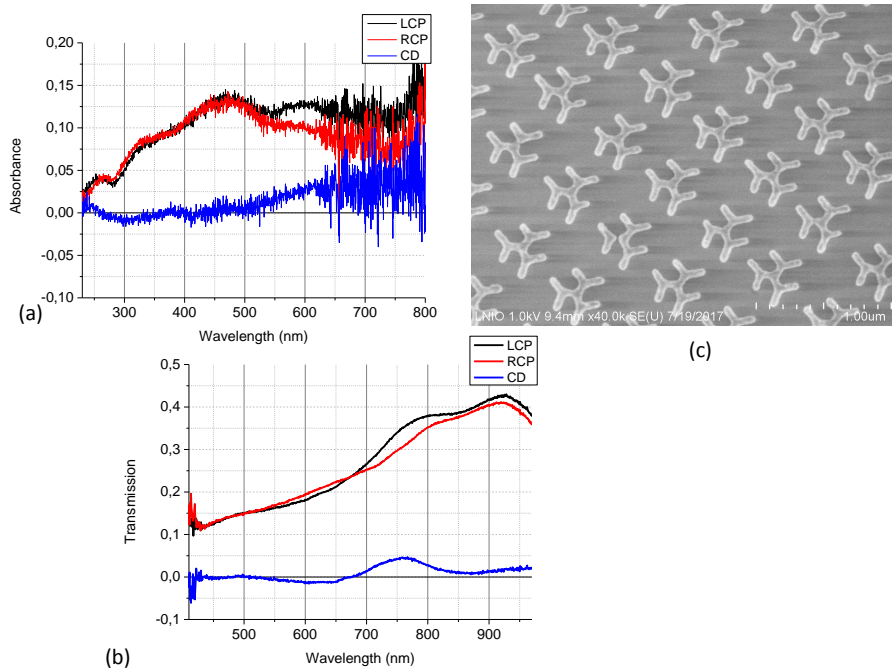


FIGURE 4.26: Absorbance spectra and calculated circular dichroism for pattern of 3D2G fractals with 20° rotation and $l_1 = 100$ nm, $l_2 = 120$ nm, $w = 50$ nm. (a) Spectrum obtained in UV part; (b) Spectrum obtained in visible part; (c) SEM picture of the structure.

4.3.4 Discussion and application of chiral aluminum fractals

Even if some problems and open questions remain, the achieved results unambiguously demonstrate the potential of fractal structures for chiral optical applications. At the moment of writing of this thesis, the problem of reproducibility of fabrication and measurements is the most critical. Any further study should focus on improving the fabrication process. Below I suggest several ideas to improve fabrication.

- Using another resist exhibiting a higher contrast than PMMA should provide much better edge writing. For this purpose, a polymer (AR-P 6200.09 from All Resist) was bought, but it requires a huge adaptation of the process to achieve the expected results.
- Gradient dose writing should compensate for proximity effects. E-line setup from Raith provides advanced tools for e-beam lithography, for example gradient writing. Though this, it should be possible to increase the electron dose while moving from the center to the edges of the fractals. This will provide a clearer shape of the third generation, and even possibility to fabricate the fourth generation with the same sizes.
- Homogeneous index around particles. It can be achieved by etching the glass with Reactive Ion Etching (RIE) and/or covering the sample with a thin layer of SiO_2 . This will prevent oxidation of aluminum and also create a uniformity in environment.

This project also involved an important part in terms of understanding the theory. To find a dependence between the geometry of the fractal and their properties can be done not

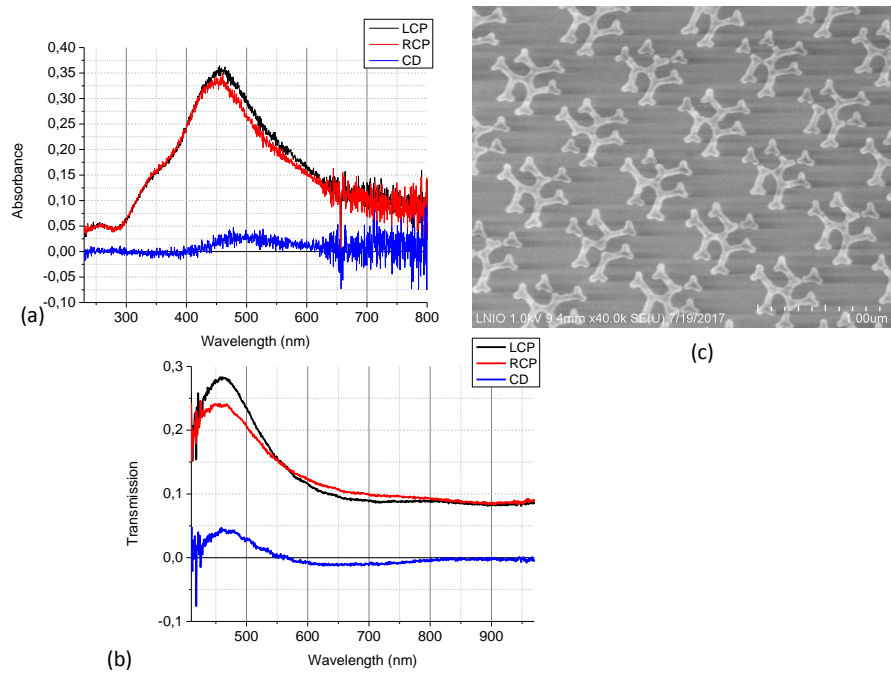


FIGURE 4.27: Absorbance spectra and calculated circular dichroism for pattern of 3D3G fractals with 20° rotation and $l_1 = 100$ nm, $l_2 = 150$ nm, $l_3 = 80$ nm, $w = 50$ nm. (a) Spectrum obtained in UV part; (b) Spectrum obtained in visible part; (c) SEM picture of the structure.

only by simple charge distribution problem, but from a mathematical point of view. Graph theory and fractal theory are great instruments to use. Prediction for fractal structures will open way to easier tuning of resonances in terms of position as well as quality.

Chiral fractal structures open a way for efficient chiral plasmonics from UV to IR ranges, allowing high customization. Fractal metasurfaces can solve several tasks at the same time, for example luminescence enhancement or light filtering combined with properties of circular polarizer. These technologies could be used in numerous optical applications and especially in enhancement of light sources for lighting.

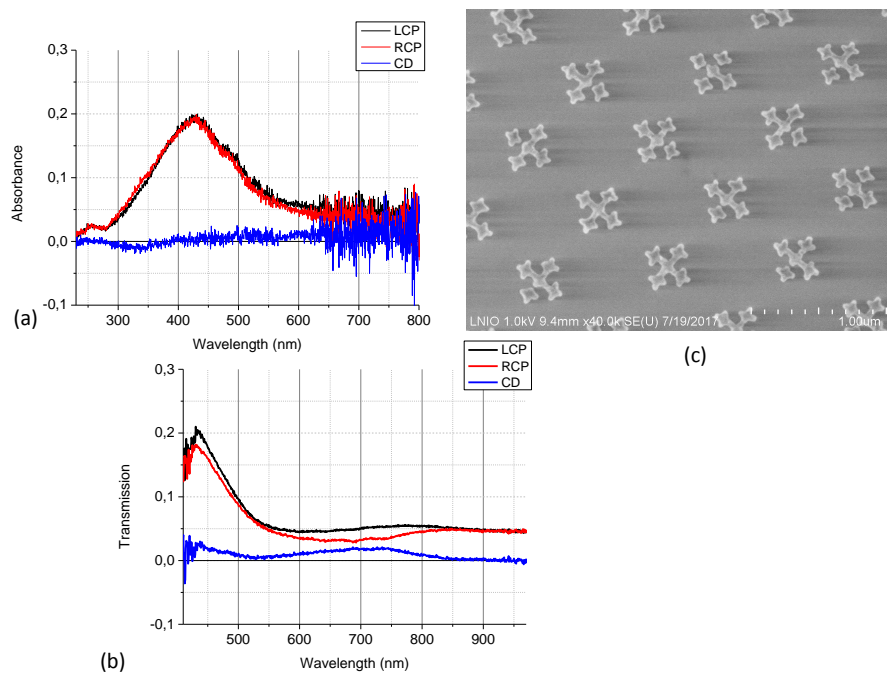


FIGURE 4.28: Absorbance spectra and calculated circular dichroism for pattern of 4D2G fractals with 20° rotation and $l_1 = 100$ nm, $l_2 = 80$ nm, $w = 50$ nm. (a) Spectrum obtained in UV part; (b) Spectrum obtained in visible part; (c) SEM picture of the structure.

General conclusion

The main goal of this thesis was to develop efficient methods of using aluminum plasmonics for optical applications, such as the coupling with wide band gap semiconductors. As described in Chapter 1, the use of aluminum for plasmonics has several advantages: aluminum is a low-cost material able to sustain plasmonic resonances in a broad range from UV to IR and has a native oxide protection film. Some disadvantages were discussed as well, mainly the high losses in the visible spectrum (see Fig. 1.7), explained by the high imaginary part of dielectric permittivity and interband transitions around 800 nm. However, aluminum plasmonics is a rapidly growing field with plenty of potential applications in light generation, theranostics and non-linear optics.

To solve the problem of low quality factor of plasmonic resonances in the visible range, we proposed a method based on the use of lattice modes. A successful study was performed with all aspects: theoretical explanation, FDTD simulation and experimental investigation. With one of the samples, an array of cylinders with diameter 60 nm and period 260 nm, we experimentally achieved a quality factor $Q \approx 13$. This is 5-10 times higher than for isolated particles.

The result of the first chapter provides us with a possibility of applying efficiently aluminum plasmonic structures to enhance light emission from wide band gap semiconductors. As an optically active material, zinc oxide was chosen by virtue of expertise in our lab. There are already several works based on the coupling of aluminum with zinc oxide, but usually they are based on geometry, where ZnO placed onto Al surface or metasurface. In our case, we developed a concept of the aluminum structures onto ZnO surface with FDTD simulations which was later realized. Experiments presented in Chapter 3 proved the suitability of this concept and showed enhancement of photoluminescence in 1.5 times in comparison with pristine ZnO epitaxial layer.

The problem encountered in Chapter 3, i.e. the lack of penetration depth of plasmonic effects, has pushed us forward to look for the more effective surface design. Based on the experience of the radio technology we adapted fractal structures to the optical range of spectra. Among the fractals, the simple structure of Cayley trees was used to compare the advantage brought by fractals in comparison with basic cylinders. FDTD simulations of aluminum Cayley trees and cylinders showed that without presence of collective effects fractal structure overcome cylinders in term of average electric field per unit surface. This could lead to the higher enhancement of optically active materials.

During the fractal structure investigation we proposed a model of chiral fractal. By combining chiral geometry with fractals we showed the possibility to realize optical chirality in the blue and near-UV parts of the spectrum. Also, a high customizability of fractals allows to

sustain several plasmonic resonances and chiral properties within the same structure. Theoretical study with FDTD simulations proved the presence of circular dichroism and of local optical chirality enhancement in described aluminum fractals. The experiments performed on fabricated chiral fractals showed the presence of dichroism in blue region and higher wavelengths.

Concerning the perspectives of this thesis, there is still plenty of work to be done. Fractals, as a complex geometry, provides high customization for different applications:

- The use of aluminum fractals in combination with wide band gap semiconductor should provide an enhancement of luminescence. An energy effective light source or detector could be based on fractal geometry.
- Also, fractal can be used to increase luminescence of quantum dots or phosphorous molecules.
- Nevertheless, aluminum fractals can be used for SERS.

With the complex geometry comes a complex fabrication process. We observed that this procedure needs an improvement to get higher reproducibility. With the use of advanced resists, it should be possible to obtain high quality fractals with sharp edges. This is especially important for the chiral fractals where geometry plays a crucial role.

Further investigation of chiral fractals can be applied in a field of molecule detection, where chirality helps to distinguish the components. Moreover, light sources with tunable circular polarization can be created based on those structures. Those sources could be interesting in 3D screen industries. Concerning screens, it is also very important to mention a "hot cell" model proposed in Chapter 4. Cayley trees with four branches can work as an optical switch remotely controlled by polarization.

Generally speaking, aluminum plasmonics is a developing field. UV optics have important applications, for example in medicine. Aluminum shows the best compatibility within this spectral range. In future years, aluminum plasmonics would be an important field with different efficient applications.

Appendix A

Script for fractals

The code was implemented using Ruby language.

As an output, it generates two ASCII tables giving the coordinates of fractals both ordered in a square lattice and randomly distributed. Each fractal is defined its vertices.

Files are adapted to use with Raith e-Line setup.

```
#Global values
$PI = Math::PI
#Desired variables

$lambd = 222 #Working wavelength for filename
$Dimension = 3 #Dimension of the tree
$Deep = 3 #Deep of the tree
$type = "ab"
$length = [120, 100, 100] #l1, l2, l3
$Width = 50 * 0.001
$Rot = ($PI/180) * 60 #Rotation angle

$length.each_index {|i| $length[i] = 0.001 * ($length[i] - $Width *
  500 * Math.tan(($PI - 2 * $PI / $Dimension) / 2))}

class Float
  def to_rad
    self/180 * Math::PI
  end
end

def generation (startX, startY, listX, listY, angle, gen, branch)
  branch2 = branch
  if branch2 < $Dimension || (gen == 0 && branch2 <=
    $Dimension)
```

```

    #puts startX
    #puts startY
a2X = startX + $length[gen] * Math.cos(angle) #Left edge
a2Y = startY + $length[gen] * Math.sin(angle)
    listX << a2X
    listY << a2Y
    gen2 = gen + 1
    #puts gen2.to_s + ', ' + branch.round.to_s + ', ' +
        branch2.round.to_s + ", x = " + a2X.round.to_s
        + ", y = " + a2Y.round.to_s
    if gen2 < $Deep
        angle2 = angle + $Rot - ($PI - 2 * $PI /
            $Dimension)
        #puts "flag 1"
        generation(a2X, a2Y, listX, listY, angle2,
            gen2, 1)
    end
    angle2 = angle
    if gen2 == $Deep
        a3X = a2X + $Width * (Math.cos(angle2 + $PI
            / 2)) #Top edge
        a3Y = a2Y + $Width * (Math.sin(angle2 + $PI
            / 2))
        listX << a3X
        listY << a3Y
        #puts 'END --- /n' + gen2.to_s + ', ' +
            branch.to_s + ', ' + branch2.to_s + ", x
            = " + a3X.round.to_s + ", y = " + a3Y.
            round.to_s
    end
    a4X = startX + $Width * (Math.cos(angle2 + $PI / 2)
        ) #Left edge
    a4Y = startY + $Width * (Math.sin(angle2 + $PI / 2)
        )
    listX << a4X
    listY << a4Y
    gen2 = gen2 - 1
    branch2 = branch2 + 1
    #puts gen2.to_s + ', ' + branch.to_s + ', ' +
        branch2.to_s + ", x = " + a4X.round.to_s + ", y
        = " + a4Y.round.to_s
    if gen2 <= $Deep

```

```

        angle2 = angle + 2 * $PI / $Dimension
        #puts "flag 2"
        generation(a4X, a4Y, listX, listY, angle2,
            gen2, branch2)          #Next branch
    end
    branch = branch + 1
end
#puts "flag 3"
end

pat_size = 60 # pattern size in micrometers
spacing = 0.7 #Center to center spacing in micrometers
sc = 0.1 #Scatter distance
quantity = ((pat_size / spacing).round).to_i #number of structures
        in a row
#filename1 = $lambda.to_s + "_" + $Dimension.to_s + "D" + $Deep.to_s
        + "G_" + $type + "_order.asc"
filename1 = "CD_120-100-100-a60.asc"
File.open(filename1, 'w') do |orderCoor|
    #filename2 = $lambda.to_s + "_" + $Dimension.to_s + "D" +
        $Deep.to_s + "G_" + $type + "_random.asc"
    filename2 = "CD_120-100-100-a60-RANDOM.asc"
    File.open(filename2, 'w') do |randomCoor|
        quantity.times do |i|
            quantity.times do |j|
                orderX = 20 - i * spacing + pat_size
                orderY = 20 - j * spacing + pat_size

                listX = [orderX]
                listY = [orderY]
                generation(orderX, orderY, listX,
                    listY, 0, 0, 1)
                listX[-1] = orderX
                listY[-1] = orderY

                orderCoor.syswrite ("1_100.0_0\n")
                listX.each_index {|i| orderCoor.
                    syswrite (listX[i].to_s + "_" +
                        listY[i].to_s + "\n")}
                orderCoor.syswrite ("#\n")
            end
        end
    end
end

```

```

        listX.clear
        listY.clear

addR1 = Random.new
randomX = orderX + addR1.rand(-sc..sc)
Random.new_seed
randomY = orderY + addR1.rand(-sc..sc)
Random.new_seed
randomRot = addR1.rand(0..$PI)

listX = [randomX]
listY = [randomY]
generation(randomX, randomY, listX,
            listY, randomRot, 0, 1)
listX[-1] = randomX
listY[-1] = randomY

randomCoor.syswrite ("1_100.0_0\n")
listX.each_index {|i| randomCoor.
    syswrite (listX[i].to_s + "_" +
        listY[i].to_s + "\n")}
randomCoor.syswrite ("#\n")
listX.clear
listY.clear

end
end

##### L letter

listX = [0, 0, 5, 5, 15, 15, 0]
listY = [0, 30, 30, 5, 5, 0, 0]
orderCoor.syswrite ("1_100.0_1\n")
listX.each_index {|i| orderCoor.syswrite (listX[i].
    to_s + "_" + listY[i].to_s + "\n")}
orderCoor.syswrite ("#\n")
listX.clear
listY.clear

##### R letter

listX = [0, 0, 5, 15, 10, 15, 10, 6, 10, 5, 5, 0]
listY = [0, 30, 30, 20, 15, 0, 0, 15, 20, 25, 0, 0]

```

```
randomCoor.syswrite ("1_100.0_1\n")
listX.each_index {|i| randomCoor.syswrite (listX[i
  ].to_s + "_" + listY[i].to_s + "\n")}
randomCoor.syswrite ("\n")
listX.clear
listY.clear
end
end
```


Appendix B

Résumé

Dans ce chapitre sera présenté un résumé de l'ensemble de la thèse en langue française.

B.1 Introduction

Les nanostructures métalliques sont les éléments de base de la nanoplasmonique et des applications sous-jacentes en nano-optique. Depuis plusieurs décennies, la plasmonique a été étudiée presque exclusivement dans la région du visible et de l'infrarouge en utilisant des nanostructures faites de métaux nobles, à savoir l'or et l'argent, qui possèdent des propriétés plasmoniques du proche infrarouge jusqu'au visible. Malgré cela, les applications émergentes nécessiteront l'extension de la nanoplasmonique vers des énergies plus élevées, en particulier dans l'ultraviolet. Par conséquent, les métaux alternatifs, souvent mentionnés comme métaux pauvres dans la littérature, apparaissent comme une solution afin d'atteindre cet objectif. Parmi tous ces métaux, l'aluminium est l'un des matériaux les plus attrayants pour étendre la nanoplasmonique au domaine de l'ultraviolet. L'aluminium est un métal bon marché, très abondant sur Terre, compatible avec l'optoélectronique et possède des propriétés plasmoniques sur une large gamme d'énergies, de l'infrarouge jusqu'à l'ultraviolet profond. Les applications de la plasmonique à base d'aluminium sont nombreuses: Raman exalté dans l'ultraviolet, marqueurs biologiques (la plupart des molécules fluorescent lorsqu'elles sont excitées dans l'UV, comme l'ADN), source laser UV ultra compactes pour la purification de l'eau, pour en nommer seulement une partie. Dans un premier temps et au travers du premier chapitre, une revue des recherches actuelles centrées sur la fabrication et la caractérisation optique et structurales de nanostructures d'aluminium est présentée, ainsi que des potentielles applications. Dans le second chapitre, nous nous intéresserons aux modes de réseaux, qui apparaissent dans les réseaux de nanostructures parfaitement ordonnées. Nous verrons que grâce à ces modes particuliers, les résonances plasmoniques supportées par les réseaux de nanostructures d'aluminium peuvent être améliorées significativement en terme de facteur de qualité. Dans le chapitre 3, la possibilité de coupler les nanostructures plasmoniques d'aluminium avec des couches d'émetteurs semi-conducteurs est étudiée. En particulier, l'approche est basée sur le couplage entre une couche semi-conductrice à large bande interdite de ZnO (oxyde de Zinc), et des nanostructures plasmoniques en aluminium. Le couplage entre les propriétés excitoniques du ZnO et les propriétés plasmoniques des nanostructures d'aluminium, toutes deux situées dans le proche

ultraviolet sont étudiées. Ce type de couplage laisse entrevoir des applications telles que les sources laser ultra-compactes dans l'UV pour l'éclairage ou pour le biomédical. Enfin le quatrième et dernier chapitre s'intéresse aux structures plasmoniques fractales et/ou chirales à base d'aluminium. Dans cette partie, la possibilité d'obtenir des résonances à la fois dans le visible et l'ultraviolet sur une même nanostructure est étudiée théoriquement et expérimentalement. De plus, nous montrons expérimentalement et numériquement la possibilité d'obtenir des structures d'aluminium supportant à la fois une chiralité droite et gauche, dans les régions du visible à l'ultraviolet proche. A nouveau, de nombreuses applications sont envisageables, telles que la détection en champ proche de molécules chirales ou encore le contrôle de la polarisation de la lumière émise par des couches minces d'émetteurs.

B.1.1 Plasmonique à base d'aluminium

De part ses propriétés physiques (notamment une fréquence plasma de l'ordre de 15 eV, l'aluminium a la particularité d'avoir des propriétés plasmoniques balayant une très large gamme d'énergie, de l'infrarouge à l'ultraviolet profond. De plus, bien que ce métal présente des pertes considérables dans le visible comparativement à l'or ou l'argent, celles-ci, dues aux transitions interbandes particulières de l'aluminium, restent relativement centrées autour de 800 nm, et deviennent faibles dans l'UV [Gérard and Gray, 2015]. On rappelle que les matériaux "classiques" utilisés depuis quelques décennies dans le domaine de la plasmonique que sont l'or et l'argent ont des propriétés plasmoniques allant de l'infrarouge jusqu'à l'UV proche (380 nm argent) ou le vert (environ 540 nm, or). Ces limitations sont dues aux transitions interbandes de ces métaux nobles. Les résonances plasmoniques supportées par les nano-structures d'aluminium restent aujourd'hui assez peu utilisées. Or, depuis quelques années se produit ce qui a été nommé l'"*Aluminum Rush*" (ruée vers l'aluminium) dans la communauté de la nano-optique/plasmonique, et le nombre d'articles sur le sujet ne cesse de croître. L'aluminium en tant que matériau plasmonique a de nombreuses applications potentielles: par exemple, la détection de systèmes organiques et biologiques [Gryczynski et al., 2004] qui présentent de fortes absorptions dans l'UV, la photocatalyse [Honda et al., 2014], le couplage avec des semi-conducteurs à large bande interdite pour l'émission de lumière UV [Zhang et al., 2014], ou encore la purification de l'eau. En outre, l'aluminium est un matériau relativement bon marché et manipulable, ce qui ouvre plus de possibilités pour la fabrication et la production de masse. Il s'agit de plus d'un métal assez stable, grâce à la formation d'une couche d'oxyde natif auto-limitante (alumine) qui protège la surface métallique d'une oxydation plus profonde et des contaminants extérieurs [Langhammer et al., 2008b].

Les propriétés optiques de l'aluminium peuvent être expliquées en considérant la figure B.1, qui montre les parties réelle et imaginaire de sa fonction diélectrique, pour les gammes UV, visible et proche infrarouge. Sur la figure B.1 sont également tracées les mêmes données pour l'or et l'argent, à titre de comparaison. Tout d'abord, en dehors de la zone spectrale centrée autour de $\lambda = 800$ nm (associée aux transitions inter-bandes), l'aluminium présente un comportement très "Drude". En regardant la partie réelle de la fonction diélectrique (B.1 (a)), il apparaît que l'aluminium conserve une valeur négative de ϵ_1 (c'est-à-dire présente un

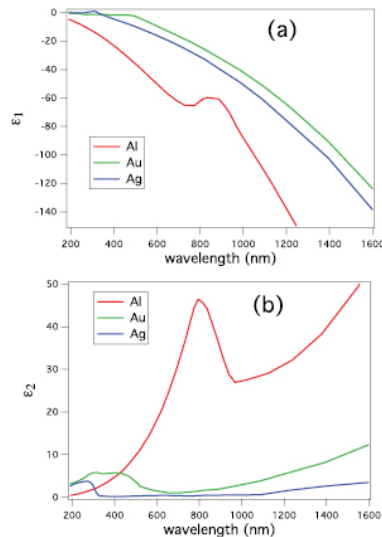


FIGURE B.1: Partie réelle (a) et partie imaginaire (b) des fonctions diélectriques pour l'aluminium, l'or et l'argent. Les données proviennent du travail de Palik, 1997 and Rakić, 1995.

caractère métallique) sur une plage plus large que l'or et l'argent. Ceci est une conséquence directe de la valeur de la fréquence plasma de l'aluminium valant $\omega_p = 15,3 \text{ eV}$. La partie imaginaire de ϵ (B.1 1 (b)) est directement liée aux pertes du métal et la situation est moins favorable pour l'aluminium par rapport à l'argent et à l'or. C'est pourquoi l'or et l'argent sont les métaux favorisés pour la plasmonique: les parties imaginaires de leurs fonctions diélectriques restent faibles sur tout le spectre visible. Cependant, en raison de la présence de transitions interbandes, l'or et l'argent ne peuvent pas être utilisés dans la gamme UV, tandis que l'aluminium présente à la fois une valeur de $\epsilon_1 < 0$ avec une valeur de ϵ_2 relativement faible dans l'UV. C'est pourquoi l'aluminium est un matériau si attrayant pour la plasmonique UV.

L'aluminium est parfois considéré comme un mauvais métal pour la plasmonique à cause de son oxydation rapide. Cet argument est une simplification excessive. Il est vrai qu'une couche native d'alumine (Al_2O_3) apparaît à la surface d'une particule d'Al ou d'une couche d'Al en quelques minutes lorsqu'elle est exposée à l'air. Cela dit, une étude approfondie datant de 2008 sur l'oxydation de films minces d'aluminium (20 nm) pour la plasmonique a été faite en utilisant la spectroscopie de photoélectrons X à résolution angulaire (XPS) Langhammer et al., 2008b. Les mesures sont présentées sur la figure B.2 et montrent qu'une couche d'oxyde natif est formée en quelques heures d'exposition à l'air, avec une épaisseur se stabilisant à 2,5-3 nm (B.2 2 (a)). L'épaisseur de la couche d'oxyde reste alors stable pendant au moins 30 jours, montrant que l'oxyde natif agit comme une couche de passivation empêchant une oxydation ultérieure. On n'observe donc aucune oxydation supplémentaire, contrairement à l'oxydation des nanostructures d'argent par exemple.

Comme exemple relativement récent, nous pouvons citer les travaux de Knight *et al.* Knight et al., 2014, dans lesquels les propriétés plasmoniques des nano-bâtonnets et de

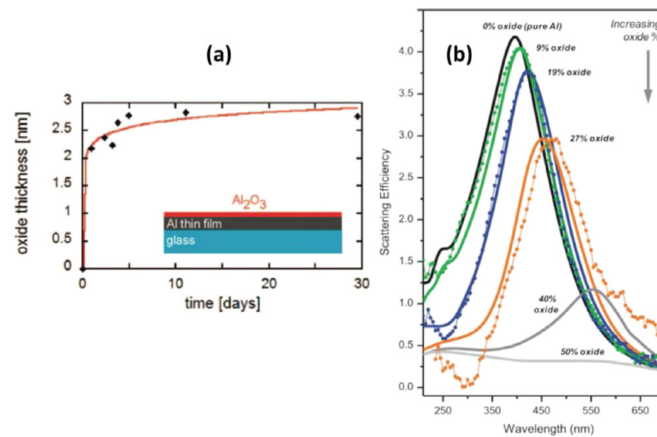


FIGURE B.2: (a) Mesures XPS à résolution angulaire de l'épaisseur de la couche d'oxyde natif sur une couche d'Al de 20 nm d'épaisseur. Les marques sont des données expérimentales, la ligne pleine est un ajustement logarithmique direct aux données XPS. (b) Spectres de diffusion de nanodisques d'Al de diamètre 100 nm avec une fraction d'oxyde variable. Extrait de Knight et al., 2014.

nano-disques d'aluminium ont été étudiées. Les auteurs ont envisagé que les nanostructures d'aluminium pourraient conduire à de multiples applications, incluant par exemple des guides d'ondes et des interconnexions plasmoniques compatibles avec la technologie CMOS. Ce travail a confirmé la possibilité d'accorder les résonances plasmoniques des nanostructures faites en aluminium du proche ultraviolet jusqu'au visible. Cette forte accordabilité est illustrée sur la figure B.3, où les spectres de diffusion (champ sombre) de nano-disques d'aluminium individuels avec des diamètres allant de 70 à 180 nm sont donnés.

Comme nous l'avons mentionné précédemment, les applications de la plasmonique à base d'aluminium sont nombreuses. Nous allons en décrire succinctement quelques unes dans ce qui suit. Premièrement nous pouvons discuter d'un résultat récent extrêmement intéressant concernant la fabrication d'une nano-source laser assistée par plasmon [Zhang et al., 2014]. Ici, une source laser miniaturisée (quelques micromètres) plasmonique émettant dans l'UV proche a été démontrée. Sa conception est basée sur la géométrie suivante, indiquée sur la figure B.4(a). Le milieu à gain est un nanofil triangulaire de GaN, un semi-conducteur à grand gap (3,4 eV) séparé d'un film nanométrique d'aluminium par une couche ultra-mince (8 nm) de SiO_2 . La structure Al / SiO_2 / GaN résultante supporte un mode plasmonique hybride, dont la distribution du champ électrique est également représentée sur la figure B.4 (b). L'énergie électromagnétique est fortement concentrée à l'intérieur de la couche isolante, formant la cavité laser. La figure B.4 (c) montre le calcul de la distribution du facteur de Purcell associé, montrant qu'un grand volume du nanofil de GaN acquiert un facteur de Purcell compris entre 7 et 10, ce qui va grandement augmenter l'émission excitonique. En pompage optique avec une source laser pulsée de 355

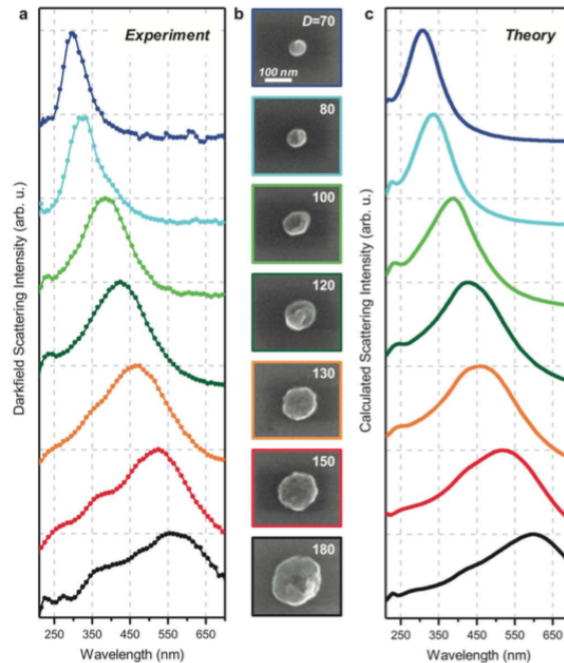


FIGURE B.3: Accordabilité des résonances plasmoniques supportées par des nano-disques d'Al fabriqués à l'aide de la lithographie par faisceau électronique. (a) Spectres de diffusion expérimentaux de nano-disques individuels de diamètres différents ($D = 70, 80, 100, 120, 130, 150, 180$ nm). (b) Images MEB des nano-disques correspondants. La barre d'échelle est de 100 nm. (c) Simulations par FDTD des spectres de diffusion, en supposant une épaisseur d'oxyde en surface de 3 nm et un substrat de SiO_2 . Extrait de Knight et al., 2014.

nm, l'émission laser à température ambiante à $\lambda = 370$ nm est observée dans le spectre d'émission (figure B.4 (d)) sous la forme d'un pic net indiquant la présence d'émission stimulée.

Les nanoparticules métalliques ont été utilisées pendant des siècles pour créer des matériaux colorés. La coupe romaine connue sous le nom de coupe de Lycurgue, ainsi que quelques vitraux des églises médiévales, ont été faites en incorporant des nanoparticules de métal à l'intérieur du verre. Les couleurs visibles sont alors directement définies par les longueurs d'onde diffusées par les NP métalliques. Si l'utilisation de métaux nobles est appropriée pour de tels objets finement ouvragés, leur prix peut devenir un problème lors du passage à la production de masse. L'aluminium est compatible avec la production de masse contrairement aux métaux nobles pour des raisons évidentes. Une application très impressionnante de l'utilisation de nanostructures d'aluminium à des fins esthétiques est la reproduction d'un tableau de Monet [Tan et al., 2014], comme on peut le voir sur la figure B.5. Dans cette étude, la palette de couleurs est définie par des pixels plasmoniques constitués de nano-disques d'Al au sommet de nano-piliers diélectriques en résine photosensible, de diamètres et d'espacements variables. La structure est supportée par un substrat de silicium recouvert également d'aluminium agissant comme un rétro-rélecteur "blanc". La peinture originale

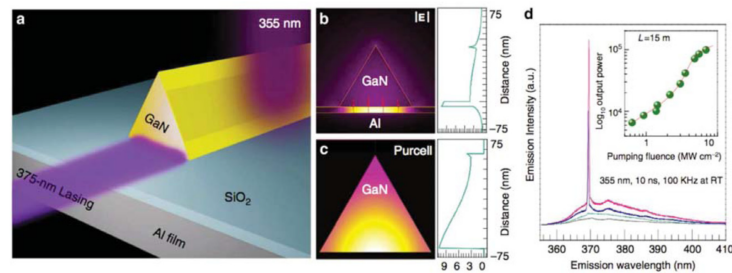


FIGURE B.4: Nanolaser plasmonique émettant dans l'ultraviolet. a) Schéma de la structure. (b) Calcul par FDTD du champ électrique absolu autour du dispositif à $\lambda = 370$ nm, montrant le degré élevé de confinement de l'énergie à l'intérieur de la couche isolante. Les flèches rouges indiquent la direction du champ électrique. (c) Distribution calculée du facteur Purcell à l'intérieur du nanofil de GaN. d) Caractérisation expérimentale de l'émission laser: spectres d'émission dépendant de la puissance du dispositif, montrant l'apparition d'un pic net au-dessus du bruit spontané. Encart: émission intégrée en fonction de l'intensité de pompage. Extrait de Zhang et al., 2014.

(visible sur le tableau a) est ainsi reproduite sur $300 \times 300 \mu\text{m}^2$, et est constituée de pixels plasmoniques dont la couleur est accordée grâce aux divers paramètres géométriques des nanostructures dans chaque pixel. Sur le panneau (b) est représentée la peinture reproduite expérimentalement en utilisant la palette de base, où les couleurs sont définies en faisant varier uniquement les tailles de nanoparticules. La palette limitée est incapable de reproduire les nuances de couleurs de la peinture de Monet. De manière frappante, avec une double variation de la taille et de l'espacement des nanoparticules d'Al dans chaque pixel, la complexité des propriétés de diffusion de chaque pixel permet une reproduction très fidèle de la peinture, ce qui est visible dans le panneau (c) (voir aussi le zoom dans le panneau (d)). Une image MEB des pixels plasmoniques est présentée dans le panneau (e): les couleurs vues sur la figure B.5 (c) sont des couleurs structurales créées par ces nanostructures. Cette reproduction des couleurs réaliste ne se limite pas aux applications liées aux beaux-arts, mais concerne également des applications telles que le marquage de sécurité ou le stockage d'informations.

Les quelques travaux récents discutés ci-avant illustrent le potentiel de la plasmonique à base d'aluminium. Les propriétés physiques et optiques de ce métal sous forme nanostructurée ouvrent la voie à d'innombrables études avec autant d'applications dans la nano-optique opérant de l'infrarouge à l'ultraviolet. Une multitude d'autres études et d'applications potentielles ont d'ailleurs été publiées dans la littérature. Bien qu'une liste exhaustive ne saurait être donnée, bon nombre de ces travaux peuvent être trouvés dans les articles de

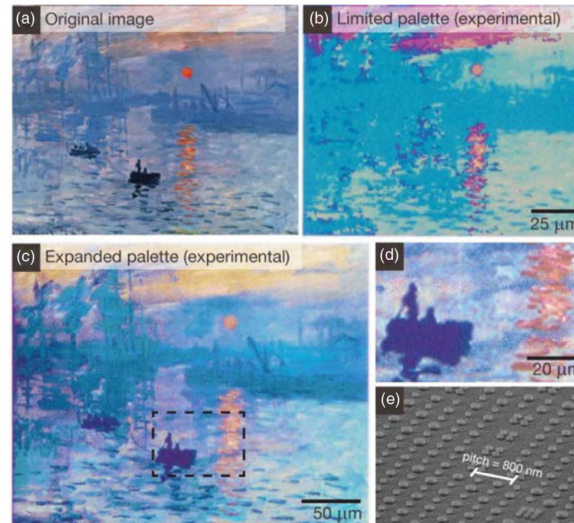


FIGURE B.5: Les couleurs structurales des nanoparticules d'Al reproduisent "impression, soleil levant" de Claude Monet. a) Image originale. b) Reproduction utilisant la "palette plasmonique limitée" (variation du diamètre des nanoparticules). (c) Reproduction utilisant la "palette plasmonique étendue" (variation du diamètre des nanoparticules et de l'espacement entre elles). (d) Image avec un grossissement plus élevée du panneau précédent. (e) Image MEB des pixels plasmoniques. Extrait de Tan et al., 2014.

revue [Gérard and Gray, 2015] et [Martin and Plain, 2015] données dans les références ci-après.

B.2 Modes de réseau

Les nanoparticules métalliques disposées en réseaux supportent à la fois des plasmons de surface localisés (LSP) dans le champ proche de chaque nanoparticule, et ont à la fois un comportement de réseau diffractif. Ce dernier effet est lié à la période du réseau ou encore la distance interparticulaire. En sélectionnant judicieusement à la fois la période du réseau et la taille des nanoparticules, il est possible de générer des modes de réseau qui sont formés par l'interférence des LSP et de l'anomalie de réseau ou anomalie de Rayleigh, qui correspond aux modes diffractifs. Ces modes hybrides ont une forme spectrale particulière de type Fano avec une largeur à mi-hauteur (ou FWHM pour Full Width at Half Maximum) réduite par rapport aux mêmes LSP non couplés aux modes de réseau. Dans ce chapitre, nous étudions les modes de réseau supportés par les réseaux de nanoparticules d'aluminium dans le visible et l'UV, expérimentalement et théoriquement. Les courbes de dispersion mesurées et simulées permettent d'analyser en détail le couplage LSP avec les anomalies de Rayleigh dans le réseau. Un réseau de nanodisques d'aluminium étudié dans ce chapitre est présenté sur la figure B.6.

Nous montrons dans la suite que lorsque la position spectrale de l'anomalie de Rayleigh (dépendant de la période du réseau) est légèrement décalée vers le bleu par rapport à la résonance LSP, le facteur de qualité du mode réseau est significativement amélioré. Nous

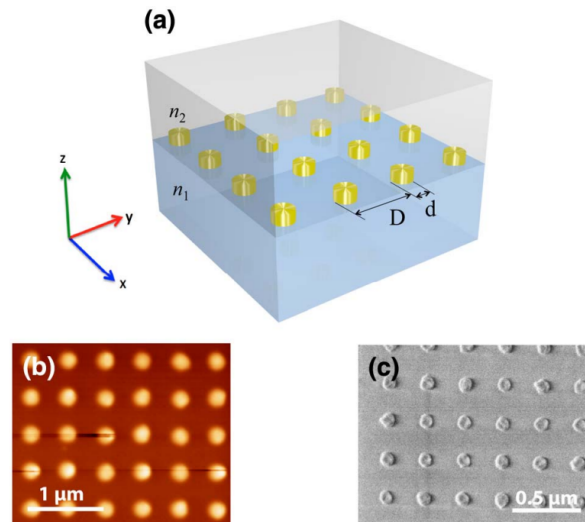


FIGURE B.6: (a) Schéma d'un réseau de nanoparticules métalliques déposées sur un substrat diélectrique d'indice de réfraction n_1 . Le superstrat peut être de l'air ou un diélectrique d'indice de réfraction n_2 . (b) Image AFM d'un réseau carré de nanodisques d'aluminium avec $D = 480$ nm, $d = 160$ nm et $h = 50$ nm. (c) Image de microscopie électronique à balayage d'un réseau de nanodisques en aluminium avec $D = 300$ nm, $d = 120$ nm, et $h = 50$ nm.

montrons également que la formation des modes de réseau dépend de façon critique de la polarisation de la lumière incidente. L'efficacité de couplage entre les LSPs et la lumière diffusée dans le plan est maximale lorsque la direction de polarisation est perpendiculaire à la direction de propagation de l'onde rasante. Les résultats obtenus fournissent des méthodes de conception afin d'obtenir pour des résonances avec des facteurs de qualité (que l'on notera Q pour Quality factors) comparables à ceux de l'or dans le visible et encore plus élevés dans l'ultraviolet. Les courbes de dispersion expérimentales mesurées dans le visible sont présentées sur la figure B.7 pour les deux polarisations. Comme le diamètre des nanoparticules métalliques est maintenu constant tandis que la période change, la position spectrale des anomalies de Rayleigh change pour une résonance LSP fixe. L'effet est clairement observé pour la polarisation s en comparant les Figures B.7 (a) et (c). Sur la figure B.7 (a), l'anomalie est située loin du LSP, et une interaction faible est observée avec la résonance LSP, beaucoup plus large. Sous incidence normale, la largeur FWHM observée est assez similaire à celle d'une nanoparticule d'aluminium isolée ($Q = 2,5$).

Lorsque la période est augmentée à 300 nm, la position de l'anomalie de Rayleigh (1,0) se déplace vers des longueurs d'onde supérieures et un plus fort couplage des résonances LSP est observé, ce qui se traduit par un fléchissement de la branche associée au plasmon ainsi qu'une diminution de la FWHM quand l'angle d'incidence augmente. En incidence normale, la FWHM est significativement plus faible que précédemment ($Q \approx 5$) et la résonance s'affine lorsque l'angle d'incidence augmente ($Q = 9,5$ pour $\theta = 32^\circ$). Enfin, pour une distance inter-particules de 350 nm, l'anomalie est très proche de la résonance LSP, conduisant à un couplage plus fort et à l'apparition d'un mode de réseau plus fin ($Q = 9$ en incidence normale). Pour la polarisation p (figures B.7(d) et (e)), nous observons clairement la même

FWHM en incidence normale à cause de la symétrie des nanoparticules. Cependant, une très faible dépendance angulaire est observée ni de claire réduction de la FWHM. Ceci est dû à la faible efficacité de couplage entre les LSP excités en polarisation p près de l'anomalie de Rayleigh (1,0). Nous notons également que l'anomalie de Rayleigh à l'interface verre / air influence la courbe de dispersion [voir Figure B.7 (e)], alors qu'elle devrait être absente dans un environnement homogène. Comme expliqué en détail dans la thèse, cela est probablement dû à l'épaisseur finie de la couche de PMMA et à la présence d'inclusions d'air à l'intérieur de cette dernière.

Les facteurs de qualité obtenus en polarisation s peuvent être comparés aux facteurs de qualité pour les nanoparticules d'aluminium isolées, qui sont généralement de l'ordre de $Q = 3-4$ dans le domaine visible. Ainsi, l'ingénierie de la FWHM est rendue possible grâce aux modes de réseau, ce qui permet d'atteindre des facteurs Q comparables à des nanoparticules d'or isolées dans le visible, de l'ordre de 10. Il est également intéressant de comparer les Figures B.7 (b) et B.7 (c). Pour ces dernières, l'anomalie est très proche de la position spectrale du LSP, conduisant à une forte résonance en incidence normale pour laquelle l'intensité diminue de façon spectaculaire lorsque l'angle d'incidence augmente. En revanche, sur la figure B.7 (b), la FWHM de la résonance en incidence normale est plus élevée (en raison du décalage plus important entre la fréquence du LSP et celle de l'anomalie), mais au fur et à mesure que l'angle d'incidence augmente, la résonance s'affine sans pour autant perdre trop en intensité. Les modes hybrides LSP-anomalies de Rayleigh sont donc utiles si l'on veut améliorer la qualité des résonances plasmoniques de l'aluminium dans le visible. Les cartographies du champ électrique, disponibles dans le manuscrit de thèse, montrent que les modes hybrides, contrairement aux modes plasmoniques purs, sont délocalisés sur les fronts d'ondes du mode de diffraction dans le plan de l'échantillon. Ainsi ces modes sont moins affectés par les pertes ohmiques que les modes LSP qui sont essentiellement localisés dans le champ proche du métal.

Finalement, nous nous sommes intéressés à des nanodisques en aluminium qui supportent des résonances LSP dans les régions bleue et proche UV. Comme expliqué dans l'introduction, l'aluminium peut supporter des résonances LSP jusqu'aux longueurs d'ondes situées dans les UV profonds. Cependant, le diamètre des particules est une forte limitation pratique (les petites tailles requises étant difficiles à fabriquer). Nous avons donc fabriqué des nanoparticules de diamètre 60 nm comme bon compromis entre la possibilité d'obtenir des résonances UV et les contraintes de fabrication. La période du réseau est fixée à $D = 260$ nm. Nous avons choisi le superstrat en air pour l'expérience afin d'éviter tout red-shift de la résonance plasmon dans le visible avec l'environnement diélectrique. De plus, le PMMA pourrait absorber dans l'ultraviolet et compromettre l'expérience. Les courbes de dispersions expérimentales pour la polarisation s sont présentées sur la figure B.8. On observe une interaction claire entre la résonance LSP autour de 420 nm et la lumière diffusée près de l'anomalie Rayleigh (1,0), conduisant à l'hybridation attendue et à l'apparition d'une résonance plus fine avec un meilleur facteur de qualité. En incidence normale, nous obtenons $Q = 8$, valeur qui doit être comparée à $Q = 4-5$ obtenue pour des particules d'aluminium isolées, que l'on peut trouver dans la littérature.

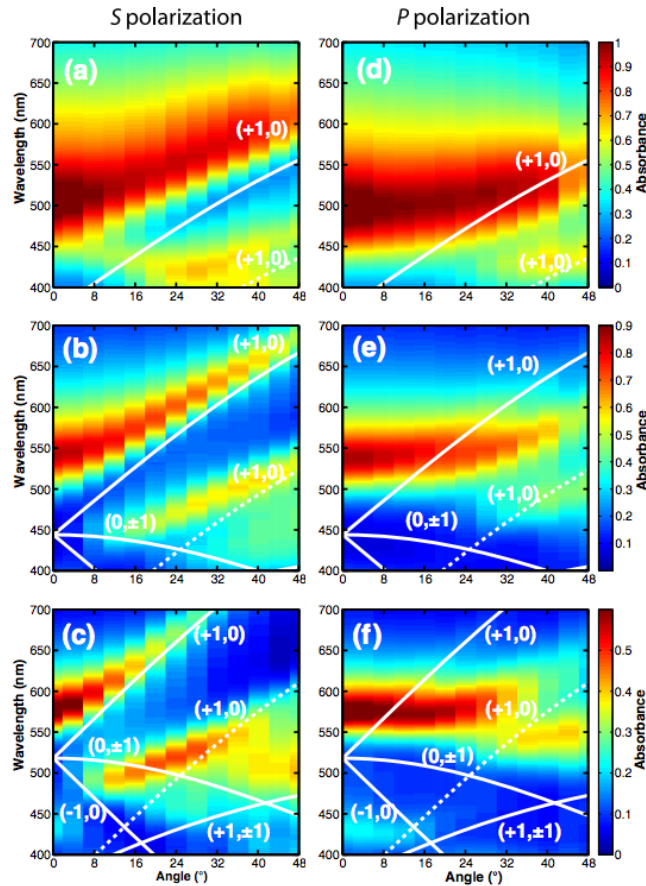


FIGURE B.7: Courbes expérimentales de dispersion mesurées sur des réseaux de nanodisques en aluminium recouverts de PMMA pour la polarisation s (a) - (c) et la polarisation p (d) - (f) p. Le diamètre des nanoparticules est de 120 nm. La période du réseau est $D = 250$ nm (a,d); 300 nm (b,e); et (c,f) $D = 350$ nm. Les lignes blanches représentent la position des anomalies de Rayleigh calculées dans la thèse pour les interfaces verre / verre (lignes pleines) ou verre / air (lignes pointillées). Extrait de Khlopin et al., 2017.

B.3 Couplage avec un semiconducteur

L'efficacité énergétique apparaît désormais comme une nécessité pour toutes les technologies futures. Étant donné que les futurs composants pour la nano-optique reposeront sur des sources lumineuses ultra-compactes, ces nouvelles sources lumineuses devront également être conçues pour être éco-énergétiques. Cela implique d'extraire plus de lumière du matériau actif constituant la source de lumière. Dans les lasers conventionnels, la limite inférieure du milieu actif est typiquement la moitié de la longueur d'onde de fonctionnement, conduisant à une taille de dispositif minimale de quelques centaines de nm. Pour rompre cette limite, il a été montré que le couplage du milieu actif laser (alliages semi-conducteurs) avec des nanostructures métalliques permet le confinement de l'énergie optique dans les plasmons de surface, donc dans des volumes nanométriques. Dans ce chapitre, nous discutons du couplage entre des structures plasmoniques en aluminium avec des couches minces

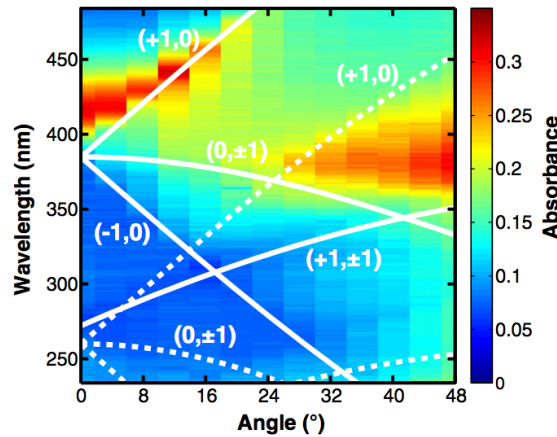


FIGURE B.8: Courbes de dispersion expérimentale mesurées sur des réseaux de nanodisques en aluminium de 60 nm de diamètre dans l’ultraviolet pour la polarisation s. La période du réseau est $D = 260$ nm. Les lignes blanches représentent la position de l’anomalie de Rayleigh calculées pour les interfaces du verre / verre (lignes pleines) ou verre / air (lignes pointillées). Extrait de Khlopin et al., 2017.

de semi-conducteurs en ZnO pour améliorer la génération de lumière émise. Nous passons brièvement en revue les propriétés des matériaux actifs pour l’émission de lumière bleue et ultraviolette. Ensuite, nous présentons la conception d’une source de lumière à base d’oxyde de zinc assistée par plasmons de surface localisés à l’aide d’une couche nanostructurée faite de nanoparticules d’aluminium. Nous discutons également les résultats expérimentaux obtenus puis tirons quelques perspectives pour les applications potentielles futures.

Nous nous intéressons donc ici à l’interaction entre le matériau semi-conducteur en ZnO (oxyde de Zinc) et des nanostructures plasmoniques d’aluminium. Le ZnO est un matériau semi-conducteur possédant des propriétés excitoniques dans le domaine de l’UV proche (énergie de gap de 370 nm). Le ZnO a suscité un grand intérêt durant cette dernière décennie en raison de ses propriétés intrinsèques uniques. Il est piézo-électrique, possède une large bande interdite électronique (3,36 à 3,4 eV) avec une énergie de liaison excitonique élevée (60 meV) et un gain optique élevé. De plus, il est très sensible à son environnement. C’est aujourd’hui un des matériaux phares et des plus prometteurs pour la synthèse de composants optoélectroniques innovants et opérants dans la gamme spectrale proche UV au visible. Enfin, il est robuste et beaucoup moins onéreux en terme de fabrication que ces concurrents nitrurés (GaN, AlN, BN et leurs alliages).

Nous avons choisi dans cette étude une conception d’échantillon représentée sur la figure B.9. Il s’agit d’un réseau de nanoparticules d’aluminium déposé sur un film mince de ZnO. Celles-ci sont dimensionnées de telle sorte qu’elles supportent des résonances plasmoniques aux alentours de 375 nm, proche de l’énergie de bande interdite de la couche active de ZnO. De plus, l’utilisation d’un réseau de diffraction peut avoir un double impact. Tout d’abord, des réseaux de nanoparticules permettent d’accorder la longueur d’onde de la

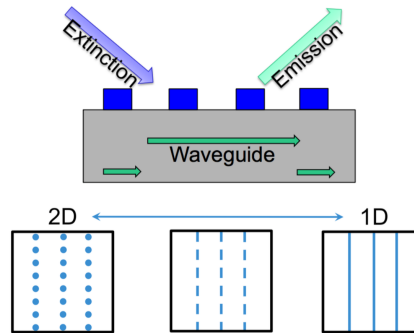


FIGURE B.9: Schéma de principe de l'échantillon: nanostructures d'aluminium lithographiées sur une couche mince de ZnO.

résonance plasmonique des nanoparticules avec l'anomalie de Rayleigh, comme décrit dans le chapitre précédent, afin d'obtenir des résonances avec des facteurs de qualité élevés, de l'ordre de 10. Le deuxième avantage attendu est que le réseau de nanoparticules permettra d'augmenter le taux d'absorption de la lumière à l'intérieur de la couche de ZnO, qui sera potentiellement piégée et guidée dans la couche de ZnO. Cet effet peut considérablement augmenter le rendement quantique externe de la couche de ZnO. Le réseau de diffraction situé sur la couche de ZnO peut être un réseau 1D (lignes périodiques, ou un réseau 2D (c'est-à-dire une matrice de nano-structures), ou une configuration hybride entre les deux que l'on pourrait nommer un réseau 1.5D (comme les lignes en pointillées représentées sur la figure B.9). Nous avons essayé de fabriquer ces trois structures, mais malheureusement nous avons rencontré un problème avec les structures 1D et 1.5D. La fabrication a été réalisée en utilisant la lithographie par faisceau électronique et la méthode de *lift-off*, avec le PMMA comme résine positive. En raison de la petite surface de contact du polymère non-exposé après irradiation par faisceau de électrons, le polymère peut, au cours du processus de développement, se détacher et changer de position, donnant une structure mal imprimée. Une meilleure solution pour produire de telles structures serait par exemple l'utilisation de la gravure ionique réactive sur une surface d'aluminium évaporée.

Sur la figure B.10 est présenté le schéma de la structure étudiée dans ce chapitre (a) ainsi qu'une image MEB de nano-cylindres d'Al déposés sur la couche de ZnO (b). Les mesures de photo-luminescence ont été effectuées sur un banc de micro-photoluminescence disponible dans notre laboratoire dont le schéma de principe est donné sur la figure B.11. Un laser He-Cd (Coherent) émettant à une longueur d'onde de 325 nm avec une puissance de 10 mW en continu est utilisé comme source d'excitation. Le spot de collection du signal a un diamètre d'environ 1 μm . En comparaison avec la taille du motif lithographié (30 μm) le spot de collection est relativement petit, ce qui permet une bonne sélection spatiale des différentes zones (ZnO avec ou sans nanostructures d'aluminium sur le dessus).

Des spectres de micro-photoluminescence mesurés sur l'échantillon décrit ci-dessus sont

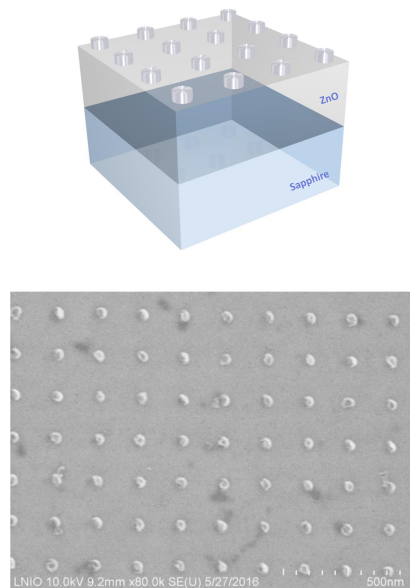


FIGURE B.10: (a) Schéma de l'échantillon. (b) Image MEB des nanostructures en aluminium.

présentés sur la figure B.12a. Les résultats expérimentaux montrent une amélioration modérée de la luminescence de la couche mince de ZnO lorsque cette dernière est recouverte par les nano-cylindres d'aluminium. Dans les meilleures conditions, le facteur d'exaltation atteint une valeur de 1,5 pour une plage de longueurs d'ondes comprises entre 360 et 380 nm, centrée autour du pic d'émission de la couche de ZnO, comme on l'observe sur la figure B.12b. Il est important de préciser que les résonances plasmoniques supportées par les nano-cylindres d'aluminium ont été mesurées par spectroscopie d'extinction et présentent un maximum centré à 380 nm (ces résultats ne sont pas montrés ici). Les résonances plasmoniques sont donc "alignées" avec le pic d'émission de la couche de ZnO afin d'optimiser le couplage entre les propriétés plasmoniques (Al) et excitoniques (ZnO). Ce résultat n'est pas à la hauteur de nos attentes et mérite quelques explications. Tout d'abord, nous avons une couche assez épaisse d'oxyde de zinc (150 nm) par rapport à la profondeur de pénétration typique du champ électrique localisé autour des nanostructures d'aluminium (typiquement quelques dizaines de nm, calculé par FDTD). En d'autres termes, le volume modal plasmonique autour d'une nanoparticule qui contribue à l'exaltation de luminescence par couplage est très inférieur au volume du matériau actif (massif) de la couche de ZnO. Cela signifie que la majeure partie du matériau actif n'est pas couplée au champ proche des particules métalliques. La distribution spatiale du champ électrique, obtenue à partir de simulations FDTD, a été calculée dans ce travail de thèse. Pour compenser l'influence du volume découplé, et ainsi remonter à une valeur d'exaltation plus proche de la réalité, une normalisation peut être effectuée. Les volumes couplés et non couplés sont alors estimés à partir des simulations. Avec cette méthode, la valeur maximale du facteur d'exaltation de la photo-luminescence normalisé est d'environ 30. Cette valeur est plus proche de nos attentes initiales et correspond aux mesures faites sur le meilleur échantillon.

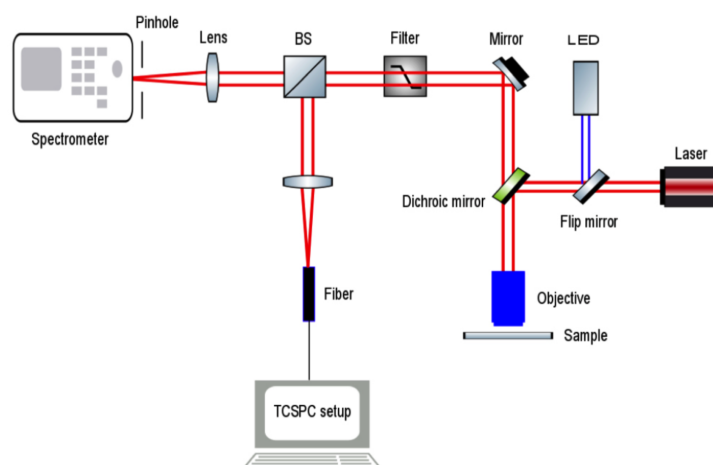


FIGURE B.11: Schéma du banc de micro-photoluminescence utilisé au laboratoire. Extrait de Rahbany, 2016.

Dans ce chapitre, nous avons démontré que les nanostructures d'aluminium ont un potentiel certain pour exalter la luminescence de semi-conducteurs à large bande interdite tel que l'oxyde de zinc. Même si ce n'est pas la configuration la plus efficace, avec les nanocylindres d'aluminium lithographiés sur le dessus de la couche de ZnO, nous avons obtenu des facteurs d'exaltation de 1,5 (brut) et d'environ 10 en moyenne (normalisé). La structuration des deux matériaux (ZnO et aluminium) est une voie possible de poursuite de ce travail. Par exemple, l'utilisation de nanostructures en ZnO telles que des nano-fils couplés à des nano-structures d'aluminium est une configuration très prometteuse qui devrait donner un couplage beaucoup plus efficace. Ce type de nano-matériaux hybrides (métal / semi-conducteur nanostructurés) ont des applications potentielles très variées telles que les sources lasers ultra confinées, le biomédical, la détection ultra sensible d'agents chimiques, ou encore la purification de l'eau et le photovoltaïque.

B.4 Plasmonique dans le visible et l'ultraviolet avec des nanostructures d'aluminium fractales et chirales

Les valeurs relativement faibles du facteur d'exaltation de la photo-luminescence d'une couche mince de semi-conducteur assistée par la plasmonique observée au chapitre 3 est un problème assez général lorsque le volume d'émetteurs est élevé par rapport au volume occupé par le champ proche des nanostructures. Cette limitation peut entraver le développement d'applications basées sur la nanostructuration de métaux. Afin de trouver une solution à ce problème, nous avons adopté une tactique inspirée de la technologie des radiofréquences: les antennes fractales. Dans ce chapitre, nous étudions théoriquement et expérimentalement l'utilisation de nanoparticules d'aluminium de formes fractales spécifiquement adaptées pour la plasmonique dans le visible et le proche UV. Les structures

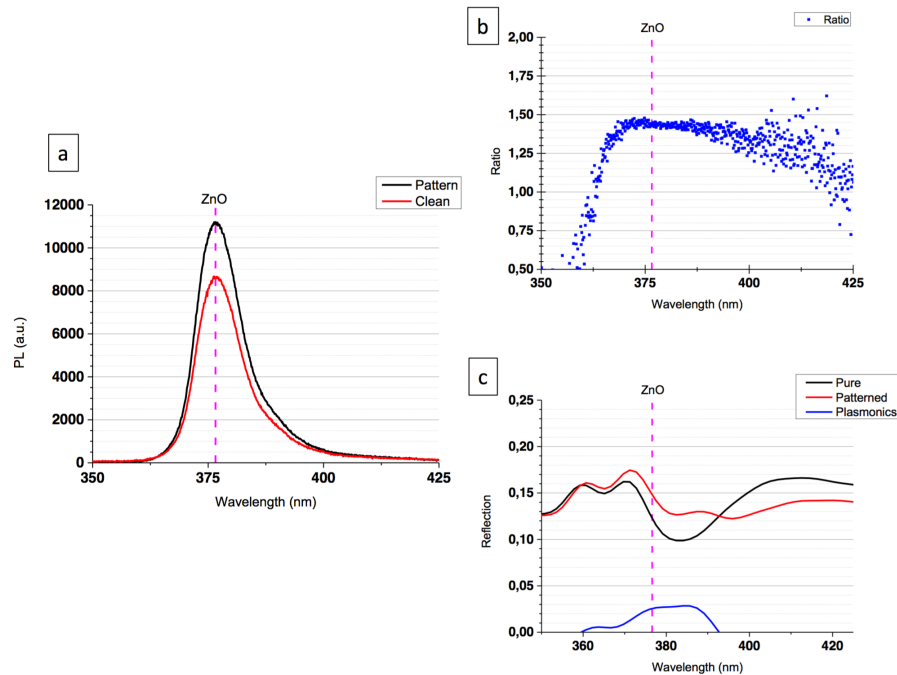


FIGURE B.12: (a) Spectres de photo-luminescence mesurés sur une couche fine de ZnO dans une zone contenant des nano-cylindres d'aluminium (spectre noir) et sans nano-cylindres (spectre rouge). (b) Facteur d'exaltation de photo-luminescence entre les zones avec et sans nano-cylindres d'aluminium. (c) Spectres de réflexion calculés par FDTD.

fractales sont fabriquées par lithographie électronique. Nous montrons également que pour certaines géométries, ces structures possèdent une réponse optique chirale droite ou gauche, à la fois dans le visible et l'ultraviolet proche.

Sur la figure B.13 sont présentés des résultats obtenus sur une structure fractale de type "Cayley Tree" (arbre de Cayley). L'encart (a) montre la structure lithographiée avec 3 générations successives de branches dans l'arbre. La première branche a une longueur de 105 nm, la seconde 100 nm et la troisième 80 nm. Toutes ont une largeur de 60 nm. Les spectres d'extinction expérimentaux et calculés sont en bon accord (encart b). Ces derniers montrent que les structures fractales possèdent des résonances plasmoniques allant du bleu (400 nm) au rouge (700 nm). Des calculs FDTD des champs proches pour une longueur d'onde de 610 nm sont donnés dans les encarts (c) et (d) pour deux états de polarisation de l'onde incidente le long des deux axes principaux de symétrie. A cette longueur, d'onde, on peut noter que le champ est concentré de manière inhomogène, uniquement au niveau de certaines branches.

Comme il est expliqué dans ce manuscrit de thèse, le dichroïsme circulaire est une quantité macroscopique obtenue à partir de mesures en champ lointain. Pour quantifier la chiralité à l'intérieur des nanostructures, il faut définir une quantité pour le champ proche, rendant compte des effets *locaux* de chiralité, autrement dit dans le champ proche des nanostructures. Une telle quantité a été définie récemment dans les travaux de Govorov et al., 2011 et s'appelle la *Chiralité optique* (ou densité optique de chiralité). Cette quantité représente les effets locaux d'amplification chirale apparaissant dans les nanostructures plasmoniques. La

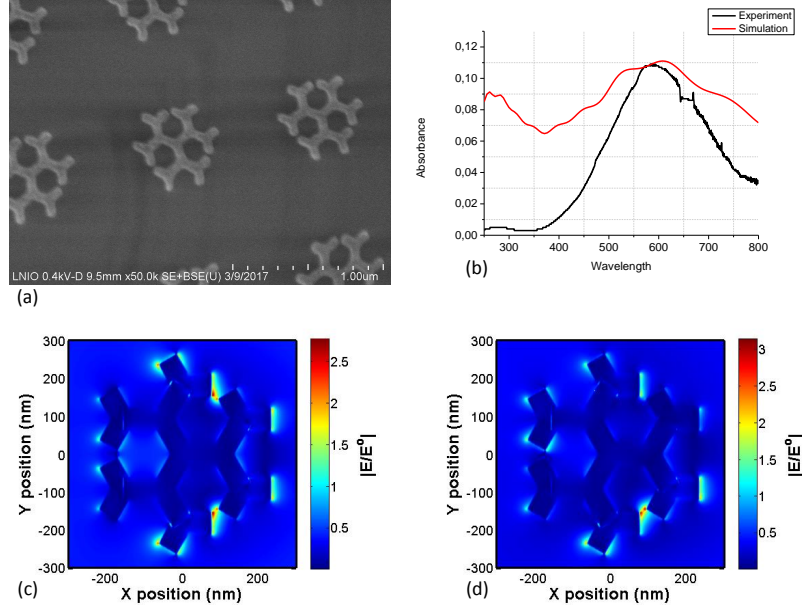


FIGURE B.13: (a) Image MEB d'une structure fractale en aluminium avec 3 générations successives de branches ($l_1 = 105$ nm, $l_2 = 100$ nm, $l_3 = 80$ nm, w (largeur) = 60). (b) Spectres d'extinction expérimentaux (noir) et calculés par FDTD (rouge). (c) Cartographie du champ proche électrique calculé par FDTD pour la longueur d'onde optimale (610 nm, maximum de la résonance) pour deux polarisations de la lumière incidente le long des axes principaux de symétrie.

chiralité optique peut s'écrire sous la forme suivante:

$$C(\vec{r}) = \frac{1}{2} [\epsilon_0 \vec{E}(\vec{r}) \cdot \vec{\nabla} \times \vec{E}(\vec{r}) + \frac{1}{\mu_0} \vec{B}(\vec{r}) \cdot \vec{\nabla} \times \vec{B}(\vec{r})] \quad (\text{B.1})$$

où \vec{E} et \vec{B} sont les champs électrique et magnétique, respectivement. Dans le cas de champs harmoniques, une version simplifiée peut s'écrire:

$$C(\vec{r}) = -\frac{\epsilon_0 \omega}{2} \text{Im}[\vec{E}^*(\vec{r}) \cdot \vec{B}(\vec{r})] \quad (\text{B.2})$$

où \vec{E} et \vec{B} sont les amplitudes des champs complexes. Afin d'obtenir des nombres plus pratiques à utiliser, il est commode de normaliser cette valeur en utilisant la chiralité d'une onde à polarisation circulaire comme référence. Ceci définit le *facteur d'exaltation chirale optique*, qui est représenté par la formule:

$$\hat{C}(\vec{r}) = \frac{C^\pm}{|C_{CPL}^\pm|} \quad (\text{B.3})$$

où \pm représente les polarisations circulaires droite et gauche et C_{CPL}^\pm la chiralité sans nanostructures. Pour une lumière non polarisée $\hat{C} = 0$ et pour une lumière polarisée circulairement $\hat{C} = 1$. Les champs avec $\hat{C} > 1$ sont appelés "champs super-chiraux". Ces champs super-chiraux naissent à partir des effets locaux et, par conséquent, sont confinés dans le champ proche. Le calcul de \hat{C} a été effectué pour une structure fractale et chirale

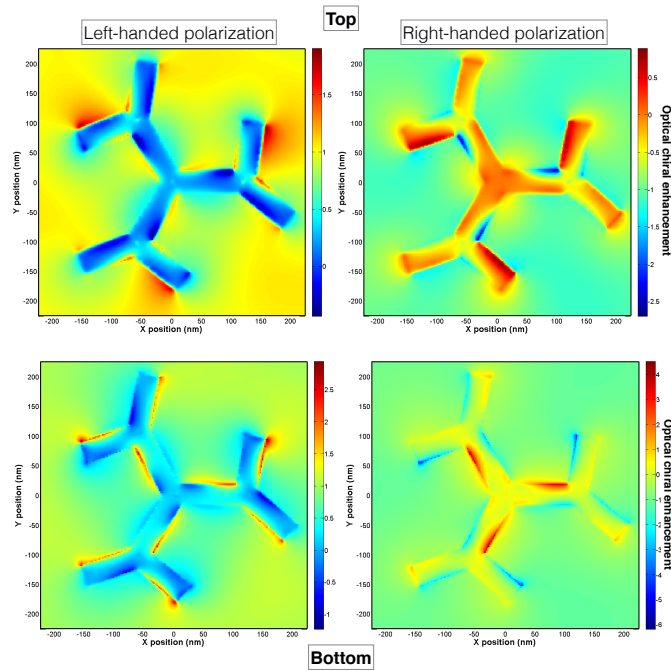


FIGURE B.14: Facteur d'exaltation chiral optique obtenu à partir de simulations FDTD pour une structure d'aluminium fractale avec deux générations de branches (longueurs $l_1 = 120$ nm, $l_2 = 100$ nm), d'épaisseur $w = 50$ nm, de hauteur $h = 40$ nm, avec une rotation $\theta = 20^\circ$ entre les deux branches. Les cartes ont été calculées à $\lambda = 450$ nm.

d'aluminium aux dimensions réalisables dont les résultats sont montrés sur la figure B.14. On remarque qu'une même structure peut présenter des propriétés chirales droite et gauche, et à des longueurs d'ondes allant de de l'ultraviolet proche au visible. Ceci est possible grâce aux propriétés plasmoniques remarquables de l'aluminium et à "l'effet Cotton", comme il est expliqué dans le manuscrit.

Ces résultats montrent que pour cette structure particulière l'amélioration chirale optique atteint des valeurs maximales de \hat{C} comprises entre -6 et 4 . Cette gamme est comparable à ce qui a été rapporté dans la gamme infrarouge en utilisant des structures en or de géométrie de type "gammadion". Une optimisation plus poussée de la structure devrait conduire à des valeurs encore plus élevées de \hat{C} . Nous discutons maintenant des résultats expérimentaux, présentés sur la figure B.15.

Cette figure présente des résultats expérimentaux sur des structures fractales avec la même configuration géométrique qui est décrite dans la figure précédente, pour les calculs théoriques. La différence entre les spectres d'extinction lorsque la lumière incidente est polarisée circulaire droite ou gauche est visible, particulièrement dans le visible, aux alentours de 700 nm. Dans le proche ultraviolet les résultats sont moins marqués. Toutefois, d'autres résultats discutés dans le manuscrit montrent clairement que du dichroïsme circulaire peut également être créé à ces longueurs d'onde.

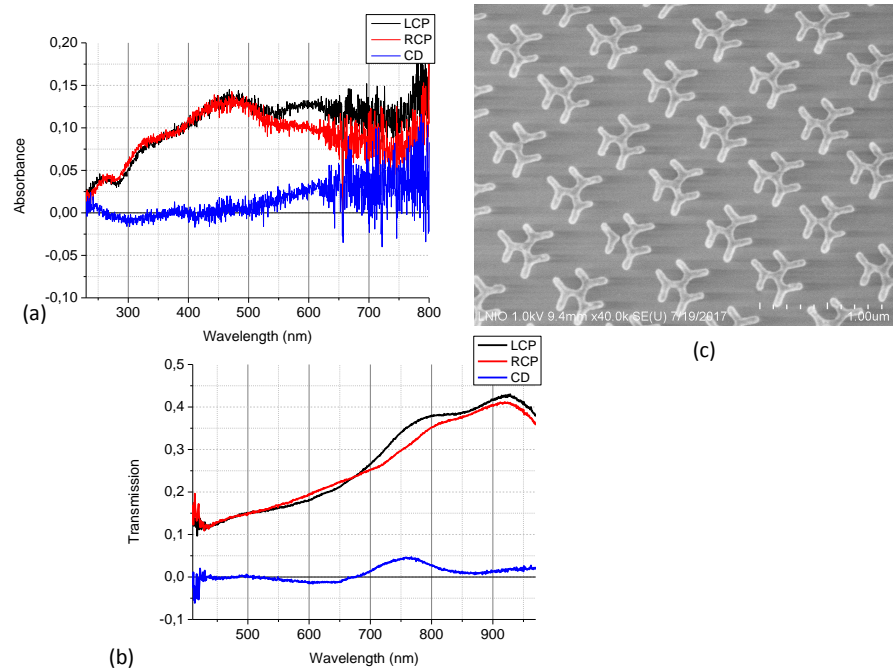


FIGURE B.15: (a) Spectres d’extinction obtenus sur un réseau contenant des structures chirales d’aluminium avec la géométrie décrite sur la figure précédente. Rouge : polarisation incidente circulaire droite; noir: polarisation incidente circulaire gauche; bleu: dichroïsme circulaire calculé. (b) Mêmes mesures dans la visible. (c) Image MEB du réseau de structures chirales.

B.5 Conclusion

Le but principal de cette thèse était de mettre au point des méthodes efficaces basées sur la plasmonique à base d’aluminium pour des applications optiques. Par exemple, nous nous sommes intéressés au couplage de la plasmonique aluminium avec les semi-conducteurs à large bande interdite afin d’exalter ou de contrôler la luminescence de ces derniers.

Dans le chapitre 1, il est montré que l’utilisation de l’aluminium pour la plasmonique présente plusieurs avantages : l’aluminium est un matériau peu coûteux qui possède des propriétés plasmoniques sur une large gamme spectrale, de l’ultraviolet (80 nm théoriquement) à l’infrarouge. Quelques inconvénients dont nous avons également discuté sont les pertes élevées dans la partie visible, à cause d’une partie imaginaire élevée de la permittivité diélectrique dues aux transitions interbandes autour de 800 nm. Cependant, la plasmonique à base d’aluminium est un domaine en pleine croissance avec de très nombreuses applications potentielles en nano-optique.

Pour résoudre le problème du faible facteur de qualité des résonances plasmoniques dans le domaine visible, nous avons proposé dans le chapitre 2 une méthode basée sur le couplage des résonances avec les modes de réseau. Une étude systématique conséquente a été réalisée comprenant tous les aspects : explication théorique, simulation FDTD et investigation expérimentale. Avec un réseau de nano-cylindres d’aluminium avec les dimensions optimales, nous avons atteint des facteurs de qualité $Q \approx 13$. Cette valeur est de 5 à 10 fois

plus élevée que pour les nanoparticules d'aluminium isolées. Ces résultats ont également été démontrés dans le proche ultraviolet.

Dans le chapitre 3, les structures plasmoniques en aluminium sont utilisées dans le but d'améliorer l'émission de lumière de matériaux semi-conducteurs à large bande interdite, l'oxyde de zinc dans notre cas. Nous avons intégré des nanostructures d'aluminium sur la surface d'une couche mince de ZnO. Des simulations FDTD ont été réalisées pour concevoir et étudier les structures hybrides. Les résultats expérimentaux présentés dans ce chapitre ont montré que de telles structures peuvent aboutir à un facteur d'exaltation de la photoluminescence du ZnO de 30.

Le problème que nous avons rencontré dans le chapitre 3, c'est-à-dire l'absence de profondeur de pénétration des effets plasmoniques au sein de la couche active, nous a poussés à rechercher des structures avec des extensions spatiales du champ électrique plus élevées. En nous inspirant des technologies développées dans le domaine des radiofréquences, nous avons adapté les structures fractales à la gamme optique avec l'aluminium. Une structure fractale simple, l'arbre de Cayley, a été utilisée pour démontrer l'efficacité de la géométrie fractale. Les simulations numériques sur les arbres de Cayley et les cylindres en aluminium ont montré qu'en l'absence d'effets collectifs, les structures fractales ont des valeurs plus élevées que les cylindres en termes de champ électrique moyen par unité de surface.

De plus, au cours de l'étude nous avons proposé un modèle de fractale chirale. En combinant la géométrie chirale avec la géométrie fractale, nous avons démontré la possibilité d'obtenir une réponse optique chirale des nanostructures dans la partie proche UV et visible du spectre. Les nombreux degrés de liberté inhérents à la géométrie des structures fractales permettent d'obtenir des propriétés chirales droite et gauche au sein d'une même structure. Les simulations numériques prouvent la présence d'un dichroïsme circulaire et d'une amélioration de la chiralité optique locale dans les fractales d'aluminium avec les bonnes dimensions. Les expérimentations effectuées sur des fractales chirales d'aluminium fabriquées par lithographie électronique ont montré la présence de dichroïsme dans l'ultraviolet proche et le visible.

Les fractales possédant une géométrie complexe, leurs propriétés plasmoniques peuvent être optimisées en vue de différentes applications :

1. L'utilisation de fractales d'aluminium couplées avec un semi-conducteur à large bande interdite devrait permettre de polariser circulairement et de contrôler la luminescence de ce dernier. Les applications potentielles en nano-optique/photonique sont dès lors très nombreuses.
2. En outre, les structures fractales peut être utilisées pour augmenter la luminescence d'émetteurs quantiques ou de molécules fluorescentes diverses.
3. De plus, les fractales d'aluminium peuvent être utilisées pour le SERS, de l'ultraviolet à l'infrarouge.

Il est important de noter que la géométrie complexe des fractales impose un processus de fabrication complexe. Cette procédure nécessite encore des améliorations pour obtenir une

meilleure reproductibilité des nanostructures lithographiées. Avec l'utilisation de résines de pointe, il sera possible d'obtenir des fractales de grande qualité aux bords parfaitement définis. Ceci est particulièrement important pour les fractales chirales où la géométrie joue un rôle crucial.

Une autre application des fractales chirales est la détection de molécules, où la chiralité aide à distinguer les différents énantiomères. De même, des sources lumineuses avec une polarisation circulaire accordable peuvent être créées sur la base de ces structures. Ces sources pourraient être intéressantes dans l'industrie des écrans 3D. Toujours à propos des écrans, il est également très important de mentionner le modèle "cellule chaude" discuté au chapitre 4. Les arbres de Cayley à 4 branches peuvent fonctionner comme un commutateur optique commandé par la polarisation.

Plus généralement, la plasmonique à base d'aluminium est un domaine de recherche encore récent et donc en développement. La nano-optique UV (et visible) assistée et contrôlée par la plasmonique est un domaine de plus en plus important, avec énormément d'applications potentielles. Dans un futur proche, la plasmonique à base d'aluminium pourrait devenir une thématique phare dans la communauté.

Bibliography

- Aad, R. et al. (2014). "Efficient Pump Photon Recycling via Gain-Assisted Waveguiding Energy Transfer". In: *ACS Photonics* 1.3, pp. 246–253. ISSN: 23304022. DOI: [10.1021/ph4001179](https://doi.org/10.1021/ph4001179).
- Abdellaoui, N. et al. (2015). "Plasmonic enhancement of Eu:Y2O3 luminescence by Al percolated layer." In: *Nanotechnology* 26.9, p. 095701. ISSN: 1361-6528. DOI: [10.1088/0957-4484/26/9/095701](https://doi.org/10.1088/0957-4484/26/9/095701).
- Amano, H. et al. (1989). "P-type conduction in Mg-doped GaN treated with low-energy electron beam irradiation (LEEBI)". In: *Japanese Journal of Applied Physics* 28.12 A, pp. L2112–L2114. ISSN: 13474065. DOI: [10.1143/JJAP.28.L2112](https://doi.org/10.1143/JJAP.28.L2112).
- Aouani, H. et al. (2013). "Plasmonic nanoantennas for multispectral surface-enhanced spectroscopies". In: *Journal of Physical Chemistry C* 117.36, pp. 18620–18626. ISSN: 19327447. DOI: [10.1021/jp404535x](https://doi.org/10.1021/jp404535x).
- Arenal, R. et al. (2005). "Electron energy loss spectroscopy measurement of the optical gaps on individual boron nitride single-walled and multiwalled nanotubes". In: *Physical Review Letters* 95.12. ISSN: 00319007. DOI: [10.1103/PhysRevLett.95.127601](https://doi.org/10.1103/PhysRevLett.95.127601).
- Bachelot, R. and Plain, J. (2013). "Near field imaging of complex metal nanostructures based on the use of azobenzene nanomotors". In: Figure 2, pp. 2–3. DOI: [10.1021/jz400586y](https://doi.org/10.1021/jz400586y).
- Bartlett, P. N. et al. (2004). *Optical properties of nanostructured metal films*. Vol. 125, p. 117. ISBN: 1364-5498. DOI: [10.1039/b304116f](https://doi.org/10.1039/b304116f). URL: <http://xlink.rsc.org/?DOI=b304116f>.
- Beddard, T. *Sub.Blue*. URL: <http://2008.sub.blue/projects/mandelbulb.html>.
- Boardman, A. D. and Zayats, A. V. (2014). "Nonlinear plasmonics". In: *Handbook of Surface Science* 4.11, pp. 329–347. ISSN: 15734331. DOI: [10.1016/B978-0-444-59526-3.00011-2](https://doi.org/10.1016/B978-0-444-59526-3.00011-2).
- Bohm, D. (1952). "A suggested interpretation of the quantum theory in terms of "hidden" variables. I". In: *Physical Review* 85.2, pp. 166–179. ISSN: 0031899X. DOI: [10.1103/PhysRev.85.166](https://doi.org/10.1103/PhysRev.85.166).
- Boltasseva, A. and Atwater, H. A. (2011). "Low-Loss Plasmonic Metamaterials". In: *Science* 331.6015, pp. 290–291. ISSN: 0036-8075. DOI: [10.1126/science.1198258](https://doi.org/10.1126/science.1198258).
- Bourrellier, R. et al. (2014). "Nanometric Resolved Luminescence in h-BN Flakes: Excitons and Stacking Order". In: *ACS Photonics* 1.9, pp. 857–862. ISSN: 23304022. DOI: [10.1021/ph500141j](https://doi.org/10.1021/ph500141j).
- Cakmakyapan, S. et al. (2014). "Validation of electromagnetic field enhancement in near-infrared through Sierpinski fractal nanoantennas". In: *Optics Express* 22.16, p. 19504. ISSN: 1094-4087. DOI: [10.1364/OE.22.019504](https://doi.org/10.1364/OE.22.019504).

- Cameron, R. P., Götze, J. B., and Barnett, S. M. (2016). "Chiral rotational spectroscopy". In: *Physical Review A* 94.3. ISSN: 24699934. DOI: [10.1103/PhysRevA.94.032505](https://doi.org/10.1103/PhysRevA.94.032505).
- Cassabois, G., Valvin, P., and Gil, B. (2015). "Hexagonal boron nitride is an indirect bandgap semiconductor". In: *Nature Photonics* January. ISSN: 1749-4885. DOI: [10.1038/nphoton.2015.277](https://doi.org/10.1038/nphoton.2015.277).
- Castro-lopez, M. et al. (2008). "Polarized multiphoton emission from resonant Al, Ag and Au nanoantennas". In: *Nano Lett.* 9.1, p. 116805.
- Catchpole, K. R. and Polman, A. (2008). "Plasmonic solar cells". In: *Optics Express* 16.26, p. 21793. ISSN: 1094-4087. DOI: [10.1364/OE.16.021793](https://doi.org/10.1364/OE.16.021793).
- Cayley, A. (1878). "A theorem on groups". In: *Mathematische Annalen* 13.4, pp. 561–565. ISSN: 00255831. DOI: [10.1007/BF01444354](https://doi.org/10.1007/BF01444354).
- Cheng, P. et al. (2009). "Localized surface plasmon enhanced photoluminescence from ZnO films: Extraction direction and emitting layer thickness". In: *Journal of Applied Physics* 106.6, pp. 1–5. ISSN: 00218979. DOI: [10.1063/1.3225094](https://doi.org/10.1063/1.3225094).
- Chou, Y. H. et al. (2015). "Ultrastrong Mode Confinement in ZnO Surface Plasmon Nanolasers". In: *ACS Nano* 9.4, pp. 3978–3983. ISSN: 1936086X. DOI: [10.1021/acsnano.5b01643](https://doi.org/10.1021/acsnano.5b01643).
- Class for Physics of the Royal Swedish Academy of Sciences (2014). "Efficient blue light-emitting diodes leading to bright and energy-saving white light sources". In: *Scientific Background on the Nobel Prize in Physics 2014* 50005, pp. 1–9. URL: http://www.nobelprize.org/nobel/_prizes/physics/laureates/2014/.
- Colas des Francs, G et al. (2016). "Plasmonic Purcell factor and coupling efficiency to surface plasmons. Implications for addressing and controlling optical nanosources". In: *Journal of Optics* 18.9, p. 094005. ISSN: 2040-8978. DOI: [10.1088/2040-8978/18/9/094005](https://doi.org/10.1088/2040-8978/18/9/094005).
- Database, I. I. URL: <http://www.ioffe.ru/SVA/NSM/Semicond/>.
- De Oñate, J. J. *Fractal antenna experiment*. URL: http://www.m0wwa.co.uk/page/M0WWA_fractal_antenna.html.
- Di Carlo, A. (2001). "Tuning optical properties of GaN-based nanostructures by charge screening". In: *Physica Status Solidi (A) Applied Research* 183.1, pp. 81–85. ISSN: 00318965. DOI: [10.1002/1521-396X\(200101\)183:1<81::AID-PSSA81>3.0.CO;2-N](https://doi.org/10.1002/1521-396X(200101)183:1<81::AID-PSSA81>3.0.CO;2-N).
- Divay, L. et al. (2008). "Studies of optical emission in the high intensity pumping regime of top-down ZnO nanostructures and thin films grown on c-sapphire substrates by pulsed laser deposition". In: *Physica Status Solidi (C) Current Topics in Solid State Physics* 5.9, pp. 3095–3097. ISSN: 18626351. DOI: [10.1002/pssc.200779298](https://doi.org/10.1002/pssc.200779298).
- Dong, J. et al. (2014). "Simultaneous SEF and SERRS from silver fractal-like nanostructure". In: *Sensors and Actuators, B: Chemical* 191, pp. 595–599. ISSN: 09254005. DOI: [10.1016/j.snb.2013.09.088](https://doi.org/10.1016/j.snb.2013.09.088).
- Drude, P. (1900). "Zur Elektronentheorie der Metalle; II. Teil. Galvanomagnetische und thermomagnetische Effecte". In: *Annalen der Physik* 308.11, pp. 369–402. ISSN: 15213889. DOI: [10.1002/andp.19003081102](https://doi.org/10.1002/andp.19003081102).
- Ebbesen, T. W. et al. (1998). "Extraordinary optical transmission through sub-wavelength hole arrays". In: *Nature* 391.6668, pp. 667–669. DOI: [10.1038/35570](https://doi.org/10.1038/35570).

- Ehrenreich, H., Philipp, H. R., and Segall, B. (1963). "Optical properties of aluminum". In: *Physical Review* 132.5, pp. 1918–1928. ISSN: 0031899X. DOI: [10.1103/PhysRev.132.1918](https://doi.org/10.1103/PhysRev.132.1918).
- Eid, J. et al. (2009). "Real-Time DNA Sequencing from Single Polymerase Molecules". In: *Science* 323.5910, pp. 133–138. ISSN: 0036-8075. DOI: [10.1126/science.1162986](https://doi.org/10.1126/science.1162986).
- Elser, J. et al. (2006). "Nanowire metamaterials with extreme optical anisotropy". In: *Applied Physics Letters* 89.26. ISSN: 00036951. DOI: [10.1063/1.2422893](https://doi.org/10.1063/1.2422893).
- Fan, Z. and Govorov, A. O. (2010). "Plasmonic circular dichroism of chiral metal nanoparticle assemblies". In: *Nano Letters* 10.7, pp. 2580–2587. ISSN: 15306984. DOI: [10.1021/nl101231b](https://doi.org/10.1021/nl101231b).
- Fano, U. (1941). "The Theory of Anomalous Diffraction Gratings and of Quasi-Stationary Waves on Metallic Surfaces (Sommerfeld's Waves)". In: *Journal of the Optical Society of America* 31.3, p. 213. ISSN: 0030-3941. DOI: [10.1364/JOSA.31.000213](https://doi.org/10.1364/JOSA.31.000213).
- Freestone, I. et al. (2007). "The Lycurgus Cup — A Roman nanotechnology". In: *Gold Bulletin* 40.4, pp. 270–277. ISSN: 0017-1557. DOI: [10.1007/BF03215599](https://doi.org/10.1007/BF03215599).
- Gall, D. (2016). "Electron mean free path in elemental metals". In: *Journal of Applied Physics* 119.8, pp. 1–5. ISSN: 10897550. DOI: [10.1063/1.4942216](https://doi.org/10.1063/1.4942216).
- Gao, N. et al. (2012). "Surface-plasmon-enhanced deep-UV light emitting diodes based on AlGaN multi-quantum wells". In: *Scientific Reports* 2.1, p. 816. ISSN: 2045-2322. DOI: [10.1038/srep00816](https://doi.org/10.1038/srep00816).
- Gérard, D. and Gray, S. K. (2015). "Aluminium plasmonics". In: *Journal of Physics D: Applied Physics* 48.18, p. 184001. ISSN: 0022-3727. DOI: [10.1088/0022-3727/48/18/184001](https://doi.org/10.1088/0022-3727/48/18/184001).
- Giannini, V. et al. (2011). "Fano resonances in nanoscale plasmonic systems: A parameter-free modeling approach". In: *Nano Letters* 11.7, pp. 2835–2840. ISSN: 15306984. DOI: [10.1021/nl201207n](https://doi.org/10.1021/nl201207n).
- Gokarna, A. et al. (2014). "Highly crystalline urchin-like structures made of ultra-thin zinc oxide nanowires". In: *RSC Adv.* 4.88, pp. 47234–47239. ISSN: 2046-2069. DOI: [10.1039/C4RA06327A](https://doi.org/10.1039/C4RA06327A).
- Gottheim, S. et al. (2015). "Fractal nanoparticle plasmonics: The cayley tree". In: *ACS Nano* 9.3, pp. 3284–3292. ISSN: 1936086X. DOI: [10.1021/acs.nano.5b00412](https://doi.org/10.1021/acs.nano.5b00412).
- Govorov, A. O. et al. (2011). "Chiral nanoparticle assemblies: circular dichroism, plasmonic interactions, and exciton effects". In: *Journal of Materials Chemistry* 21.42, p. 16806. ISSN: 0959-9428. DOI: [10.1039/c1jm12345a](https://doi.org/10.1039/c1jm12345a).
- Greenfield, N. J. (2006). "Using circular dichroism spectra to estimate protein secondary structure." In: *Nature protocols* 1.6, pp. 2876–90. ISSN: 1750-2799. DOI: [10.1038/nprot.2006.202](https://doi.org/10.1038/nprot.2006.202). URL: <http://www.ncbi.nlm.nih.gov/pubmed/17406547>{\% }5Cn<http://www.pubmedcentral.nih.gov/articlerender.fcgi?artid=PMC2728378>.
- Gryczynski, I. et al. (2004). "Ultraviolet surface plasmon-coupled emission using thin aluminum films". In: *Analytical Chemistry* 76.14, pp. 4076–4081. ISSN: 00032700. DOI: [10.1021/ac040004c](https://doi.org/10.1021/ac040004c).

- Guerrero-Martínez, A. et al. (2011). *From individual to collective chirality in metal nanoparticles*. DOI: [10.1016/j.nantod.2011.06.003](https://doi.org/10.1016/j.nantod.2011.06.003).
- Hendry, E. et al. (2012). "Chiral electromagnetic fields generated by arrays of nanoslits". In: *Nano Letters* 12.7, pp. 3640–3644. ISSN: 15306984. DOI: [10.1021/nl3012787](https://doi.org/10.1021/nl3012787).
- Honda, M. et al. (2014). "Plasmon-enhanced UV photocatalysis". In: *Applied Physics Letters* 104.6, p. 61108. ISSN: 00036951. DOI: [10.1063/1.4864395](https://doi.org/10.1063/1.4864395).
- Hou, C. et al. (2014). "Ag-nanoparticle-decorated Au-fractal patterns on bowl-like-dimple arrays on Al foil as an effective SERS substrate for the rapid detection of PCBs". In: *Chem. Commun.* 50.5, pp. 569–571. ISSN: 1359-7345. DOI: [10.1039/C3CC46878J](https://doi.org/10.1039/C3CC46878J).
- Hubert, C. et al. (2008). "Near-field polarization effects in molecular-motion-induced photochemical imaging". In: *Journal of Physical Chemistry C* 112.11, pp. 4111–4116. ISSN: 19327447. DOI: [10.1021/jp7096263](https://doi.org/10.1021/jp7096263).
- Jackson, J. D. and Fox, R. F. (1999). *Classical Electrodynamics, 3rd ed*. DOI: [10.1119/1.19136](https://doi.org/10.1119/1.19136).
- Jaffrennou, P. et al. (2007). "Cathodoluminescence imaging and spectroscopy on a single multiwall boron nitride nanotube". In: *Chemical Physics Letters* 442.4-6, pp. 372–375. ISSN: 00092614. DOI: [10.1016/j.cplett.2007.06.001](https://doi.org/10.1016/j.cplett.2007.06.001).
- Jaffrennou, P. et al. (2008). "Near-band-edge recombinations in multiwalled boron nitride nanotubes: Cathodoluminescence and photoluminescence spectroscopy measurements". In: *Physical Review B - Condensed Matter and Materials Physics* 77.23. ISSN: 10980121. DOI: [10.1103/PhysRevB.77.235422](https://doi.org/10.1103/PhysRevB.77.235422).
- Kelvin, W. T. (1894). "The molecular tactics of a crystal". In: *Clarendon Press*, p. 65. URL: <http://archive.org/details/moleculartactic00kelvgoog/%5Cnfiles/1426/Kelvin-1894-Themoleculartacticsofacrystal.pdf>.
- Khlopin, D. et al. (2017). "Lattice modes and plasmonic linewidth engineering in gold and aluminum nanoparticle arrays". In: *Journal of the Optical Society of America B* 34.3, p. 691. ISSN: 0740-3224. DOI: [10.1364/JOSAB.34.000691](https://doi.org/10.1364/JOSAB.34.000691).
- Khorrami, M. and Aghamohammadi, A. (2014). "Autonomous models on a Cayley tree". In: *Journal of Statistical Mechanics: Theory and Experiment* 2014.7, P07017. ISSN: 1742-5468. DOI: [10.1088/1742-5468/2014/07/P07017](https://doi.org/10.1088/1742-5468/2014/07/P07017).
- Kildishev, A. V., Boltasseva, A., and Shalaev, V. M. (2013). "Planar Photonics with Metasurfaces". In: *Science* 339.6125, pp. 1232009–1232009. ISSN: 0036-8075. DOI: [10.1126/science.1232009](https://doi.org/10.1126/science.1232009).
- Klimov, V. (2014). *Nanoplasmonics*. Pan Stanford Publishing. ISBN: 9789814267427. URL: <https://books.google.fr/books?id=KqfSBQAAQBAJ>.
- Knight, M. W. et al. (2014). "Aluminum for plasmonics". In: *ACS Nano* 8.1, pp. 834–840. ISSN: 19360851. DOI: [10.1021/nn405495q](https://doi.org/10.1021/nn405495q).
- Krause, D., Teplin, C. W., and Rogers, C. T. (2004). "Optical surface second harmonic measurements of Isotropic thin-film metals: Gold, silver, copper, aluminum, and tantalum". In: *Journal of Applied Physics* 96.7, pp. 3626–3634. ISSN: 00218979. DOI: [10.1063/1.1786341](https://doi.org/10.1063/1.1786341).

- Kumar, K. et al. (2012). "Printing colour at the optical diffraction limit". In: *Nature Nanotechnology* 7.9, pp. 557–561. ISSN: 1748-3387. DOI: [10.1038/nnano.2012.128](https://doi.org/10.1038/nnano.2012.128).
- Kunz, J. N. et al. (2017). "Aluminum plasmonic nanoshielding in ultraviolet inactivation of bacteria". In: *Scientific Reports* 7.1, p. 9026. ISSN: 2045-2322. DOI: [10.1038/s41598-017-08593-8](https://doi.org/10.1038/s41598-017-08593-8).
- Langhammer, C. et al. (2008a). "Localized surface plasmon resonances in aluminum nanodisks". In: *Nano Letters* 8.5, pp. 1461–1471. ISSN: 15306984. DOI: [10.1021/nl080453i](https://doi.org/10.1021/nl080453i).
- (2008b). "Localized surface plasmon resonances in aluminum nanodisks". In: *Nano Letters* 8.5, pp. 1461–1471. ISSN: 15306984. DOI: [10.1021/nl080453i](https://doi.org/10.1021/nl080453i).
- Larach, S. and Shrader, R. E. (1956). "Multiband luminescence in boron nitride". In: *Physical Review* 104.1, pp. 68–73. ISSN: 0031899X. DOI: [10.1103/PhysRev.104.68](https://doi.org/10.1103/PhysRev.104.68).
- Laroche, T., Vial, A., and Roussey, M. (2007). "Crystalline structure's influence on the near-field optical properties of single plasmonic nanowires". In: *Applied Physics Letters* 91.12. ISSN: 00036951. DOI: [10.1063/1.2784389](https://doi.org/10.1063/1.2784389).
- Laux, F., Bonod, N., and Gérard, D. (2017). "Single Emitter Fluorescence Enhancement with Surface Lattice Resonances". In: *Journal of Physical Chemistry C* 121.24, pp. 13280–13289. ISSN: 19327455. DOI: [10.1021/acs.jpcc.7b04207](https://doi.org/10.1021/acs.jpcc.7b04207).
- Levinson, H. J., Greuter, F., and Plummer, E. W. (1983). "Experimental band structure of aluminum". In: *Physical Review B* 27.2, pp. 727–747. ISSN: 01631829. DOI: [10.1103/PhysRevB.27.727](https://doi.org/10.1103/PhysRevB.27.727).
- Liu, Y. et al. (2015). "A plasmonic gold nanostar theranostic probe for in vivo tumor imaging and photothermal therapy". In: *Theranostics* 5.9, pp. 946–960. ISSN: 18387640. DOI: [10.7150/thno.11974](https://doi.org/10.7150/thno.11974).
- Lord, H. L., Zhan, W., and Pawliszyn, J. (2012). *Fundamentals and applications of needle trap devices*. Vol. 2. 1. Springer Science+BusinessMedia LLC, pp. 677–697. ISBN: 9780123813749. DOI: [10.1016/B978-0-12-381373-2.00056-9](https://doi.org/10.1016/B978-0-12-381373-2.00056-9).
- Lu, Y.-J. et al. (2012). "Plasmonic Nanolaser Using Epitaxially Grown Silver Film". In: *Science* 337.6093, pp. 450–453. ISSN: 0036-8075. DOI: [10.1126/science.1223504](https://doi.org/10.1126/science.1223504).
- Lumerical. URL: <https://optiwave.com/optifdtd-overview/>.
- Maidecchi, G. et al. (2013). "Deep ultraviolet plasmon resonance in aluminum nanoparticle arrays". In: *ACS Nano* 7.7, pp. 5834–5841. ISSN: 19360851. DOI: [10.1021/nn400918n](https://doi.org/10.1021/nn400918n).
- Maier, S. A. (2007). *Plasmonics: Fundamentals and applications*, pp. 1–223. ISBN: 0387331506. DOI: [10.1007/0-387-37825-1](https://doi.org/10.1007/0-387-37825-1).
- Mandelbrot, B. (1983). *The Fractal Geometry of Nature*. Vol. 51. 3. New York: W. H. FREEMAN and COMPANY, p. 286. ISBN: 9788578110796. DOI: [10.1017/CBO9781107415324.004](https://doi.org/10.1017/CBO9781107415324.004). URL: <http://link.aip.org/link/?AJP/51/286/1{\&}Agg=doi>.
- Martin, J. and Plain, J. (2015). "Fabrication of aluminium nanostructures for plasmonics". In: *Journal of Physics D: Applied Physics* 48.18, p. 184002. ISSN: 0022-3727. DOI: [10.1088/0022-3727/48/18/184002](https://doi.org/10.1088/0022-3727/48/18/184002).
- Martin, J. et al. (2014). "High-resolution imaging and spectroscopy of multipolar plasmonic resonances in aluminum nanoantennas". In: *Nano Letters* 14.10, pp. 5517–5523. ISSN: 15306992. DOI: [10.1021/nl501850m](https://doi.org/10.1021/nl501850m).

- Mastroianni, A. J., C., S. A., and Paul Alivisatos, A. (2009). "Pyramidal and chiral groupings of gold nanocrystals assembled using DNA scaffolds". In: *Journal of the American Chemical Society* 131.24, pp. 8455–8459. ISSN: 00027863. DOI: [10.1021/ja808570g](https://doi.org/10.1021/ja808570g).
- Maystre, D. (2012). *Plasmonics*. Vol. 167. ISBN: 978-3-642-28078-8. DOI: [10.1007/978-3-642-28079-5](https://doi.org/10.1007/978-3-642-28079-5). URL: <http://link.springer.com/10.1007/978-3-642-28079-5>.
- Melentiev, P. N. et al. (2013). "Single nano-hole as a new effective nonlinear element for third-harmonic generation". In: *Laser Physics Letters* 10.7, p. 075901. ISSN: 1612-2011. DOI: [10.1088/1612-2011/10/7/075901](https://doi.org/10.1088/1612-2011/10/7/075901).
- Mie, G. (1908). "Beiträge zur Optik trüber Medien, speziell kolloidaler Metallösungen". In: *Annalen der Physik* 330.3, pp. 377–445. ISSN: 15213889. DOI: [10.1002/andp.19083300302](https://doi.org/10.1002/andp.19083300302). URL: <http://dx.doi.org/10.1002/andp.19083300302>.
- Morkoç, H. et al. (1994). "Large-band-gap SiC, III-V nitride, and II-VI ZnSe-based semiconductor device technologies". In: *Journal of Applied Physics* 76.3, pp. 1363–1398. ISSN: 00218979. DOI: [10.1063/1.358463](https://doi.org/10.1063/1.358463).
Nanovation. URL: <http://nanovation.com/fr/>.
- Navarro-Cia, M. and Maier, S. A. (2012). "Broad-band near-infrared plasmonic nanoantennas for higher harmonic generation". In: *ACS Nano* 6.4, pp. 3537–3544. ISSN: 19360851. DOI: [10.1021/nn300565x](https://doi.org/10.1021/nn300565x).
- Nomenyo, K. et al. (2014). "Enhanced stimulated emission in ZnO thin films using microdisk top-down structuring". In: *Applied Physics Letters* 104.18. ISSN: 00036951. DOI: [10.1063/1.4875744](https://doi.org/10.1063/1.4875744).
- Nomenyo, K. D. (2014). "Photonique UV : structuration top-down du ZnO pour une émission amplifiée et un transfert d'énergie efficace". PhD thesis. URL: <http://www.theses.fr/2014TROY0023/document>.
- Norek, M., Łuka, G., and Włodarski, M. (2016). "Plasmonic enhancement of UV emission from ZnO thin films induced by Al nano-concave arrays". In: *Applied Surface Science* 384, pp. 18–26. ISSN: 01694332. DOI: [10.1016/j.apsusc.2016.05.029](https://doi.org/10.1016/j.apsusc.2016.05.029).
- Okamoto, K. et al. (2004). "Surface-plasmon-enhanced light emitters based on InGaN quantum wells". In: *Nature Materials* 3.9, pp. 601–605. ISSN: 1476-1122. DOI: [10.1038/nmat1198](https://doi.org/10.1038/nmat1198).
- Olson, J. et al. (2014). "Vivid, full-color aluminum plasmonic pixels". In: *Proceedings of the National Academy of Sciences* 111.40, pp. 14348–14353. ISSN: 0027-8424. DOI: [10.1073/pnas.1415970111](https://doi.org/10.1073/pnas.1415970111).
Optiwave. URL: <https://optiwave.com/optifdtd-overview/>.
- Ordal, M. A. et al. (1983). "Optical properties of the metals Al, Co, Cu, Au, Fe, Pb, Ni, Pd, Pt, Ag, Ti, and W in the infrared and far infrared". In: *Applied Optics* 22.7, p. 1099. ISSN: 0003-6935. DOI: [10.1364/AO.22.001099](https://doi.org/10.1364/AO.22.001099).
- Palik, E. (1997). *Handbook of Optical Constants of Solids*. ISBN: 9780125444156. DOI: [10.1016/B978-012544415-6.50143-6](https://doi.org/10.1016/B978-012544415-6.50143-6).
- Pettinger, B. (2010). "Single-molecule surface- and tip-enhanced Raman spectroscopy". In: *Molecular Physics* 108.16, pp. 2039–2059. ISSN: 00268976. DOI: [10.1080/00268976.2010.506891](https://doi.org/10.1080/00268976.2010.506891).

- Plain, J. et al. (2014). *Procede thermo acoustique de fabrication de nanoparticules monocristallines d'aluminium*. URL: <https://www.google.com/patents/EP2808105A1?cl=fr>.
- Popov, S. (2017). "The Tangle". In: *White Paper*. ISSN: 0028-792X. URL: https://iota.org/IOTA_Whitepaper.pdf.
- Powell, C. J. and Swan, J. B. (1959). "Origin of the characteristic electron energy losses in aluminum". In: *Physical Review* 115.4, pp. 869–875. ISSN: 0031899X. DOI: [10.1103/PhysRev.115.869](https://doi.org/10.1103/PhysRev.115.869).
- Purahmad, M., Stroschio, M. A., and Dutta, M. (2012). "Photoluminescence characterization of ZnO nanowires decorated with metallic nanoparticles". In: *2012 IEEE Nanotechnology Materials and Devices Conference, IEEE NMDC 2012*, pp. 166–169. DOI: [10.1109/NMDC.2012.6527601](https://doi.org/10.1109/NMDC.2012.6527601).
- Rahbany, N. (2016). "Towards integrated optics at the nanoscale : plasmon-emitter coupling using plasmonic structures". PhD thesis.
- Rakić, A. D. (1995). "Algorithm for the determination of intrinsic optical constants of metal films: application to aluminum". In: *Applied Optics* 34.22, p. 4755. ISSN: 0003-6935. DOI: [10.1364/AO.34.004755](https://doi.org/10.1364/AO.34.004755).
- Rayleigh, L. (1907). "III. Note on the remarkable case of diffraction spectra described by Prof. Wood". In: *Philosophical Magazine Series 6* 14.79, pp. 60–65. ISSN: 1941-5982. DOI: [10.1080/14786440709463661](https://doi.org/10.1080/14786440709463661).
- Reif, F. (1998). *Fundamentals of Statistical and Thermal Physics*. McGraw-Hill series in fundamentals of physics. McGraw-Hill, p. 666. ISBN: 9780070518001. DOI: [10.1119/1.19073](https://doi.org/10.1119/1.19073). URL: <https://books.google.fr/books?id=w5dRAAAAMAAJ>.
- Ross, M. B., Mirkin, C. A., and Schatz, G. C. (2016). "Optical Properties of One-, Two-, and Three-Dimensional Arrays of Plasmonic Nanostructures". In: *The Journal of Physical Chemistry C* 120.2, pp. 816–830. ISSN: 1932-7447. DOI: [10.1021/acs.jpcc.5b10800](https://doi.org/10.1021/acs.jpcc.5b10800). URL: <http://pubs.acs.org/doi/abs/10.1021/acs.jpcc.5b10800>.
- Schäferling, M. et al. (2012). "Tailoring enhanced optical chirality: Design principles for chiral plasmonic nanostructures". In: *Physical Review X* 2.3, pp. 1–9. ISSN: 21603308. DOI: [10.1103/PhysRevX.2.031010](https://doi.org/10.1103/PhysRevX.2.031010).
- Schwab, P. M. et al. (2013). "Linear and nonlinear optical characterization of aluminum nanoantennas". In: *Nano Letters* 13.4, pp. 1535–1540. ISSN: 15306984. DOI: [10.1021/nl304692p](https://doi.org/10.1021/nl304692p).
- Semrock. *Surface Enhanced Raman Spectroscopy*. URL: <https://www.semrock.com/surface-enhanced-raman-scattering-sers.aspx>.
- Sheremet, E. et al. (2016). "Nanoscale imaging and identification of a four-component carbon sample". In: *Carbon* 96.October 2015, pp. 588–593. ISSN: 00086223. DOI: [10.1016/j.carbon.2015.09.104](https://doi.org/10.1016/j.carbon.2015.09.104).
- Shi, F. (1998). "GaN Nanowires Fabricated by Magnetron Sputtering Deposition". In: *InTechOpen.Com*. Ed. by A. B.T.N.F. R. Hashim. Rijeka: InTech, p. 225. ISBN: 978-953-307-327-9. DOI: [10.5772/681](https://doi.org/10.5772/681). URL: http://www.intechopen.com/source/pdfs/16569/InTech-Gan_nanowires_fabricated_by_magnetron_sputtering_deposition.pdf.

- Sierpinski, W. (1916). "Sur une courbe cantorienne qui contient une image biunivoque et continue de toute courbe donnée". In: *C.R. Science Academie Paris* 160.302, pp. 629–632.
- Sommerfeld, A. (1909). "Ueber die Ausbreitung der Wellen in der drahtlosen Telegraphie". In: *Annalen der Physik* 4.28, pp. 665–736. ISSN: 00033804. DOI: [10.1002/andp.19093330402](https://doi.org/10.1002/andp.19093330402). URL: <http://https://doi.org/10.1002/andp.19093330402>.
- Sonnichsen, C. et al. (2002). "Drastic reduction of plasmon damping in gold nanorods". In: *Physical Review Letters* 88.7, pp. 774021–774024. ISSN: 00319007. DOI: [10.1103/PhysRevLett.88.077402](https://doi.org/10.1103/PhysRevLett.88.077402).
- Stephens, W. (1946). "Proceedings of the American Physical Society". In: *Physical Review* 69.11-12, pp. 674–674. ISSN: 0031-899X. DOI: [10.1103/PhysRev.69.674.2](https://doi.org/10.1103/PhysRev.69.674.2).
- Taguchi, A et al. (2009). "Deep-UV tip-enhanced Raman scattering". In: *J. Raman Spectrosc.* 40, pp. 1324–1330.
- Tan, S. J. et al. (2014). "Plasmonic color palettes for photorealistic printing with aluminum nanostructures". In: *Nano Letters* 14.7, pp. 4023–4029. ISSN: 15306992. DOI: [10.1021/nl501460x](https://doi.org/10.1021/nl501460x).
- Tang, Y. and Cohen, A. E. (2010). "Optical chirality and its interaction with matter". In: *Physical Review Letters* 104.16. ISSN: 00319007. DOI: [10.1103/PhysRevLett.104.163901](https://doi.org/10.1103/PhysRevLett.104.163901).
- Tateishi, K. et al. (2015). "Highly enhanced green emission from InGaN quantum wells due to surface plasmon resonance on aluminum films". In: *Applied Physics Letters* 106.12, pp. 6–10. DOI: [10.1063/1.4916392](https://doi.org/10.1063/1.4916392).
- Vlckova, B. et al. (2007). "Single molecule SERS: Perspectives of analytical applications". In: *Journal of Molecular Structure* 834-836.SPEC. ISS. Pp. 42–47. ISSN: 00222860. DOI: [10.1016/j.molstruc.2006.11.053](https://doi.org/10.1016/j.molstruc.2006.11.053).
- Volpe, G., Volpe, G., and Quidant, R. (2011). "Fractal plasmonics: subdiffraction focusing and broadband spectral response by a Sierpinski nanocarpet". In: *Optics Express* 19.4, p. 3612. ISSN: 1094-4087. DOI: [10.1364/OE.19.003612](https://doi.org/10.1364/OE.19.003612).
- Wardley, W. P. (2016). "Development , fabrication and characterization of plasmonic structures and metamaterials for use in the ultraviolet wavelength range". PhD thesis. King's College London.
- Watanabe, K., Taniguchi, T., and Kanda, H. (2004). "Direct-bandgap properties and evidence for ultraviolet lasing of hexagonal boron nitride single crystal". In: *Nature Materials* 3.6, pp. 404–409. ISSN: 1476-1122. DOI: [10.1038/nmat1134](https://doi.org/10.1038/nmat1134).
- Watanabe, K. et al. (2009). "Far-ultraviolet plane-emission handheld device based on hexagonal boron nitride". In: *Nature Photonics* 3.10, pp. 591–594. ISSN: 1749-4885. DOI: [10.1038/nphoton.2009.167](https://doi.org/10.1038/nphoton.2009.167).
- Wen, W. et al. (2002). "Subwavelength Photonic Band Gaps from Planar Fractals". In: *Physical Review Letters* 89.22, p. 223901. ISSN: 0031-9007. DOI: [10.1103/PhysRevLett.89.223901](https://doi.org/10.1103/PhysRevLett.89.223901).
- West, P. R. et al. (2010). "Searching for better plasmonic materials". In: *Laser and Photonics Reviews* 4.6, pp. 795–808. ISSN: 18638880. DOI: [10.1002/lpor.200900055](https://doi.org/10.1002/lpor.200900055).
- White, J. (2007). *Surface Plasmon Polaritons*. Tech. rep. Stanford University. URL: <http://large.stanford.edu/courses/2007/ap272/white1/>.

- Wiecha, P. R. et al. (2017). "Local field enhancement and thermoplasmonics in multimodal aluminum structures". In: *Physical Review B* 96.3. ISSN: 24699969. DOI: [10.1103/PhysRevB.96.035440](https://doi.org/10.1103/PhysRevB.96.035440).
- Wood, R. W. (1935). "Anomalous diffraction gratings". In: *Physical Review* 48.12, pp. 928–936. ISSN: 0031899X. DOI: [10.1103/PhysRev.48.928](https://doi.org/10.1103/PhysRev.48.928).
- Yamashita, J., Wakoh, S., and Asano, S. (1975). "Electrical Resistivity of Transition Metals. II". In: *Journal of the Physical Society of Japan* 39.2, pp. 344–351. ISSN: 13474073. DOI: [10.1143/JPSJ.39.344](https://doi.org/10.1143/JPSJ.39.344).
- You, J. B. et al. (2008). "Effects of the morphology of ZnO/Ag interface on the surface-plasmon-enhanced emission of ZnO films". In: *Journal of Physics D: Applied Physics* 41.20, p. 205101. ISSN: 0022-3727. DOI: [10.1088/0022-3727/41/20/205101](https://doi.org/10.1088/0022-3727/41/20/205101).
- Yu, M. K., Park, J., and Jon, S. (2012). *Targeting strategies for multifunctional nanoparticles in cancer imaging and therapy*. DOI: [10.7150/thno.3463](https://doi.org/10.7150/thno.3463).
- Zenneck, J. (1907). "Über die Fortpflanzung ebener elektromagnetischer Wellen langs einer ebenen Leiterfl??che und ihre Beziehung zur drahtlosen Telegraphie". In: *Annalen der Physik* 328.10, pp. 846–866. ISSN: 15213889. DOI: [10.1002/andp.19073281003](https://doi.org/10.1002/andp.19073281003).
- Zhang, F. et al. (2017). "Reduction of Plasmon Damping in Aluminum Nanoparticles with Rapid Thermal Annealing". In: *Journal of Physical Chemistry C* 121.13, pp. 7429–7434. ISSN: 19327455. DOI: [10.1021/acs.jpcc.7b00909](https://doi.org/10.1021/acs.jpcc.7b00909).
- Zhang, Q. et al. (2014). "A room temperature low-threshold ultraviolet plasmonic nanolaser". In: *Nature Communications* 5, p. 4953. ISSN: 2041-1723. DOI: [10.1038/ncomms5953](https://doi.org/10.1038/ncomms5953).
- Zunger, A. and Katzir, A. (1975). "Point defects in hexagonal boron nitride. II. Theoretical studies". In: *Physical Review B* 11.6, pp. 2378–2390. ISSN: 01631829. DOI: [10.1103/PhysRevB.11.2378](https://doi.org/10.1103/PhysRevB.11.2378).
- Şendur, K. and Challener, W. (2003). "Near-field radiation of bow-tie antennas and apertures at optical frequencies". In: *Journal of Microscopy* 210.3, pp. 279–283. ISSN: 00222720. DOI: [10.1046/j.1365-2818.2003.01145.x](https://doi.org/10.1046/j.1365-2818.2003.01145.x).

Dmitry KHLOPIN

Doctorat : Matériaux, Mécanique, Optique et Nanotechnologie

Année 2017

Plasmonique d'aluminium pour des applications optiques

La plasmonique repose sur les champs électromagnétiques intenses et confinés apparaissant à résonance autour de nanostructures métalliques. Parmi ces métaux, l'aluminium soutient une gamme variée de résonances plasmoniques de l'UV jusqu'à l'IR. En raison des pertes élevées dans le visible, une amélioration est nécessaire pour concurrencer les métaux nobles. Une stratégie pour augmenter la qualité des résonances est d'utiliser un couplage diffractif au sein d'un réseau périodique. Nous montrons expérimentalement et numériquement une amélioration d'un facteur 7 du facteur de qualité par rapport à la particule isolée.

Ensuite, nous couplons des nanoparticules d'Al avec un semiconducteur à grand gap pour exalter son émission. Un réseau de particules d'Al a été déposé sur une couche épitaxiale d'oxyde de zinc. Les résultats montrent une amélioration de 1,5 fois par rapport au ZnO natif.

Pour améliorer cet effet et couvrir plus efficacement la surface, nous avons ensuite utilisé une géométrie fractale, inspirée de la technologie radio. Les structures ont été conçues via des simulations FDTD, puis elles ont été fabriquées à l'aide d'un procédé de lithographie électronique adapté.

Finalement, nous proposons le concept d'une fractale chirale. Grâce à la géométrie complexe des fractales, il est possible de pousser l'activité optique des structures plasmoniques vers la partie UV du spectre. Des échantillons ont été conçus et fabriqués, prouvant l'existence de dichroïsme circulaire dans les fractales.

Mots clés : résonance plasmonique de surface - photoluminescence - fractales - chiralité - aluminium.

Aluminum Plasmonics for Optical Applications

Plasmonics is based on the intense and confined electromagnetic fields appearing near metallic nanostructures illuminated at frequencies near their surface plasmon resonances. Among the different metals, aluminum sustains a broad range of plasmonic resonances from deep UV to near IR. Due to high losses in the visible, aluminum plasmonic structures require an improvement to compete with noble metals. First, we present a strategy to increase the resonance quality based on diffractive coupling in periodic arrays. This approach, studied with simulations and experimental methods, provides a change of quality factor of resonance up to 7 times in comparison with an isolated particle.

Then, we couple aluminum nanostructures with a wide band gap semiconductor to enhance its emission. Periodic arrays of Al nanoparticles were fabricated onto a ZnO epitaxial layer. Results show an enhancement of emission of 1.5 times in comparison with pristine ZnO.

To increase the effect and get a more efficient surface coverage, we then used a fractal geometry inspired from radiowave technology. FDTD simulations were performed to design an effective geometry and the structures were fabricated with an adapted electron beam lithography process.

Finally, we propose a concept of chiral fractals. Using the complex geometry of fractals, it is possible to push optical chirality of plasmonic structures toward the UV part of the spectrum. Samples were fabricated and the existence of circular dichroism in fractal structures was proven.

Keywords : surface plasmon resonance - photoluminescence - fractals - chirality - aluminum.

Thèse réalisée en partenariat entre :

